

THE RHOGAPS RGA-8/RICH-1/SH3BP1 AND HUM-7/MYO9 REGULATE ACTOMYOSIN
ENRICHMENT DURING *C. ELEGANS* EMBRYONIC MORPHOGENESIS

By

HAMIDAH RADUWAN

A dissertation submitted to the

School of Graduate Studies

Rutgers, The State of New Jersey

In partial fulfillment of the requirements

For the degree

Doctor of Philosophy

Graduate Program in Cell and Developmental Biology

Written under the direction of

Martha Soto

And approved by

New Brunswick, New Jersey

JANUARY 2019

ABSTRACT OF THE DISSERTATION

The RhoGAPs RGA-8/RICH-1/SH3BP1 and HUM-7/Myo9 regulate actomyosin enrichment during *C. elegans* embryonic morphogenesis

by HAMIDAH RADUWAN

Dissertation Director:

Martha Soto

Organ and tissue formation are highly regulated processes during embryonic development. Defects in this process can lead to birth defects, or premature death. The complexity of vertebrate tissues complicates the study of organ and tissue embryonic development. Epidermal morphogenesis in the nematode *Caenorhabditis elegans* is an ideal model to study tissue morphogenesis in whole organisms. *C. elegans* is amenable to genetics and microscopy observation, allowing us to capture live imaging of the migrating tissues. Previous studies from our lab identified a Rac1-dependent branched actin pathway as an important regulator of epidermal cell migration during this process. However, the role of actomyosin contractility during this process was unclear. Actin dynamics and actomyosin contractility are regulated by the Rho GTPases protein family. Rac1 and Cdc42 promote branched actin formation, while Cdc42 and RhoA promote actomyosin contractility. Rho GTPases are molecular switches that become activated by binding to GTP, and deactivated by hydrolyzing GTP to become GDP. The cycle of GTP- and GDP- binding is regulated by GTP exchange factor proteins (GEFs) and GTPase-activating proteins (GAPs), respectively. *C. elegans* only has

seven members of Rho GTPases, but 23 GAPs, suggesting layers of regulation in the process of branched actin formation and actomyosin contractility. In this study we performed the first characterization of two RhoGAPs, RGA-8/RICH-1/SH3BP1 and HUM-7/Myo9 and show that they regulate morphogenesis in *C. elegans* by modulating RHO-1/RhoA and CDC-42. We show that RGA-8/RICH-1/SH3BP1 and HUM-7/Myo9 regulate myosin enrichment during morphogenesis, including at the epidermal pocket cells during ventral enclosure. Previous studies proposed actomyosin contractility is mainly required in underlying neuroblasts to promote epidermal cell migrations. In contrast, the results here show that myosin is polarized, and tightly regulated in the migrating epidermal cells, by RGA-8/RICH-1/SH3BP1 and HUM-7/Myo9. In addition, we show these proteins contribute to normal morphogenesis by regulating the timing of morphogenetic cell movements. Overall, we place the RhoGAPs HUM-7/Myo9 and RGA-8/RICH-1/SH3BP1 in pathways that regulate both actin and actomyosin contractility through RHO-1 and CDC-42, demonstrating new roles for these GTPases in embryonic epidermal morphogenesis in *C. elegans*.

ACKNOWLEDGEMENTS

This work was conducted in the lab of Dr. Martha Soto at the Department of Pathology and Laboratory Medicine in Rutgers – Robert Wood Johnson Medical School in Piscataway, NJ, USA. I owe my deepest gratitude to Dr. Soto, who gave me the opportunity to work in her group and provided her best possible support throughout my years of study.

The following organizations are sincerely thanked for providing financial support to this work. NIH for grant support to conduct the research in the Soto lab. The Graduate School of Biomedical Sciences under RWJMS Biomedical and Health Sciences for dissertation fellowship during my thesis phase. Numerous other travel awards that will not be mentioned in detail here but are instrumental for the opportunity to present my research to the scientific community at large.

I wish to thank the previous and current head of the Cell and Developmental Biology program, Dr. Richard Padgett and Dr. Kenneth Irvine respectively, on their help navigating the PhD requirement related to the program. I am grateful to the members of my thesis committee, Dr. William Wadsworth, Dr. Kenneth Irvine and Dr. Joan Bennett for their great moral and intellectual support. Their excellent comments and suggestions had improved my thesis project tremendously throughout the years I spent on the project.

I am especially grateful to Dr. Andre G. Wallace, Eric Larsen, Dr. Loren Runnels, Dr. Donald Winkelman, and Dr. Marc Tuazon for their invaluable help in technical assistance as well as intellectual input in the matter of my study, and for kindly providing help and advice whenever needed. I would also like to thank

Rachel M. Rebello and Sushma M. Mannimala for being a great mentee and had been a tremendous help with my side project, which will not be discussed in the thesis. My sincere thanks to Theresa Mustacchio for technical assistance and for her help in the same project.

The Soto lab provided a great atmosphere and useful challenge in the working environment. For that, I would like to thank all my past and present colleagues: Maria, Jenn, Andre, Vipin, Marc, Eric, Rachel, Sushma, Theresa, Sofya, and SK. Special thanks to Andre who provided my initial training when I first joined the lab.

In addition to our lab, the whole second floor of the research tower has provided a conducive environment for research. I especially thank Maya, Karen, Ping, Nancy, Daniel and Erik for being great “work” neighbors. I would like to extend my gratitude to all personnel working at the administrative unit, IT support, kitchen and the equipment care unit (especially Walter) for saving a lot of my time by making everyday life so much easier.

Many thanks to all my friends for dragging me out of the lab once in a while and exposing me to the better things in life. Finally, I would like to express my deepest gratitude to my family and BFFs for their continued support along these years. I will not have made it this far without any of them by my side.

Hamidah Raduwan

December 17, 2018

TABLE OF CONTENTS

ABSTRACT OF THE DISSERTATION.....	ii
ACKNOWLEDGEMENTS	iv
CHAPTER 1: Introduction	1
<i>C. elegans</i> epidermal morphogenesis	2
Dorsal intercalation	3
Ventral enclosure	4
Elongation	5
Morphogenetic events are regulated by actin-based forces	8
Types of actin-regulated structures.	9
The ARP2/3 complex as branched-actin nucleator	10
Nucleation-Promoting Factors (NPFs)	11
Parallel to <i>C. elegans</i> epidermal morphogenesis	13
Rho-family GTPases are upstream regulators for actin and actomyosin dynamics	16
The GTPase activating protein (GAPs)	17
HUM-7/Myo9A/Myo9B	18
RGA-8/SH3BP1/Rich1/Nadrin	18
BAR domain proteins – linking the cytoskeleton with the membrane.....	20
BAR protein and the regulation of cytoskeleton dynamics	21

Rationale	23
CHAPTER 2: CDC-42 and the RhoGAP RGA-8 polarize myosin in the epidermis during ventral enclosure	26
Abstract	27
Introduction	28
Results	34
Discussions	48
Materials and Methods	56
Figure Legends	62
CHAPTER 3: The RhoGAP myosin 9/HUM-7 integrates signals to modulate RhoA/RHO-1 during embryonic morphogenesis in <i>Caenorhabditis elegans</i>	74
Abstract	75
Introduction	76
Results	81
Discussion	94
Materials and Methods	100
Figure Legends	107

CONCLUSION.....	123
APPENDIX I: Cloning	130
CRISPR strategy to generate mutants and fluorescent-tagged genes.....	131
Generation of RNAi Clone	141
REFERENCE.....	143

LIST OF TABLES

TABLE 1 List of <i>C. elegans</i> genes used in this study and their homologs	25
TABLE 2 Embryonic lethality count for the respective mutants, represented in Figure 6.	45
TABLE 3 Embryonic lethality count for the respective mutants, represented in Figure 7.	46
TABLE 4 All strains used in this study	56
TABLE 5 List of dna primers used in this study to generate knockout and tagged RGA-8 using the CRISPR method	59
TABLE 6 Embryonic lethality due to the loss of <i>hum-7</i>	120
TABLE 7 Terminal embryonic phenotypes caused by loss of <i>hum-7</i>	122
TABLE 8 List of primers used to generate CRISPR line.....	138
TABLE 9 Primers used to generate <i>let-502 mai</i> clone.....	141
TABLE 10 The embryonic lethality count of the constructed plasmid for <i>let-502</i> gene.....	142

LIST OF FIGURES

FIGURE 1 Stages of embryonic development in <i>C. elegans</i>	2
FIGURE 2 Ventral enclosure.....	4
FIGURE 3 Elongation stage of epidermal morphogenesis in <i>C. elegans</i>	6
FIGURE 4 Illustrative representation on the structural functional unit of actin (red) in the migrating cells.	9
FIGURE 5 Structure and cyclic regulation of myosin ii	13
FIGURE 6 CDC-42 controls morphogenesis in <i>C. elegans</i>	67
FIGURE 7 RGA-8, a GTPASE activating protein (GAP), regulates CDC-42 and RHO-1, but not CED-10/RAC1	68
FIGURE 8 RGA-8 is enriched on the membrane in the epidermis and apically- enriched in the intestine.....	69
FIGURE 9 Transient co-localization of mKATE2::RGA-8 on the epidermal membrane together with active CDC-42	70
FIGURE 10 Defective CDC-42 pathway cause increased level of epidermal F- actin in <i>rga-8(pj60)</i>	71
FIGURE 11 Mutant <i>rga-8(pj60)</i> caused decreased myosin level in the epidermal pocket cells.....	72
FIGURE 12 Mutant <i>rga-8(pj60)</i> affects timing of leading-edge cell migration and elongation.....	73
FIGURE 13 HUM-7/MYOSIN 9 interacts genetically with axonal guidance receptors and is required during embryonic morphogenesis.	114

FIGURE 14 HUM-7/MYOSIN 9 interacts genetically and molecularly with RHO GTPases.....	115
FIGURE 15 HUM-7 is expressed in muscles, and regulated by SAX-3/ROBO.	116
FIGURE 16 HUM-7 affects F-actin levels and dynamics in migrating epidermis during embryonic morphogenesis.	117
FIGURE 17 NMY-2::GFP colocalizes with F-actin in epidermal cells during enclosure.....	118
FIGURE 18 SAX-3/HUM-7/RHO-1 regulate non-muscle myosin, NMY-2, in epidermal cells	119
FIGURE 19 Sewing PCR strategy to generate the sgRNA.....	133
FIGURE 20 Generation of sgRNA in a plasmid vector	134
FIGURE 21 co-CRISPR injection strategy	135

CHAPTER 1: Introduction

C. elegans epidermal morphogenesis

Our lab is interested in the regulation of actin cytoskeleton during *Caenorhabditis elegans*' embryonic epidermal morphogenesis. Epidermal cells

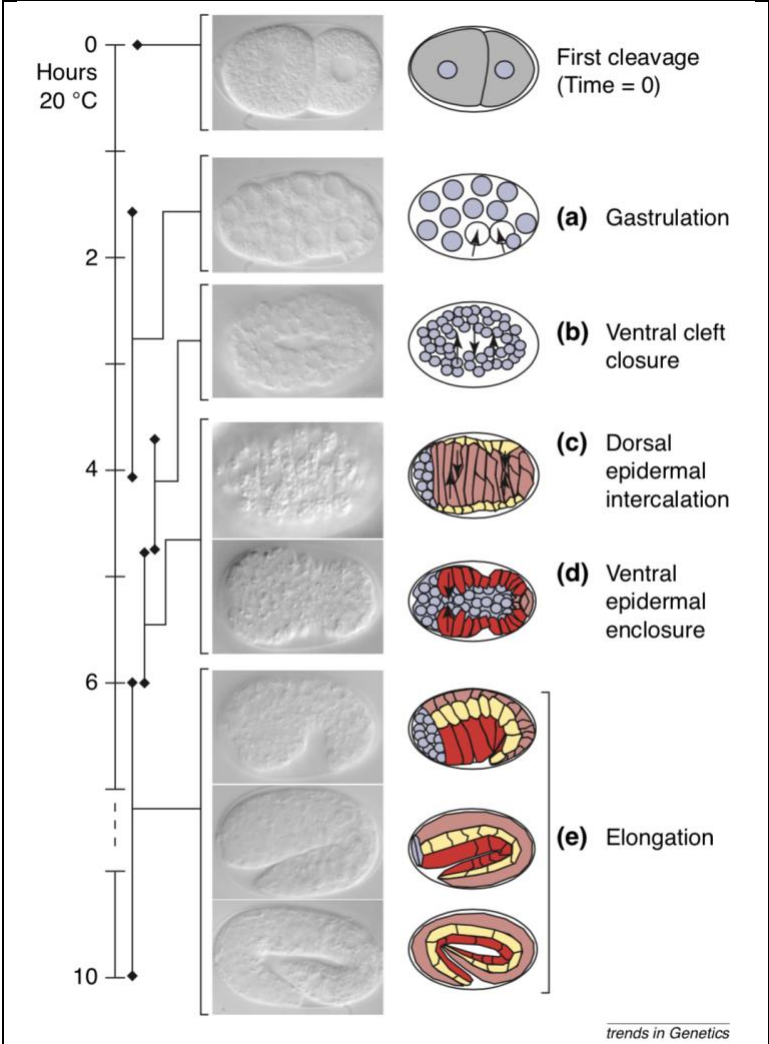


Figure 1 Stages of embryonic development in *C. elegans*.

(c) to (e) are different stages of epidermal morphogenesis. Source: (1)

descended from the AB cell lineage and became fully differentiated at ~4 hours post-fertilization. Fully differentiated epidermal cells arise at around 220-240 minutes after the first cleavage, as measured by the expression of LIN-26 (2). The differentiated cells localize at the dorso-posterior surface of the embryo. The cells form six rows that first migrate ventrally to enclose the embryo along the ventral midline and then extend to surround the anterior

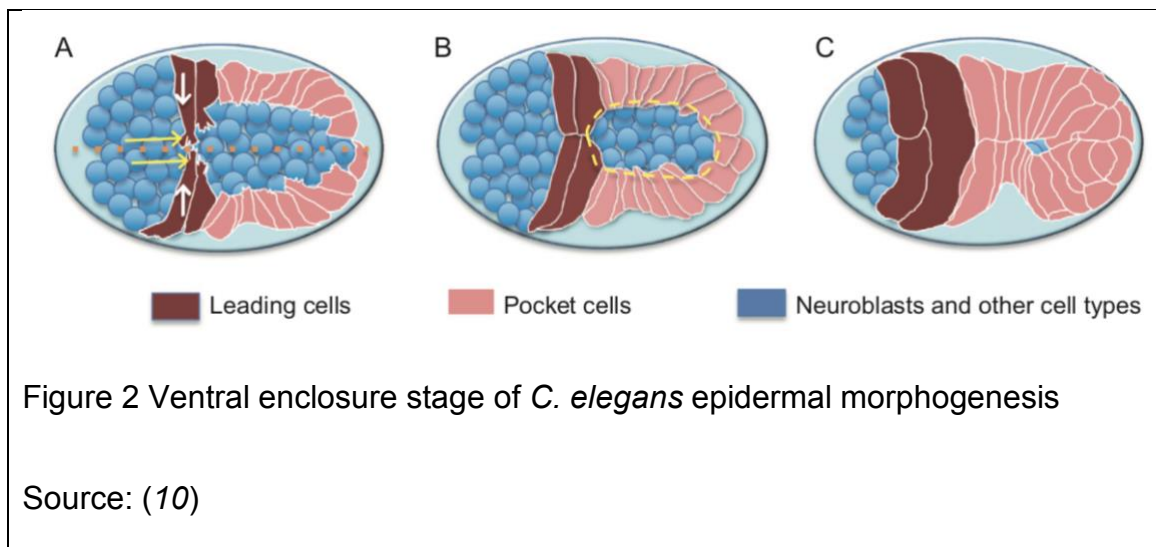
end. Following epidermal enclosure, the embryo undergoes constriction circumferentially and elongates along anterior to posterior axis. Morphogenesis of the epidermal cells of *C. elegans* embryo requires both cell-autonomous signals as well as their interaction with underlying tissues (1, 3-7). This process can be divided into several steps, as discussed further below (Figure 1).

Dorsal intercalation

One of the first movement of the embryonic epidermis is dorsal intercalation, a process that elongates the cells along the anterior/posterior axis, similar to the convergent extension in vertebrates (8). Dorsal intercalation is defined as the process when the two rows of dorsal cells rearrange and migrate towards each other to form a single row of dorsal cells. At first, rectangular dorsal cells change shape and extend basolateral protrusion to form wedge shape-cells that interdigitate in between each of the opposite dorsal cells. They then further migrate towards the opposite dorsal cells to finally establish a single row of cells. Studies showed that this process requires actin and microtubule (Figure 1, (6)). Interestingly, while the nuclei of the cells also migrate towards the direction of cell intercalation, nuclear migration is not required for successful intercalation (9). Shortly after, the cells fuse to form a syncytium (hyp7). In my thesis, I chose not to explore the topic of dorsal intercalation.

Ventral enclosure

Ventral enclosure begins shortly after the start of dorsal intercalation and occurs almost simultaneously. The ventral epidermal cells at each side must migrate towards the ventral side as a thin sheet on top of the neuroblasts to enclose the internal organs. This process was shown to be mediated by the actin and microtubule cytoskeleton in 1997 (5). This is a two-step process, first initiated by the two anterior-most ventral cells on each side that migrate and meet at the ventral midline, followed by constriction of the remainder of the posterior ventral epidermal cells, called pocket cells, to medially enclose the embryo (Figure 2, (5)). The ventral epidermal cells from the two sides make contact at the ventral midline and form junctions to seal the two rows of cells through the process termed filopodial priming (7). Further mechanistic regulation of these two-step process is further discussed below.



Step 1: Leading cell migration: In the first step, the two most anterior cells from each side initiate the process of the ventral enclosure by extending their leading

membrane toward the ventral midline. These cells are called the leading-edge cells (LC), and the membrane extensions were first shown to be dependent on actin activity. Laser ablation study of the leading cells resulted in most embryos failing to undergo ventral enclosure, demonstrating that the LC drive the progression of the ventral enclosure by pulling their neighbors along with them (5).

Step 2: Pocket cell migration: After meeting of the two pairs of leading cells at the ventral midline, the pocket cells enclose via the purse-string mechanism similar to *Drosophila* dorsal closure. This is based on the observation that the actin cable is enriched at the front of the pocket cells. Indeed, several publications showed enrichment of NMY-2/myosin II puncta at the front of migrating epidermal cells (11, 12), suggesting a role of actomyosin contractility in this process.

Elongation

As the epidermal cells complete the enclosure of the embryos, it undergoes an elongation process, resulting in a 4-fold increase in length and a 2-fold decrease in diameter forming an elongated vermiform larva. This happens while neither cell division nor cell differentiation occurring, and the volume of the entire embryo remains constant. Epidermal cells are essential for this process, as laser abrogation of epidermal cells at this stage caused the embryos to contract and fail to elongate (3, 4). This process requires actomyosin contractility on the epidermal seam cells as well as muscle contractility (4, 13). The elongation process is divided into two phases – early elongation and late elongation (10). Each stage is regulated by distinct molecular pathways (Figure 3).

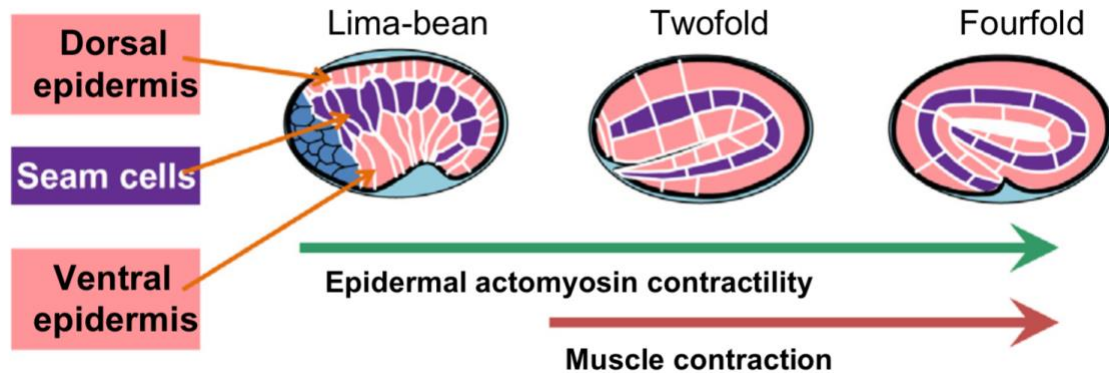


Figure 3 Elongation stage of epidermal morphogenesis in *C. elegans*.

Source: (10)

Step 1: Early elongation up to the two-fold stage: Elongation was first shown to require actin from an early pharmacological study of *C. elegans* embryonic elongation after treatment with cytochalasin-D that disrupts the elongation process. At the onset of elongation, actin is organized as filaments that connect the two circumferential ends of epidermal cells, called the circumferential actin bundles (CFB). Circumferential actin bundles first formed in the dorsal and ventral epidermis, followed by the seam cells (4). This initial observation suggests that actomyosin force are responsible for squeezing the embryo radially to decrease its diameter while simultaneously increase its anterior to posterior length.

Step 2: Late elongation post 1.7 fold: When the *C. elegans* embryo reaches close to the 1.7-fold stage, muscle cells start to contract. Elongation from this time onwards is thought to be primarily under the regulation of the muscle cells, while actomyosin contractility in the epidermis is believed to be less critical. Muscles are tightly connected to the dorsal and ventral epidermal cells through trans-epithelial

attachment structures, known as fibrous organelles (FOs). FOs act as tendons that transmit the forces exerted by muscle contraction to the cuticle exoskeleton (14, 15). Two hemidesmosome-like junctions, (known as CeHD in *C. elegans*), each on apical and basal side, are connected via intermediate filaments within the FOs (16). Tension from the muscle cells is transmitted to the epidermis via the CeHDs. Muscles contract every 1-5s, inducing oscillatory mechanical stimuli to the epidermal cells, promoting further elongation of *C. elegans* embryo (17).

Morphogenetic events are regulated by actin-based forces

Morphogenesis is a highly coordinated process to allow movement of cells in a precise manner. Collective cell migration is a hallmark of the morphogenesis process when a group of cells has to move to the targeted location while remaining attached to each other. This process involves dynamic changes in the cell shape, cell polarity, and cell attachment. All of these changes require the coordinated regulation of the cytoskeletal network inside the cells. The cytoskeleton inside the cells helps maintain their shape and internal organization while supporting the mechanical tension inside the cells to carry out the movement.

The cytoskeleton contains actin, which is a highly conserved protein across evolution and is the most abundant protein in the eukaryotic cells. It exists as both a soluble globular monomer (G-actin), as well as in filamentous form (F-actin). G-actin polymerizes to form F-actin that organizes into dynamic networks that regulate many structural and functional roles in the cells. It is involved in a variety of cellular processes, such as cell movement, vesicle trafficking, endocytosis, as well as cell shape and polarity maintenance.

Types of actin-regulated structures.

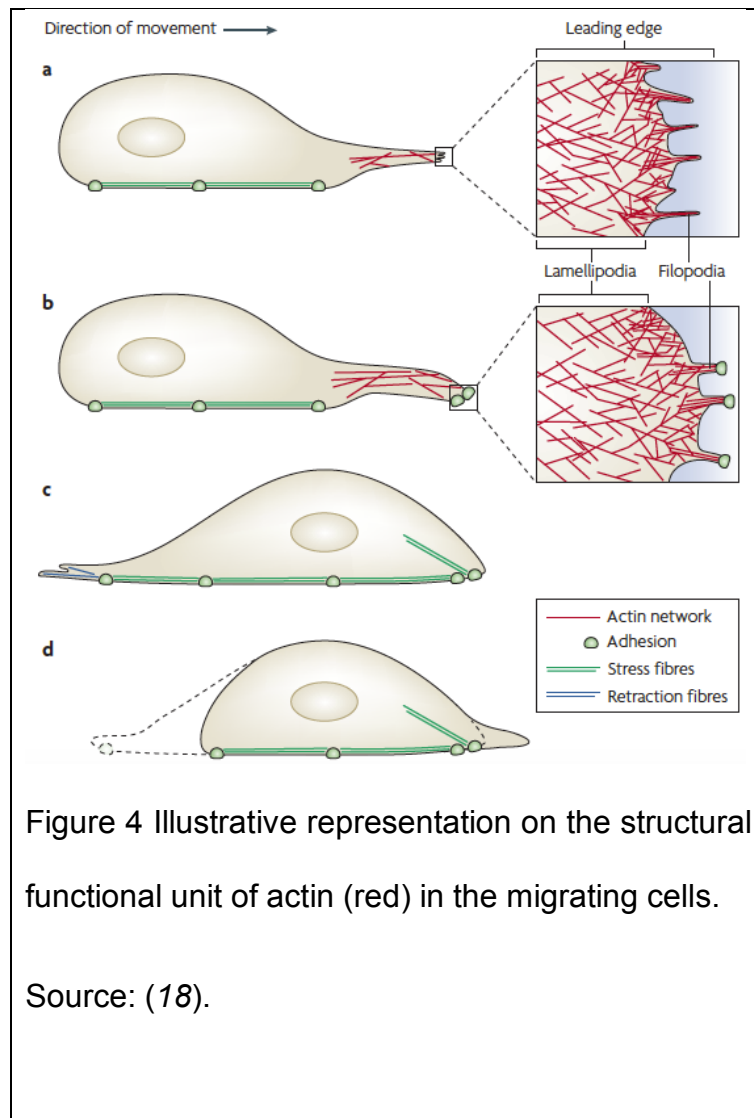


Figure 4 Illustrative representation on the structural functional unit of actin (red) in the migrating cells.

Source: (18).

Lamellipodium is a broad, sheet-like membrane that protrudes in the direction of migration. This structure is the main driving force in cell motility and is primarily regulated by branched actin network. Lamellipodia are transient structures, that rapidly protrude and retract, and require the action of a multitude of branched actin regulators, F-actin elongation and

depolymerizer to balance the F-actin assembly and disassembly within the dynamic structures of lamellipodia (19).

Filopodium is a thin, finger-like actin-rich protrusion that is embedded in the lamellipodial structure. Filopodial actin is usually in the form of long parallel tight bundles. This protrusive structure plays diverse morphogenetic roles (18).

Filopodia had been shown to regulate epithelial sheet sealing by facilitating proper alignment of cells for junction formation (7, 20, 21). Filopodia can also sense the environment to guide cell migration while remaining adhesive with the ECM. Traditionally, the CDC-42 GTPase was shown to regulate filopodia formation in a WASP-dependent manner. However, several reports suggest that filopodia can still form when WASP is removed, suggesting that there might be other signaling pathways regulating filopodial formation (22, 23). Within the finger-like protrusion, F-actin mostly exists in a linear structure that is arranged in a tight bundle (24, 25). Linear F-actin is regulated by a formin family of F-actin nucleator (26).

Actomyosin network consists of bipolar myosin II motor sliding along anti-parallel actin filaments (F-actin) through conversion of chemical (ATP hydrolysis) and mechanical energy (displacement of the myosin II head) (27, 28). Regulation of myosin II movement along F-actin is primarily under RHO-1 GTPase. Actomyosin network serves as the mechanosensor that mediates tension distribution while the cells exert pushing and pulling forces as the cells migrate. During cell migration, actomyosin is involved in many cellular processes, such as maintaining junctional integrity during collective cell migration and mediating front-back polarity.

The ARP2/3 complex as branched-actin nucleator

The actin monomer (G-actin) is polymerized into filamentous actin (F-actin) by processes involving multiple proteins. F-actin can exist in two forms, the linear or branched actin. Actin-related protein 2/3 complex (ARP2/3 complex) plays a

pivotal role in initiating branched actin polymerization in eukaryotic cells. This complex consists of seven subunits. Two of the subunits are actin-related protein (ARP) 2 and 3, hence the name ARP2/3 complex. Others are actin-related protein complex 1 to 5 (ARPC1, ARPC2, ARPC3, ARPC4, and ARPC5). This complex is highly conserved from yeasts to vertebrates, underscoring the importance of branched actin formation in a multitude of biological processes. The ARP2/3 complex has no activity on G-actin by itself. Once it is engaged with a nucleation-promoting factor (NPF), polymerization of actin monomer is initiated on the existing actin filament at 70° angle (29). ARP2 and ARP3 remain associated at the base of new branched actin filaments.

Nucleation-Promoting Factors (NPFs)

The ARP2/3 complex cannot initiate branched actin polymerization on its own and requires the action of nucleation-promoting factor (NPF) proteins. The major class of NPFs is the Wiskott-Aldrich Syndrome Protein (WASP) family of proteins, which consist of five subfamilies - WASP, WASP-family verprolin homologous protein (WAVE), WASP homolog associated with actin, membranes and microtubules (WHAMM), WASP and SCAR homolog (WASH), and junction-mediating regulatory protein (JMY) (25, 30, 31). Two of the well-characterized WASP-family NPFs, which are the WAVE/SCAR and WASP/WSP-1 will be discussed here.

WASP, the first NPF discovered of its class, was named after the Wiskott-Aldrich syndrome (WAS), a rare X-linked recessive disorder, characterized by a

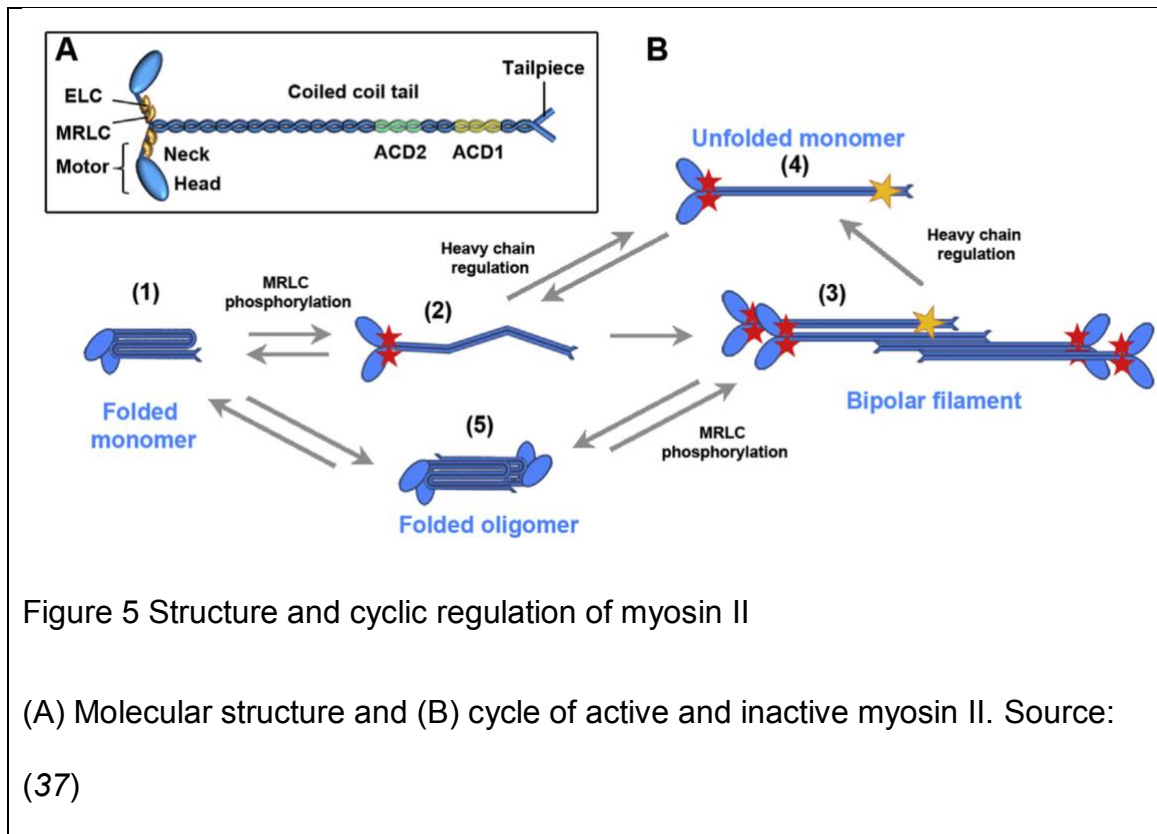
combination of immunodeficiency, thrombocytopenia, and eczema in patients (19, 20). WASP usually exists in an autoinhibited, folded conformation. Intramolecular interaction between the GBD and the C-terminus VCA region inhibits access of the ARP2/3 complex to the CA region. Competitive binding of Cdc42 or PIP2 with N-terminus region of WASP can disrupt the folded conformation and reveals the VCA region to ARP2/3 complex. ARP2/3 becomes activated when bound to the CA region on the C-terminal of WASP/WAVE proteins and initiates actin polymerization when bound in conjunction with an actin monomer binding to the V region.

The WAVE/SCAR complex was first discovered in humans and *Dictyostelium* as a protein that has sequence similarity to the verprolin homology domain of WASP, thus named WASP-family verprolin homologous protein (WAVE) (26). It was shown to act downstream of Rac1 to regulate branched F-actin (32, 33). The WAVE/Scar complex consists of five subunits - WAVE1/Scar, Abi (Abl-interactor), HSPC300, Nap (Nck-associated protein), and PIR21 (p53-inducible mRNA). In contrast to WASP, WAVE/Scar complex is trans-inhibited. Binding of Rac1 to Nck cause disassembly of WAVE1 in association with HSPC300, causing activation of branched F-actin formation (34).

Regulation of myosin II activity

Myosin II undergoes constant polymerization-depolymerization cycle, one in the folded, autoinhibitory conformation, and another in the assembled bipolar filament.

This cycle is what allows myosin II to regulate contractility in the cells. The cycle of active and inactive conformation of myosin II is controlled by many phosphorylation sites, one of which is on the myosin regulatory light chain (MRLC). MRLC is phosphorylated by Rho kinase (ROCK), and dephosphorylated by myosin phosphatase (MYPT) at Ser19 residue (27, 35-37), (Figure 5). This cycle of phosphorylation is highly conserved across species.



Parallel to *C. elegans* epidermal morphogenesis

The *C. elegans* WAVE complex, just like its homologs, consists of five subunits, and removing parts of the complex, alone or in combination caused the embryos to die during epidermal morphogenesis, with a terminal phenotype that

we named Gex (gut on the exterior) (38, 39). Indeed, the *C. elegans* CED-10/Rac1 was shown to have a role during epidermal morphogenesis (38-40). CED-10/Rac1 is the only one of three Rac proteins identified in *C. elegans* to have a role during epidermal migration (41). Homozygous knockout of this gene is 100% lethal with a highly penetrant Gex phenotype, and embryos with hypomorphic alleles of *ced-10* were shown to have a milder, partially penetrant Gex phenotype (38). The *ced-10* null allele, *n3417*, had been shown to be defective in this process that resulted to a Gex phenotype at 71% penetrance (38).

In addition, the entire pathway, CED-10/Rac1-WAVE/SCAR-Arp2/3, is required for epithelial morphogenesis of the intestine in *C. elegans*. This pathway is involved with establishment and maintenance of apical polarity since the removal of the WAVE/SCAR and Arp2/3 complex results in decreased apical F-actin enrichment in embryos and adults (39). However, some apical F-actin is assembled (42). Further, it was shown that Rac1/CED-10 is involved in regulating the direction of the protrusion (40), while Cdc-42 is involved in orienting the direction of the cell tips (43) during dorsal intercalation of the epidermal cells.

It has been reported that embryonic elongation is dependent on RHO-1-regulated actomyosin contractility. Actomyosin, referring to the actin-myosin complex, exerts its contractile force by the action of myosin pulling on the actin filaments. This creates a mechanical force across the cells in the direction of the actin filaments.

During *C. elegans* embryonic elongation, the CFB are directed radially along the embryo, thereby creating the force that squeezes the worm to reduce its

diameter while simultaneously increase in length. Two myosins found to be involved in this process are non-muscle myosin 1 (NMY-1) and non-muscle myosin 2 (NMY-2), which belong to class II (44). NMY-2 appears to be more important during early embryonic stages for cytokinesis and differentiation, while NMY-1 seems to be dispensable for these processes (44) The mechanisms by which myosin moves along actin filaments are highly conserved across species.

Nonmuscle myosin II motors are regulated through phosphorylation and dephosphorylation of the regulatory light chain MLC-4 by the LET-502/Rho-binding kinase and MEL-11/Myosin binding subunit of myosin phosphatase, respectively. LET-502/Rho-binding kinase (ROCK) and MEL-11/Myosin phosphatase (MYPT) are required for the elongation process (45). The LET-502/ROCK is expressed in the epidermal seam cells (45), while MEL-11/MYPT is expressed in the dorsal and ventral epidermis (46). Both of these proteins act antagonistically to regulate *C. elegans* embryonic elongation (45, 46). Removing MEL-11 causes hypercontractility and embryos burst due to increased tension on adherens junctions. Removing LET-502/ROCK causes embryonic elongation defects. Activation of myosin II is achieved mainly through the LET-502/Rho kinase, but two additional kinases can contribute to maintaining myosin II activity. P21-activated kinase PAK-1 and CDC-42-activated kinase MRCK-1 act in parallel to LET-502, since their loss enhances let-502 mutant severity. It was further shown that MRCK-1 acts upstream of MEL-11, and that MRCK-1 is under the regulation of CDC-42 (47).

Rho-family GTPases are upstream regulators for actin and actomyosin dynamics

RhoA was the first identified member of GTPases by Axel's group in 1985 (48). Following this discovery, many of similar proteins were later found to be closely related to Rho, and were grouped into the Rho GTPase family. The Rho GTPases consists of three main subgroups – Cdc42, Rac1, and Rho. Each subgroup was thought to regulate specific actin-related cytoskeletal structures: Rho induces the assembly of stress fibers, Rac1 induces the assembly of actin-rich, broad lamellipodial membrane protrusions and Cdc42 regulates actin-rich, finger-like protrusions called filopodia (Figure 4, (49, 50)). In addition to the intracellular signals, these GTPases are thought to be activated by signals from the extracellular space, transmitted by transmembrane receptors that relay the signals to the GTPases. As such, the Rho GTPase family of protein regulates many biological processes such as protein trafficking, cell migration, cell polarity, and tissue morphogenesis.

RHO-GTPases acts as molecular switches that are turned on and off in response to cellular cues. They are active while bound to GTP, and inactive while bound to GDP. The cycle of GTP- and GDP-bound states is regulated by two classes of protein, the GTPase activating protein (GAP), and guanine-nucleotide exchange factor (GEF). The GAPs are involved in activating the intrinsic GTPase activity, thereby hydrolyzing the GTP to the GDP state, consequently inactivating

the RHO GTPases activity. The GEFs are involved in exchanging the GDP with a new GTP, thus turning on the GTPase activity (51, 52).

The GTPase activating protein (GAPs)

In *C. elegans*, there are 23 members of the GAP family (53). In comparison, there are only seven Rho GTPase members (54), suggesting multilayers of regulation to ensure efficient signaling pathways. I investigated the morphogenesis function of two GAPs, RGA-8/SH3BP1/Rich1 and HUM-7/Myo9.

GTPases reaction mechanisms

The intrinsic GTP hydrolysis capability of Rho GTPases occurs at a very slow rate. The presence of GAP interactors accelerates the hydrolysis of GTP to GDP. Insights into the mechanism of how GAPs regulate the Rho GTPases are derived largely from structural studies (52, 55). The GAP domain consists of about 200 amino acid residues corresponding to nine alpha-helices. Its core contains four helices bundle, one of which contains a highly conserved arginine residue (52). This arginine residue, famously known as the arginine finger, interacts with glutamine 61 of the GTPase, thereby positioning a hydrolytic water molecule for nucleophilic attack of the γ -phosphate of GTP (52, 55). Indeed, mutation on glutamine 61 on the GTPase generally abolishes GAP-induced GTP hydrolysis, causing a constitutively active mutation of the GTPase.

HUM-7/Myo9A/Myo9B

HUM-7/Myo9 is a member of non-conventional myosin of class IX. The HUM-7/Myo9 protein contains an N-terminal single-headed myosin motor that moves towards the plus, or barbed, ends of F-actin (56-61). It also has conserved RA (Ras associated) and C1 domains that are less well understood. Loss of function mutations or overexpression of these proteins has been linked to various cancers and immune defects. The mouse knock out of Myo9a results in CNS and kidney defects (62, 63) that may involve changes in protein trafficking, while the mouse Myo9b knockout results in altered morphology and motility of immune cells (57) and impaired intestinal barrier function (58). Some studies support a role for Myo9b in human intestinal diseases like inflammatory bowel disease and Crohn's disease (64-66).

RGA-8/SH3BP1/Rich1/Nadrin

RhoGTPase activating protein-8 (RGA-8) has four close human homologs, which are SH3-binding protein 1 (SH3BP1), RhoGAP-interacting with CIP4 homologs (Rich1/Rich2), ARHGAP17 and Nadrin. SH3BP1 and RICH-1 were first discovered as proteins that interact specifically with the SH3 domain of TOCA-2/1 and CIP4, respectively, via their C-terminus proline-rich domain. Both SH3BP1 and Rich1/Rich2 have been shown to interact with Rac1 and Cdc42, but not RhoA. SH3BP1 was proposed to associate with exocyst complex to regulate Rac1 turnover at the membrane front to regulate cell migration (67), and to regulate Cdc42 and Rac1 in a sequential process of cell junction formation by controlling

the actin dynamics through association with CapZ, and guide Cdc42 signaling to promote junction assembly (68). SH3BP1 also regulates fast-endophilin-mediated endocytosis (FEME) in a clathrin-independent manner (69).

RICH-1 was first found to bind to the SH3 domains of CIP4, FBP17, and syndapin, and stimulates GTPase activity of Rac1 and Cdc42, but not RhoA (70). Rich1 contain multiple proline-rich motifs, suggesting that it can bind to multiple SH3-domain-containing proteins. Rich1 and CIP4 were shown to co-localize, and this colocalization was dependent on active Cdc42. Rich1 was first discovered in 2001 as a strong interacting partner with the SH3 domain of CIP4, formin-binding protein 17 (FBP17), and syndapin (70). In MDCK cells, Rich1 was shown to maintain tight junction integrity by the coordinated regulation of Cdc42 to specific pathways of intracellular trafficking (71). The BAR domain of RICH-1 binds to various membrane lipids, but shows the strongest affinity towards PI, PI(4)P, and PI(5)P. In addition, it can bend membranes into tubular form with a diameter between 50nm to 250nm. Interestingly, RICH-1 can bind to endophilin and amphiphysin (72), suggesting the ability to heterodimerize between different members of BAR-related protein.

BAR domain proteins – linking the cytoskeleton with the membrane.

The Bin-Amphiphysin-Rvs (BAR) domain is a motif that allows a protein to target lipid bilayers and provide the scaffolding that helps mold the membrane into a curvature. This amino acid domain is present in many proteins and is characterized by the presence of a surprisingly poorly conserved 200 amino acids sequence. There is no real consensus on the classification for protein members of the BAR domain superfamily, and new proteins that can sculpt membrane curvature are continually being found. Although there is poor similarity of the domain found at the amino acid sequence level, most members of this superfamily share high similarity at the 3D-structural feature. The most recent review classified members of this BAR protein superfamily into six classes – N-BAR, F-BAR, I-BAR, BAR-PH, PX-, and BAR-PDZ (73).

The BAR domain is characterized by the presence of three alpha helices that fold into crescent-shaped antiparallel dimers (74). The degree of curvature varies between the different classes. The N-BAR and BAR-PH have a higher degree of curvature compared to F-BAR and PX-BAR. In contrast, I-BAR dimerization produced a zeppelin-like shape and is thought to induce negative membrane curvature.

One model to explain how the BAR domains bend the membrane proposes a higher order assembly, with BAR protein decorating the membrane surfaces to induce bending. One study shows the higher order assembly of F-BAR on the

membrane – F-BAR of FBP17 and CIP4 initially binds to flat membranes, and subsequent oligomerization results in membrane deformation *de novo* (75). Similarly, N-BAR of endophilin induces membrane bending, and the N-terminal helices stabilize the scaffolding (76).

BAR protein and the regulation of cytoskeleton dynamics

All members of BAR superfamily had been shown to be involved in Rho GTPase-dependent signaling pathways. Most BAR superfamily proteins are multidomain, allowing them to bind to other proteins and the plasma membrane either simultaneously or sequentially, BAR domain may serve as a converging point between many signaling pathways within the cells. In addition, some of the BAR protein contains GAP or GEF domains, which suggest direct interaction with GTPase to directly affect the cytoskeleton. Finally, other BAR superfamilies may indirectly interact with GTPase, as part of a complex.

Some BAR domain-containing proteins serve as a linker between the membrane to the actin cytoskeleton, by having an interacting domain that binds to actin NPF. The SH3 domain of TOCA1/CIP4/FBP17 binds to a proline-rich sequence of WASP NPF, thereby recruiting WASP to the curved membrane to promote actin polymerization (77). In addition, an I-BAR protein IRSp53 was shown to interact with WAVE2 to induce ARP2/3-dependent branched F-actin (78, 79). Therefore, the BAR superfamily can serve as a mediator between the membrane and the NPFs.

Interestingly, several proteins in the BAR superfamily have been shown to have the capacity to bind directly to F-actin. The N-BAR domain of PICK1 was the first to be shown to have direct interaction with F-actin. Interestingly, PICK1 can also bind directly to ARP2/3 and attenuate ARP2/3-dependent F-actin polymerization (80). In another report, the F-BAR domain of pacsin2 was shown to bind to F-actin using the same concave surface used to bind to plasma membranes (81). The BAR domain of human Bin1 (hBin1) can bind to both F-actin and G-actin, but preferentially to F-actin. Interestingly, hBin1 could stabilize F-actin by promoting cofilin severing activity to induce more F-actin polymerization and could promote F-actin bundling (82). Overall, members of BAR superfamily had been shown to have the ability to bind and regulate F-actin polymerization or depolymerization.

Rationale

Cell migration plays an integral role in many biological processes throughout the life of the organisms. It is a highly orchestrated process that is regulated by many proteins in multitude interconnected signaling pathways. These signaling pathways coordinate the organization of the cytoskeleton, e.g. actin and tubulin, that drives the protrusion and retraction of the plasma membrane as the cells migrate. Smooth muscle cell migration is vital during tube formation of organs such as the blood vessel (83). Migration of neuroblast (precursor of neurons) is essential during development to form a fully functional brain (84). In addition, cell migration remains prominent in adult organisms, in both normal physiology and pathology. Cell migration is needed during an effective immune response (85) or repair of injured tissues (86). Molecular mechanisms involved during wound healing had been shown to have a lot of similarity to morphogenetic movement occurring during development (87).

Failure for cells to migrate can cause abnormalities to the development of the organisms and sometimes be life-threatening. Development of tube formation and hollow organs such as the airways and blood vessel involve coordinated migration of the smooth muscle cells. Defective migration of smooth muscle cells has been implicated in the pathogenesis of airway development, one of the key feature in people suffering from asthma (83). Defective cell migration during nervous system development can cause congenital defects in the brain that leads to many mental disorder and epilepsy (84). Finally, metastatic cancer acquires

defective cell migration that allows them to migrate and colonize different parts of the body (88-90).

As such, it is imperative to study the process of cell migration. Identification of the molecular mechanisms involved during cell migration will allow us to move a step closer in understanding the mechanism of action on how many diseases involving defective cell migration occurring, such as during cancer metastasis, and defective neuronal development. Hence, there is considerable interest in understanding the molecular mechanisms of cell migration. This could lead to the development of a therapeutic approach in treating migration-related diseases. My research topic uses *C. elegans* epidermal morphogenesis as a model to understand the molecular mechanisms and signaling pathway involved during cell migration. From this thesis, two more proteins were added in the pathways that regulate cell migration in *C. elegans* epidermal morphogenesis, which are RGA-8 and HUM-7/Myosin IX (12).

Table 1 List of *C. elegans* genes used in this study and their homologs

Complex	<i>C. elegans</i>	<i>Homo sapiens</i> homolog
ARP2/3	ARP-2	ARP-2
	ARP-3	ARP-3
WAVE/SCAR	ABI-1	Abl-interactor (Abi)
	GEX-2	Sra1
	GEX-3	HEM2 NAP1 (Nck-associated protein) KETTE
	GEX-1 WVE-1	WAVE-1
WASP	WSP-1	WASP N-WASP
N/A	TOCA-1 TOCA-2	TOCA-1 FBP17 CIP4
N/A	LET-502	Rho-binding kinase (ROCK)
N/A	MEL-11	Myosin Phosphatase (MYPT)
N/A	NMY-2	Myosin II
N/A	RGA-8	Rich1 SH3BP1 ARHGAP17 Nadrin
N/A	HUM-7	Myo9A Myo9B

CHAPTER 2: CDC-42 and the RhoGAP RGA-8 polarize myosin in the epidermis during ventral enclosure

Hamidah Raduwan^{1,2}, Andre G. Wallace³, and Martha C. Soto^{1,2}

¹Department of Pathology and Laboratory Medicine, Rutgers – RWJMS

²Cell and Developmental Biology Graduate Program, School of Graduate Studies,
Rutgers – RWJMS, Piscataway, NJ

³School of Natural Sciences, Fairleigh Dickinson University, Teaneck, NJ

HR performed all experiments and analysis unless otherwise mentioned.

AGW performed imaging analysis on Figure 10 and Figure 12C, D.

Abstract

Studies in *C. elegans* have established an essential role for CDC-42 to regulate non-muscle myosin II, NMY-2, during polarity establishment in the one cell embryo. CDC-42 and NMY-2/NMYII continue to regulate polarity in later embryos, but their contribution to the complex events of epidermal morphogenesis are less understood. Our studies of the epidermal enclosure have revealed an essential requirement for the GTPase CED-10/Rac1 and its effector, the WAVE/Scar complex, in promoting the protrusions that drive enclosure through activation of the branch actin regulator Arp2/3. Our analysis here of RGA-8, a homolog of SH3BP1/Rich1/ARHGAP17/Nadrin, with BAR and RhoGAP motifs, demonstrates it contributes to two events of epidermal morphogenesis, ventral enclosure and elongation. Genetic and molecular data show RGA-8 regulates CDC-42, in a pathway interacting with the transducer of cytokinesis (TOCA-1/2) and the CDC-42 effector WSP-1. These proteins affect levels of myosin in the migrating epidermal cells during ventral enclosure, and the timing of both enclosure and elongation. Two CDC-42 regulators with membrane-binding BAR domains, TOCA-1/2 and RGA-8, work together to ensure adequate levels of NMY-2/MyosinII in the migrating cells. We propose polarization of CDC-42 activity in the migrating cells supports the polarization of myosin that contributes to migration and cell shape changes of epidermal morphogenesis.

Introduction

Organ and tissue formation are highly regulated processes during embryonic development. During embryogenesis, epithelial cells must develop and maintain apicobasal polarity and healthy cell-cell junctions as they move past or over other tissues in the process of morphogenesis. Defects in this process can lead to birth defects or premature death. The complexity of vertebrate tissues complicates the study of organ and tissue embryonic development. Many studies are done *ex vivo* with simplified tissues, thereby factors such as tissue-tissue interaction, or tissue-extracellular matrix interaction are excluded from the analysis. Epidermal morphogenesis in the nematode *Caenorhabditis elegans* is an ideal model to study tissue morphogenesis. Tissue morphogenesis is well described in these transparent animals (3, 4, 91). In addition, *C. elegans* is amenable to genetics and microscopic observation, allowing live-imaging of the migrating tissues. While physical observations of this process have been described, the molecular proteins and signaling pathways involved are still poorly understood.

Epidermal morphogenesis in *C. elegans* can be divided into several stages. Epidermal cells are born at the posterior and dorsal side of the embryo and become arranged in three types of adjacent cells with distinct behaviors – two rows of dorsal cells, and on each side of the embryo, two rows of seam cells, and two rows of ventral cells. The right and the left row of ventral epidermal cells first form at the lateral edge of the epidermis. They migrate towards the ventral midline as a thin

adjacent sheet, over the neuroblasts, to enclose the internal organs, in a process termed ventral enclosure (1, 5). This tissue migration is led by the two anterior-most ventral cells on each side, the leading cells. The leading cells reach the ventral midline first, while the more posterior ventral cells, the pocket cells, undergo a purse-like constriction, to enclose the embryo on the ventral side. Simultaneously, the two dorsal rows undergo dorsal intercalation to generate a single row of cells, in a process analogous to the vertebrate convergent extension. Later, beginning at the ventral enclosure stage, the two rows of lateral seam cells undergo elongation, which increases their length along the anterior to the posterior axis, and decreasing along the dorsal/ventral axis, thus contributing to embryo length. This process requires actomyosin contractility (3, 4).

Actin nucleation and actomyosin contractility play essential roles during epidermal morphogenesis in *C. elegans* embryogenesis. The dynamics of actin and actomyosin contractility, in turn, are regulated by the Rho GTPases. Rho GTPases are molecular switches that cycle between the on and off state, depending on the status of its bound guanine nucleotide. Hydrolysis of GTP to GDP causes the GTPase to be inactive, and this is regulated by GTPase activating protein (GAP) family. In contrast, exchange of GDP with a new GTP causes the GTPase to be active, and this is regulated by the guanine exchange factor (GEF) protein (52, 55). Three main members of the Rho GTPase family members have been extensively characterized; their *C. elegans* and mammalian names are Rac1/CED-10, RhoA/RHO-1, and Cdc-42/CDC-42.

In *C. elegans*, the three main GTPases, Rac1/CED-10, CDC-42 and RhoA/RHO-1, have been shown to be involved in some aspects of epidermal morphogenesis. The ventral enclosure was initially shown to be dependent on actin (5), and subsequently shown to be regulated by Rac1/CED-10 GTPase acting on the WAVE/SCAR-dependent branched actin pathway (38, 39). In addition, Rac1/CED-10 can regulate dorsal intercalation (40), underscoring the important role played by CED-10/Rac1 in regulating the overall process of epidermal morphogenesis. Downstream of Rac-1/CED-10 is WAVE/Scar, a nucleation-promoting factor (NPF) that activates branched actin formation through Arp2/3 (38, 39, 92). In parallel to the CED-10/Rac1/WAVE pathway, branched actin can also be regulated by CDC-42 GTPase by recruiting the NPF WASP (92, 93). Studies using the *cdc-42* mutants in *C. elegans* have focused on the role of CDC-42 during the one cell-stage where it regulates cell division and differentiation (94, 95). Recently, Zilberman and colleagues mentioned a ventral enclosure defect in epidermal-specific *cdc-42* mutants, while focusing on its role during elongation of the embryo (96). In addition, CDC-42 was shown to have a role during dorsal intercalation (43). These reports suggest a role for CDC-42 during the overall epidermal morphogenesis process, but they do not reveal the mechanistic role of CDC-42 in the ventral enclosure.

WASP/WSP-1 is the NPF that is recruited and activated by CDC-42 to promote branched actin formation through ARP2/3 (32, 97, 98). Several reports support a role for CDC-42 and WASP/WSP-1 during ventral enclosure (92, 93). Oulette and colleagues characterized the role of CDC-42-dependent branched

actin pathway and showed RhoGAP-7/RGA-7 regulates CDC-42 during ventral enclosure in *C. elegans*. They found that RGA-7 and WASP/WSP-1 act antagonistically to regulate the protrusion rate of leading cells during ventral enclosure, calculated as the length vs. the width of the leading cells. Overexpression of CDC-42 caused a decreased protrusion rate of the leading-edge cells, with most of the embryos dying during ventral enclosure, suggesting a balance of active and inactive CDC-42 is required for efficient ventral migration (99). A regulator of CDC-42 and WASP/WSP-1 is transducer of cytokinesis-1, TOCA1. TOCA1 contains a GTPase binding domain (GBD) that binds to CDC-42, an SH3 domain that binds to the proline-rich region of WASP or other proteins, and an F-BAR domain that senses and binds to the curved membrane (77). *C. elegans* has two homologs of TOCA1, named TOCA-1 and TOCA-2, which were both implicated in epidermal morphogenesis of *C. elegans* (100). RGA-7 was also shown to regulate TOCA-1/2 for the formation of the actin-rich protrusion in leading-edge cells in an antagonistic manner (99). These suggest that the conserved pathway of branched actin regulation by TOCA-1/2-WASP-CDC-42 also regulates ventral enclosure during *C. elegans* morphogenesis.

Actomyosin contractility was shown to be important during *C. elegans* epidermal morphogenesis, specifically at the elongation stage (4, 10). Phosphorylation and dephosphorylation of the regulatory light chain MLC-4 by the LET-502/Rho-binding kinase (ROCK) and MEL-11/Myosin binding subunit of myosin phosphatase (MYPT), respectively, regulate the activity of nonmuscle myosin II (NMY-2). In addition, LET-502/ROCK and MEL-11/MYPT act

antagonistically during the elongation process, where LET-502/ROCK is expressed in the epidermal seam cells, while MEL-11/MYPT is expressed in the dorsal and ventral epidermis (45, 46). The *mel-11* mutant embryo exhibited hypercontractility, causing burst embryos due to increased tension on adherens junctions. The *let-502* mutant exhibited a defect in elongation of the embryo as well. Two additional kinases can contribute to maintaining myosin II activity; P21-activated kinase PAK-1 and CDC-42-activated kinase MRCK-1, both of which act in parallel to LET-502/ROCK. It was shown that MRCK-1 acts upstream of MEL-11, and that MRCK-1 is under the regulation of CDC-42 (47).

It is not clear what role actomyosin contractility plays during ventral migration or dorsal intercalation. One study showed the requirement for ANI-1, a multidomain protein that organizes actomyosin contractility, to ensure proper alignment of contralateral leading-edge epidermal cells meeting at the ventral midline. However, this study did not detect expression of ANI-1 in the epidermal cells, suggesting that this action might be delivered through the interaction between the underlying neuroblast (neuron precursors) with the migrating epidermal cells. Interestingly, *let-502* and *mel-11* mutants were reported to have embryonic lethality with a Gex phenotype, but no further analysis was done on the phenotype (11).

In this paper, we investigate a proposed novel regulator of CDC-42 during ventral enclosure in *C. elegans*. We identify the RhoGAP and BAR domain protein, RGA-8, as a regulator of CDC-42, based on genetic interactions. A *rga-8* null allele, *pj60* interacts genetically with *cdc-42*, and with the *toca-2(ng11);toca-1(tm2056)*

double mutant. Using RGA-8 endogenously-tagged via CRISPR with the mKate2 fluorescent protein, we found that RGA-8 is expressed in the epidermal cells and shows a polarized distribution in pharyngeal and intestinal epithelia. Surprisingly, the *rga-8* null mutant, *pj60*, and other regulators of CDC-42 results in reduced non-muscle myosin II (NMY-2::GFP) at the front of migrating epidermal pocket cells during ventral enclosure. We propose a model where RGA-8 regulates CDC-42, probably with TOCA-1/TOCA-2, to enrich and maintain polarized NMY-2::GFP accumulation at the epidermal pocket cells.

Results

RGA-8 is a GAP for CDC-42 that regulates *C. elegans* embryogenesis

To characterize the regulators of CDC-42 during epidermal morphogenesis, we screened the *C. elegans* family of GTPase activating proteins (GAPs), which inactivate and turn over the GTPases (54). To verify a defect in epidermal morphogenesis phenotype for CDC-42 pathway we used a *dlg-1::gfp* transgenic strain (Figure 6). We knocked down *cdc-42* via RNAi by expressing *cdc-42* double-stranded RNAi in L1 worms and waited 3 days. Under these conditions the RNAi knockdown resulted in over 80% embryonic lethality in their progeny, yielding the highest embryonic death during ventral enclosure stage at 35.9%, followed by elongation stage at 26.8%, and early differentiation at only 1% (Figure 6C). In vertebrates, CDC-42 regulates the actin cytoskeleton through the action of the Wiskott-Aldrich syndrome protein (WASP) and transducer of cytokinesis (TOCA-1). WASP/WSP-1 is a branched actin nucleation-promoting factor that remains inactive in folded form, masking the actin nucleation site. Binding of TOCA with CDC-42 releases the actin nucleation site on WASP/WSP-1, thereby inducing the formation of branched actin through the action of the branched actin nucleator Arp-2/3 complex (33, 97). Indeed, we saw death at both ventral enclosure and elongation for all mutants – *wsp-1(gm324)* at 20.3% and 4.9% respectively, *toca-2(ng11);toca-1(tm2056)* at 6% and 6.4% respectively (Figure 6C, Table 2).

We hypothesized that removing GAPs from *cdc-42* RNAi, which creates a hypomorphic *cdc-42* background, might rescue embryonic lethality. We focused

on one candidate CDC-42 GAP, named Rho-GTPase activating protein-8 (RGA-8). We generated an *rga-8* full deletion allele, *pj60*, using CRISPR and found it rescued *cdc-42 RNAi* embryonic lethality, from 84% to 65% (Figure 7, Table 3). Indeed, removing *cdc-42* by RNAi, *wsp-1*, *toca-2;toca-1* by genetic mutation also caused embryonic lethality at 85%, 17.9%, and 8.4% respectively (Figure 7).

To investigate which step of embryogenesis may be regulated by RGA-8, we crossed the *pj60* deletion mutant in the DLG-1::GFP transgenic background. *rga-8(pj60)*, resulted in 3% embryonic lethality. Another allele of this gene, *ok3242*, made by the *Caenorhabditis* Knock-Out Consortium, is a 611bp deletion that caused an initial frameshift and an eventual premature stop codon, resulting in the absence of a part of the GAP domain and the remainder of the C-terminus. Interestingly, the smaller deletion of this gene has a strong embryonic lethality, at 7% (5.5% in *dlg-1::gfp* background) (Figure 6C, Table 2). We used the null allele *pj60* to determine at which stage of embryogenesis requires RGA-8. By checking the *rga-8(pj60)* in *dlg-1::gfp* background, we determined that this mutant arrests during the ventral enclosure and elongation steps of morphogenesis (Figure 6C, D).

We investigated if RGA-8 interacted with known components of CDC-42 pathway: TOCA-1, TOCA-2, and WASP/WSP-1. When the *rga-8(pj60)* deletion was crossed to the *toca-2(ng11);toca-1(tm2056)* double mutant, we saw a rescue of embryonic lethality from 8.4% to 4.5% (Figure 7, Table 3). When using the *dlg-1::gfp* transgenic background, lethality was rescued from 13% to 6% (Figure 6C). We examined the specific stage of rescue, and found that *pj60* could rescue the

toca-2(ng11);toca-1(tm2056) arrest at both ventral enclosure and elongation stages of embryonic development, from 6% to 3.1%, and 6.4% to 2.1%, respectively (Figure 6C). Genetic doubles with *wsp-1(gm324)*, a known effector of *cdc-42* that regulates ventral enclosure (92), resulted in no change of embryonic lethality when combined with *rga-8(pj60)*, at approximately 11%, suggesting that WSP-1 acts downstream of RGA-8 (Figure 7, Table 3). Collectively, our results suggest that RGA-8 works with CDC-42 to regulate embryogenesis, possibly downstream of TOCA-1/TOCA-2 and upstream of WSP-1 to mediate the cytoskeletal dynamics.

RGA-8 potentially regulates RHO-1, but not CED-10/Rac1, during *C. elegans* morphogenesis

The homologs of RGA-8, SH3BP1, RICH-1, and NADRIN, are proposed GAPs for the GTPase Rac1. If RGA-8 was a GAP for the GTPase Rac1/CED-10, we expected it to rescue the hypomorphic allele of *ced-10, n1993*. Genetic doubles with *ced-10(n1993)* hypomorphic mutant did not affect the embryonic lethality when combined with *pj60* allele, as the lethality stayed at approximately 10% (Figure 7, Table 3). Similarly, embryonic lethality level in the double mutant with another *ced-10* hypomorphic allele, *n3246*, at 24.6%, was similar to the single mutant, at 22.8% (Table 3). Combining the *pj60* mutant with partial depletion of the Rac-1-dependent WAVE/WVE-1 protein, via *wve-1 RNAi*, (38), led to an enhancement of embryonic lethality, from 54.7% to 75% (Figure 7). This suggests

that RGA-8 may function in parallel with the Rac1-WAVE/SCAR branched actin pathway to mediate embryogenesis of *C. elegans*.

We tested RGA-8 genetic interactions with the RHO-1 pathway. Genetic doubles with a downstream effector of RHO-1 GTPase, the Rho Kinase (*let-502*), temperature sensitive allele, *sb118ts*, rescued lethality from 15% to 8% at the non-permissive temperature (25°C). This suggested loss of *rga-8* increases Rho-1 signaling. However, loss of *rga-8* also rescued lethality caused by a mutation in the myosin phosphatase, *mel-11 RNAi*, from 33% to 8% (Figure 7, Table 3), which could indicate loss of RGA-8 decreases RHO-1 signaling. This suggests that RGA-8 affects RHO-1 pathway but in a complicated manner. Collectively, we conclude that RGA-8 is a candidate GAP for CDC-42 since the loss of RGA-8 promotes CDC-42 pathway signaling. RGA-8 affects RHO-1 signaling, but it may not be a direct GAP for RHO-1 (Figure 7).

RGA-8 is expressed in epithelial cells with preferred localization at apical pharyngeal and intestinal cells.

To examine the expression pattern of RGA-8 in the embryo, we endogenously-tagged RGA-8 at the N-terminus with the red fluorescent marker, mKate2, using CRISPR technology (101) (Figure 8A). Visualization using a confocal spinning disk showed enrichment of RGA-8 at the apical region of two types of epithelial cells, the pharynx and the intestine (Figure 8C). This enrichment starts at approximately 240 min after the two-cell stage, as early as an enrichment of other apical markers, such as DLG-1. Apical enrichment of mKate2::RGA-8 is

maintained until adulthood. This localization pattern at apical regions of epithelia is similar to the transgenic marker, GFP::CDC-42 (Figure 8).

We first examined the subcellular localization of mKate2::RGA-8, relative to other proteins, at the apical intestine in L1 larvae. Viewing the images as cross-section projections (Methods), we found mKate2::RGA-8 is enriched all around the lumen of the intestine (Figure 8F-H). This is different than the localization of apical junction marker, DLG-1::GFP that localizes at two puncta that hold the two intestinal cells together (Figure 8G). The localization of mKate2::RGA-8 around the lumen of the intestine suggested RGA-8 might support the microvilli of the apical-most regions of the intestinal lumen. ERM-1 has been shown to localize in the apical intestine (102). Using animals doubly marked with ERM-1::GFP and mKate2::RGA-8, we found that RGA-8 localizes more basally than ERM-1::GFP, suggesting that RGA-8 is not found in the microvilli (Figure 8F). We compared the localization of RGA-8::mKate2 and ARP-2::GFP and found that ARP-2::GFP also localizes all around the apical side of the intestinal lumen. ARP-2::GFP appeared to be more basal and to surround a broader region around the lumen compared to mKate2::RGA-8 (Figure 8H). We conclude that RGA-8 localizes around the intestinal lumen, basal to the ERM-1::GFP apical-most domain and partially overlaps with ARP-2::GFP localization.

RGA-8 is expressed in the epidermal cells.

If RGA-8 were to regulate ventral enclosure, we expect RGA-8 may be expressed in the epidermis. Using a transgene that reports epidermal F-actin, *plin-*

26::Lifeact::gfp (103), we found that *mKate2::RGA-8* is expressed in the epidermal cells, and in regions where F-actin is enriched (Figure 8L). The localization in the epidermal cells is diffuse, with some enrichment on the cell membrane, based on partial overlap with an epidermal F-actin marker. RGA-8 in the epidermal cells localizes basally to *DLG-1::GFP* and co-localizes with CDC-42 and ARP-2 in the epidermal cells (Figure 8I-M). We conclude that RGA-8 is expressed in the epidermal cells, and it is enriched in regions that are also enriched with actin regulators.

RGA-8 localization relative to CDC-42

To test if RGA-8 colocalizes with active CDC-42, we compared *mKate2::RGA-8* to *GFP::CDC-42* (53) and a biosensor for active CDC-42, the G-binding domain of WSP-1, (GBD)WSP-1, transgenic marker ((96); Figure 9). *mKate2::RGA-8* and *GFP::CDC-42* co-localize together at the apical intestinal lumen (Figure 9A). In contrast to total *CDC-42::GFP* which is most enriched at the apical intestine, *WSP-1-GBD::GFP* is slightly reduced at the apical intestine, a complementary pattern to *RGA-8::mKate2* (Figure 9B). If RGA-8 is a CDC-42 GAP, it may be responsible for this apical reduction of active CDC-42. Therefore we crossed the *rga-8* null allele *pj60* into *GBD-WSP-1::GFP*, and found that the ratio of apical to lateral enrichment of *GBD-WSP-1::GFP* was reduced slightly but not significantly affected (Figure 9C).

GBD-WSP-1 is transiently enriched at cell junctions in the epidermis.

To test if mKate2::RGA-8 has specific localization in the epidermis, we compared the localization of both proteins in the dorsal epidermis (Figure 9D-E). Line scans through the dorsal cells during intercalation show mKate2::RGA-8 appears enriched at the medial tip of intercalating cells as GBD-WSP-1::GFP (Figure 9D'). This enrichment did not occur at all times (Figure 9D''), suggesting that RGA-8 is transiently enriched at the front tip of intercalating dorsal cells (Figure 9D). Similarly, we found RGA-8 is enriched on the cell membrane together with GBD-WSP-1::GFP, but not at all times (Figure 9E). This confirms that mKate2::RGA-8 is transiently enriched at cell-cell boundaries of the epidermal cells during intercalation (Figure 9D-E).

RGA-8 maintain apical enrichment in *cdc-42* mutant

Using the doubly marked GBD::WSP-1::GFP;mKate2::RGA-8, we checked if localization of both active CDC-42 and RGA-8 is affected. As expected, active CDC-42 localization was completely abrogated in *cdc-42 RNAi* mutant. The localization of mKate2::RGA-8 is maintained at apical enrichment in the intestine (Figure 9F).

Defects in CDC-42 pathway caused aberrant F-actin activity and levels in the epidermal cells.

Since RGA-8 is proposed to be a GAP for CDC-42, we postulated that removing *rga-8* will cause CDC-42 to be hyperactive. We measured the levels of F-actin in the epidermal cells using *plin-26::LifeAct::GFP* (103) and detected the

mutant *wsp-1(gm324)* caused an increase in F-actin level in the leading-edge cells as the cells are undergoing ventral enclosure. Similarly, depleting *cdc-42* via RNAi, and measuring embryos that differentiate epidermis using epidermal transgene controls (see Methods) showed that embryos depleted of *cdc-42* via RNAi also show elevated F-actin levels (Figure 10). Further, the *pj60* mutant also results in elevated F-actin levels in the leading cells. Therefore, the CDC-42 pathway appears to be required to maintain appropriate F-actin levels in the migrating epidermal cells.

Protrusions dynamics are not significantly affected by the CDC-42 pathway

Ouellette and colleagues showed decreased dynamics in *wsp-1* mutants, measured as how much the leading-edge membrane is displaced in the leading cells (99). In contrast, we examined the dynamic formation of protrusion and retractions at the leading edge. We detected no significant change, though the number of protrusions was slightly increased in *wsp-1* and *rga-8(pj60)* mutants (Figure 10). Therefore, the elevated F-actin levels may only slightly perturb dynamics.

Loss of *rga-8* reduces NMY-2/myosin II at the ventral region of epidermal pocket cells

While CDC-42 has been connected to the ventral enclosure, it is not clear which effectors of CDC-42 are responsible for this. CDC-42 regulates polarity (along with PAR-3/PAR-6/PKC) (104), cellular trafficking (through dynamin) (105),

actin nucleation (through WSP-1 and formins like DIA-1/CYK-1) and myosin contractility (through the myosin kinase MRCK-1) (47). Since changes in the *cdc-42* pathway altered F-actin levels and slightly affected dynamics, we examined if RGA-8 is involved in NMY-2/myosin II regulation during ventral enclosure. To this end, we measured the NMY-2/myosin II enrichment as the pocket cells meet at the ventral midline as a measure of epidermal myosin expression. Previously, it had been shown that myosin is enriched as puncta at the front of migrating epidermal pocket cells that later converge at the ventral midline as the contralateral pocket cells meet (12, 106). When the pocket cells first meet, NMY-2/myosin II enrichment is high, but then reduced to the basal level as the embryo further elongates (Figure 11). We measured levels of NMY-2/myosin II at the first meeting of the contralateral pocket cells, as previously reported (12). We first measured the level of NMY-2/myosin II level in animals depleted of the CDC-42 pathway, using the mutant *wsp-1(gm324)*. We found that *cdc-42* RNAi did not cause a detectable difference in the level of NMY-2/myosin II in the migrating pocket epidermal cells. However, we found that the mutant, *wsp-1(gm324)*, caused a reduction of 20% compared to wild type. Similarly, we found that the null mutant *rga-8(pj60)* caused a 40% reduction compared to wild type. Interestingly, removing both TOCA-1 and TOCA-2 did not cause any effect on NMY-2/myosin II enrichment, but removing all three in *toca-2(ng11); toca-1(tm2016) rga-8(pj60)* triple mutant restored the level of NMY-2/myosin II back to wild type levels. Surprisingly, the proposed gain-of-function allele of *rga-8*, *ok3242*, caused a 30% increase in myosin II/NMY-2, the opposite of the null mutation *pj60* (Figure 11A, B). We compared the localization

of NMY-2::GFP and mKate2::RGA-8 when the contralateral pocket cells meet at the ventral midline. Indeed, we saw co-localization of both proteins at the front of each contralateral pocket cells when they meet at the ventral midline (Figure 11C). We concluded that RGA-8 regulates the accumulation of myosin II/NMY-2 at the epidermal pocket cells.

RGA-8 regulates the rate of enclosure of the migrating epidermal cells

Since *rga-8(pj60)* mutants affect the level of myosin at the pocket cells, we sought to understand if RGA-8 also controls myosin in the leading-edge cells. NMY-2::GFP marks all NMY-2/myosin II in the embryos, however, so we couldn't faithfully see the leading-edge epidermal cells without the presence of a second marker that demarcates epidermal cells from other cells. Attempts to build the epidermal *Lifeact::mCherry; nmy-2::gfp; rga-8(pj60)* triple strain were unsuccessful since *pj60* is located close to the *LifeAct::mCherry* locus on the X chromosome. Instead, we used the rate of migration as a phenotypic readout. By measuring from the time of the first protrusion to the first meeting at the ventral midline for the contralateral leading-edge cells, we found that *rga-8(pj60)* epidermal leading-edge cells migrate at a slower rate (48min) compared to the wild type (24min) (Figure 12). Therefore, *rga-8* mutant caused the ventral enclosure rate to be slower compared to wild type.

RGA-8 regulates late elongation stage during epidermal morphogenesis of *C. elegans*

C. elegans elongation during epidermal morphogenesis can be divided into two stages. First, early elongation occurs immediately after ventral enclosure until around 1.7-fold stage and this is regulated primarily by actomyosin contractility (Figure 11). The second, late elongation occurs after the 1.7-fold stage, and this is regulated primarily by the underlying muscle cells (10). We checked to see if the *rga-8(pj60)* null mutant affects the late elongation stage of epidermal morphogenesis using live imaging. Our movies showed that *pj60* resulted in faster elongation specifically beginning at the 1.7-fold stage (Figure 12). While wildtype embryos incubated at 23°C for 7.5 hours were at the 2-fold stage, *pj60* embryos at 7.5 hours had already reached the 3-fold stage (Figure 12). Overall, we concluded that RGA-8 regulated the rate of epidermal morphogenesis in a stage-specific manner.

Table 2 Embryonic lethality count for the respective mutants, represented in

Figure 6.

Genotype	Alive	Death			n=
		Early	Gex	Late	
<i>dlg-1::gfp</i>	1154	0	5	5	1164
<i>cdc-42 (RNAi); dlg-1::gfp</i>	76	2	75	56	209
<i>rga-8(pj60); dlg-1::gfp</i>	457	2	0	0	459
<i>rga-8(ok3242); dlg-1::gfp</i>	483	6	20	2	511
<i>wsp-1(gm324); dlg-1::gfp</i>	463	15	130	31	639
<i>toca-2(ng11); toca-1(tm2056); dlg-1::gfp</i>	202	2	14	15	233
<i>toca-2(ng11); toca-1(tm2056) rga-8(pj60); dlg-1::gfp</i>	481	5	16	11	513

Lethality count was done on plates containing embryos after incubation of L4

larvae for 4 days for mutants, or L1 larvae for 3 days for RNAi experiment. All

experiments were done at 23°C.

Table 3 Embryonic lethality count for the respective mutants, represented in Figure 7.

Genotype	Temp	Alive	Death	n=	% Lethality
<i>N2</i>	23°C	641	1	642	0.16
<i>N2; L4440 (RNAi)</i>	23°C	1148	21	1169	1.80
<i>N2; rga-8(RNAi)</i>	23°C	1323	20	1343	1.49
<i>rga-8(pj60)</i>	23°C	210	4	214	1.87
<i>rga-8(ok3242)</i>	23°C	432	31	463	6.70
<i>rga-8(pj60); L4440 (RNAi)</i>	23°C	1214	24	1238	1.94
<i>ced-10(n1993)</i>	23°C	633	75	708	10.59
<i>ced-10(n1993); rga-8(pj60)</i>	23°C	571	67	638	10.50
<i>ced-10(n3246)</i>	23°C	598	177	775	22.84
<i>ced-10(n3246); rga-8(pj60)</i>	23°C	525	171	696	24.57
<i>N2; wve-1 (RNAi)</i>	23°C	120	145	265	54.2
<i>rga-8(pj60); wve-1 (RNAi)</i>	23°C	63	189	252	75.00
<i>N2; cdc-42 (RNAi)</i>	23°C	67	379	446	84.98
<i>rga-8(pj60); cdc-42 (RNAi)</i>	23°C	144	312	456	68.42
<i>toca-2(ng11); toca-1(tm2056)</i>	23°C	294	27	321	8.41
<i>toca-2(ng11); toca-1(tm2056) rga-8(pj60)</i>	23°C	407	19	426	4.46
<i>wsp-1(gm324)</i>	23°C	637	139	776	17.91
<i>wsp-1(gm324); rga-8(pj60)</i>	23°C	761	172	933	18.44
<i>N2^a</i>	20°C	161	3	164	1.83
<i>rga-8(pj60)^a</i>	20°C	278	4	282	1.42
<i>let-502(sb118ts)^a</i>	20°C	373	6	379	1.58
<i>let-502(sb118ts); rga-8(pj60)^a</i>	20°C	313	3	316	0.95
<i>N2^a</i>	25°C	317	5	322	1.55
<i>rga-8(pj60)^a</i>	25°C	367	5	372	1.34
<i>let-502(sb118ts)^a</i>	25°C	368	61	429	14.22
<i>let-502(sb118ts); rga-8(pj60)^a</i>	25°C	358	32	429	8.21
<i>N2; mel-11 (RNAi)^b</i>	23°C	554	243	797	30.49
<i>rga-8(pj60); mel-11(RNAi)^b</i>	23°C	671	61	732	8.33
<i>unc-40(n324)</i>	23°C	101	804	905	11.2
<i>unc-40(n324); rga-8(pj60)</i>	23°C	132	804	936	14.1
<i>vab-1(dx31)</i>	23°C	583	733	1316	44.3

<i>vab-1(dx31); rga-8(pj60)</i>	23°C	570	575	1145	49.8
<i>sax-3(ky123)</i>	23°C	158	341	499	31.7
<i>sax-3(ky123); rga-8(pj60)</i>	23°C	218	358	576	37.9
<i>unc-34(e315)</i>	23°C	488	7	495	1.41
<i>unc-34(e315); rga-8(pj60)</i>	23°C	549	19	568	3.35
<i>sax-7(eq1)</i>	23°C	346	5	351	1.42
<i>sax-7(eq1); rga-8(pj60)</i>	23°C	356	1	357	0.28

Lethality count was done on plates containing embryos after incubation of L4 larvae for 4 days for mutants, or L1 larvae for 3 days for RNAi experiment at 23°C, unless otherwise indicated.

^a Lethality counts were done after plating L4 hermaphrodites for one day at the respective temperature

^b Lethality counts were done after plating L4 hermaphrodites for two days on the respective RNAi

Discussions

RGA-8 regulates CDC-42 pathway during epidermal morphogenesis in *C. elegans*

In this study, we focused on the role of CDC-42 on the ventral enclosure and addressed two key biological questions – (1) which GTPase activating protein (GAP) interactor of CDC-42 that regulates ventral enclosure, and (2) which downstream pathway of CDC-42 does the GAP protein control. We found a GAP, RGA-8, functions together with CDC-42 to regulate ventral enclosure by regulating the level and dynamics of actin and non-muscle myosin (NMY-2) in the epidermal cells. To uncover an inactivating signal for the GTPase CDC-42, we screened 23 GAPs candidate in *C. elegans* (54) for embryonic lethality rescue of the *cdc-42 RNAi* hypomorphic mutant. We found a GAP, RGA-8, has a role in regulating CDC-42 based on *cdc-42 RNAi* lethality rescue on *rga-8* null allele, *pj60*. The mutant *pj60* can also rescue the lethality of *toca-2(ng11);toca-1(tm2056)* double mutant, a well-known interactor of CDC-42 to regulate branched actin pathway via the action of WSP-1/WASP (97). Interestingly, *wsp-1(gm324); rga-8(pj60)* double mutants resulted to the same embryonic lethality as *wsp-1(gm324)* mutants, which could indicate *wsp-1* is epistatic to *rga-8*. Collectively, our genetics data suggests that WSP-1 functions downstream of TOCA-1/TOCA-2 and RGA-8 (Figure 2).

We found that the lethality caused by an *rga-8* null allele made in the lab using CRISPR, *pj60*, to be mild for embryonic lethality, while all the animals showed changes in developmental timing and NMY-2/myosin II levels. The small

deletion, the *ok3242* allele, had significant embryonic lethality, at approximately 7%, and some phenotypes, like the effects on myosin, were opposite to complete loss of RGA-8 (Figure 6, 10). From the observation on the embryonic lethality of the null allele, we proposed that; (1) RGA-8 plays an ancillary role in regulating CDC-42 and that there might be other GAPs that work together with RGA-8, and (2) *ok3242* allele might be a gain of function allele. Our attempts to identify another GAP that works in parallel with RGA-8 using RNAi depletion were unsuccessful, but RNAi is not always effective at depleting all genes. It is also possible that more than two GAPs are working together with RGA-8 to regulate CDC-42 during the process of ventral enclosure.

Alternative pathways work together with RGA-8 to regulate CDC-42 during epidermal morphogenesis in *C. elegans*

The GTPase activating protein (GAP) family consists of many members that regulate members of the RHO-GTPase family. In *C. elegans*, there are only 7 members of the RHO-GTPase in comparison to 23 GAPs (54). Numerous studies have contributed to our understanding on how different GAPs work on the RHO-family GTPases in *C. elegans* during two-cell polarity and cytokinesis (94, 95), clearance of cell death (54), as well as epidermal morphogenesis (99, 107). However, the function of the majority of the *C. elegans* GAP proteins is still unknown. This could be due to the mild phenotypes when these GAPs are removed from the system. Some studies, therefore, use overexpression of these GAPs to investigate their function. In disease studies, GAPs are often over-

expressed, rather than missing. For example, high expression of RacGAP (also named MgcRacGAP) is associated with more advanced epithelial ovarian tumor (108), bladder cancer (109), gastric cancer (110), and colorectal cancer (111). These examples underscore the importance of careful study of the regulatory role of GAPs members, even if there is limited or mild phenotype in the null mutants.

RGA-8 regulates RHO-1

RGA-8 has four close human homologs, which are SH3-binding protein 1 (SH3BP1), RhoGAP-interacting with CIP4 homologs (Rich1/Rich2), ARHGAP17 and Nadrin. SH3BP1 and RICH-1 were first discovered as proteins that interact specifically with the SH3 domain of TOCA-2/1 and CIP4, respectively, via their C-terminus proline-rich domain. Both SH3BP1 and Rich1/Rich2 have been shown to interact with Rac1 and Cdc42, but not RhoA. RGA-8 genetic interactions with regulators of RHO-1 and CDC-42, but not Rac1/CED-10, contradicts what has been found for RGA-8 homologs, which typically interact with Rac1 and CDC-42, but not RhoA/RHO-1. The regulation of RHO-1 is especially intriguing since *rga-8(pj60)* can suppress the lethality of both *mel-11 RNAi* and *let-502(sb118ts)*. *C. elegans* contains only one Rho GAP that contains an N-terminus BAR domain, followed by GAP domain, and C-terminus proline-rich region, while humans have three paralogs. Therefore, the *C. elegans* homolog may have evolved different roles compared to its homologs throughout evolution.

Alternatively, our study was done *in vivo*, suggesting that crosstalk between different pathways and tissues are pertinent to the overall regulation of cell

migration. What we see as genetic interaction with RhoA/RHO-1 and CDC-42 might indicate a masked phenotype due to the interaction between several interconnected pathways, and in several types of tissues, which is a point that might have been missed when the study was done on tissue culture. Indeed, ANI-1 was shown to only express in the neuroblast, yet phenotypically showed failure for epidermal cells to undergo ventral enclosure during epidermal morphogenesis, but *rho-1* mutant was also shown to regulate ventral enclosure and was expressed in all cell types, including the epidermis (11). In addition, LET-502 was shown to be highly enriched in the seam cells, while MEL-11 was shown to be highly enriched in the dorsoventral cells. This suggests a different RhoA/RHO-1-dependent regulatory pathway even in the subset of epidermal cells. The fact that we see a rescue in embryonic lethality for both mutants of *let-502* and *mel-11* suggests that regulation of RGA-8/SH3BP1/RICH-1 on RHO-1/RhoA is not straightforward. Careful dissection on how actin and actomyosin contractility works in the different type of cells during epidermal morphogenesis will be required, and *C. elegans* will serve as an attractive model for future studies to elucidate the role of tissue-tissue interaction in regulating cell migration.

Defective CDC-42 pathway resulted in aberrant actin phenotype

A well-known function of CDC-42 is to regulate branched actin dynamics via the WASP/WSP-1 protein. Knockdown of *cdc-42* by RNAi caused many embryos to have a ventral enclosure defect, most epidermal cells completely failed to migrate, resulting in a fully penetrant Gex phenotype. We used the mutant, *wsp-*

1(gm324), as a readout for a defect in the CDC-42 branched actin pathway. In *wsp-1(gm324)* we found elevated levels of actin as the leading-edge epidermal cells migrate towards the ventral midline. Similarly, *cdc-42 RNAi* also caused an increase in F-actin level at the leading-edge cells. Both of the mutants, however, did not affect the protrusion or retraction rates of the leading-edge cells (Figure 9). In addition, we did not detect changes in F-actin levels and dynamics in *toca-2(ng11);toca-1(tm2056)* double mutant when measured with *plin-26::LifeAct::GFP* transgenic strain. However, we detected elevated F-actin levels in *rga-8(pj60)* and in the triple mutant *toca-2(ng11);toca-1(tm2056)rga-8(pj60)*, while F-actin dynamics appeared elevated but not significantly so (Figure 10).

We reason that, in our system, TOCA-2/TOCA-1 and RGA-8 control different populations of CDC-42-regulated F-actin. This appears contrary to reports in other systems that TOCA-2/TOCA-1 regulates branched actin formation through WASP/WSP-1. Alternatively, TOCA-2/TOCA-1-WASP/WSP-1 regulated branched actin pathway could play a redundant role during ventral epidermal enclosure in *C. elegans*. This is consistent with a highly penetrant Gex phenotype previously reported for Rac1/CED-10-WAVE/SCAR pathway (38, 39), suggesting that the WAVE/SCAR pathway plays the central role for the epidermal enclosure. Interestingly, TOCA-2/TOCA-1 had also been shown to be able to bind to part of the WAVE/SCAR complex, WVE-1 and ABI-1 (100), suggesting potential crosstalk between the WAVE/SCAR pathway and WASP/WSP-1 pathway in regulating branched actin formation. In addition, CDC-42 had also been shown to regulate

linear F-actin formation through the action of the formin protein family. It is possible that RGA-8 might control linear F-actin pathway in CDC-42-dependent manner.

RGA-8 regulates NMY-2/ myosin II accumulation during pocket cell migration

Surprisingly, we see lower myosin accumulation on the membrane front when the epidermal pocket cells meet at the ventral midline in the *rga-8(pj60)* mutant (Figure 11). However, we did not see any change in myosin accumulation in the *toca-2(ng11);toca-1(tm2056)* double mutant and *toca-2(ng11);toca-1(tm2056)rga-8(pj60)* triple mutant (Figure 11). Similarly, we also see a low level of NMY-2/myosin II at the membrane front of the epidermal pocket cells in *wsp-1(gm324)*. This can be interpreted in several ways. First, RGA-8 may be required for the negative feedback loop to attenuate branched actin formation by the TOCA-2/1 pathway, in order to give way for myosin accumulation as the epidermal cells move or elongate. When RGA-8 is removed from the system, RGA-8 could either fail to signal to stop branched actin formation or to allow for myosin accumulation. However, we do see a decreased myosin accumulation at the membrane front of migrating pocket cells in *wsp-1(gm324)* mutant, suggesting that the N-WASP/WSP-1-dependent branched actin pathway is needed to potentiate myosin accumulation at this localization, but not necessarily needed for the accumulation of myosin on the membrane itself.

Finally, while the role of actomyosin contractility has been extensively characterized during elongation and early cell division, it is not clear what role it plays during ventral enclosure. However, branched actin pathway has been

extensively shown to be involved during ventral enclosure. Our analysis on myosin behavior in epidermal cells suggested that myosin plays a role during epidermal cell migration during ventral enclosure. Interestingly, Oulette and colleagues reported that overexpression of RhoA/RHO-1 had little effect on the protrusion rate of leading-edge cell migration but caused an increased in pocket cells protrusion rate. Instead, overexpression of CDC-42 caused a decreased protrusion rate of leading-edge cell migration, resulting in delayed ventral enclosure (99). Similarly, loss of *rga-8* resulted in delayed leading-edge cells migration during ventral enclosure. This suggests that myosin activity during ventral epidermal enclosure could be under the control of CDC-42 and RGA-8. It will be interesting to measure epidermal myosin behavior in the epidermal-specific mutation of CDC-42 to ascertain that CDC-42 in the epidermal cells affect epidermal myosin.

We could not differentiate an epidermal myosin signal from a neuroblast signal while the epidermal cells are migrating due to the high NMY-2/myosin II expression in the underlying neuroblasts. We addressed this issue by using a doubly-marked strain of epidermal F-actin with the endogenously tagged NMY-2::GFP in our previous publication (12). However, we could not cross *plin-26::LifeAct::mCherry* (103) with *rga-8* mutant, suggesting that the transgenic marker *plin-26::Lifeact::mCherry* is integrated near *rga-8* locus on the X chromosome. In the future, it would be interesting to study the behavior of epidermal cells when NMY-2/myosin II is removed specifically in the epidermal cells. In addition, epidermal-specific expression of myosin will allow us to look for the pattern of NMY-2/myosin II expression and localization as the epidermal cells

migrate during morphogenesis without background signals from the underlying neuroblast. Our study raised new questions regarding the regulation of tissue morphogenesis, and we look forward to new discoveries to dissect the molecular regulation of tissue morphogenesis in *C. elegans*.

Materials and Methods

Strains table. All strains were grown and maintained at 23°C using the original worm culture condition unless otherwise mentioned (91). Strains were either collected from CGC, which is funded by NIH Office of Research Infrastructure Programs (P40 OD010440), and National Bio-Resource Project of the MEXT Japan as denoted as NBRP, or gifted by the individual lab where the strains were generated. All strains used in this study are listed in Table 4.

Table 4 All strains used in this study

Strain Name	Genotype	Source
N2	<i>Wild type</i>	CGC
NG0324	<i>wsp-1(gm324)</i>	CGC via (93)
MT5013	<i>ced-10(n1993)</i>	CGC
HR1157	<i>let-502(sb118ts)</i>	Paul Mains
	<i>toca-2(ng11); toca-1(tm2056)</i>	CGC, NBRP, via (100)
OX680	<i>rga-8(pj60)</i>	This study
OX808	<i>rga-8(pj71)</i>	This study
OX768	<i>wsp-1(gm324); rga-8(pj60)</i>	This study
OX711	<i>ced-10(n1993); rga-8(pj60)</i>	This study
OX794	<i>let-502(sb118ts); rga-8(pj60)</i>	This study
OX748	<i>toca-2(ng11); toca-1(tm2056) rga-8(pj60)</i>	This study
RB2384	<i>rga-8(ok3242)</i>	CGC
OR113	<i>dlg-1::gfp; rol-6(su1006)</i>	Rongo Lab at Rutgers
OX725	<i>dlg-1::gfp; rol-6(su1006); rga-8(pj60)</i>	This study
OX785	<i>dlg-1::gfp; rol-6(su1006); rga-8(ok3242)</i>	This study
OX749	<i>dlg-1::gfp; rol-6(su1006); toca-2(ng11); toca-1(tm2056) rga-8(pj60)</i>	This study
OX	<i>dlg-1::gfp; rol-6(su1006); toca-2(ng11); toca-1(tm2056)</i>	This study
OX	<i>dlg-1::gfp; rol-6(su1006); rga-8(pj71)</i>	This study

OX787	<i>pjEx69[plin-26::GFP- rga-8]</i>	This study
OX684	<i>rga-8(pj66[mKate2::FLAG:: rga-8 + LoxP])</i>	This study
VJ402	ERM-1::GFP	Verenal Gobel 2007
	HMP-1::GFP	Goldstein lab
OX724	<i>rga-8(pj66[mKate2::FLAG:: rga-8 + LoxP]); dlg-1::gfp; rol-6(su1006)</i>	This study
OX734	<i>rga-8(pj66[mKate2::FLAG:: rga-8 + LoxP]); erm-1::gfp</i>	This study
OX726	<i>rga-8(pj66[mKate2::FLAG:: rga-8 + LoxP]); hmp-1::gfp</i>	This study
OX721	<i>rga-8(pj66[mKate2::FLAG:: rga-8 + LoxP]); arp-2::gfp</i>	This study
OX747	<i>rga-8(pj66[mKate2::FLAG:: rga-8 + LoxP]); nmy-2::gfp</i>	This study
WS4700	<i>opls295 [cdc-42p::GFP::cdc-42(genomic)::cdc-42 3'UTR + unc-119(+)]</i>	(53) via CGC
FT1459	<i>unc-119(ed3); xnls506 [cdc42P::gst-gfp-wsp-1gbd, unc-119(+)]</i>	(96)
OX762	<i>rga-8(pj66[mKate2::FLAG:: rga-8 + LoxP]); opls295 [cdc-42p::GFP::cdc-42(genomic)::cdc-42 3'UTR + unc-119(+)]</i>	This study
OX832	<i>rga-8(pj66[mKate2::FLAG:: rga-8 + LoxP]); unc-119(ed3); xnls506 [cdc42P::gst-gfp-wsp-1gbd, unc-119(+)]</i>	This study
	<i>pend-1::vab10abd::gfp</i>	(112)
JUP30	<i>unc119(ed3); ls[Plin-26::Lifeact::GFP::unc54 3'UTR; Cb-unc119]</i>	(103)
	<i>NMY-2::GFP</i>	Goldstein lab
OX732	<i>NMY-2::GFP; rga-8(pj60)</i>	This study
OX803	<i>NMY-2::GFP; rga-8(ok3242)</i>	This study
OX846	<i>NMY-2::GFP; toca-2(ng11); toca-1(tm2056)</i>	This study
OX855	<i>NMY-2::GFP; toca-2(ng11); toca-1(tm2056) rga-8(pj60)</i>	This study

Strains generation using CRISPR. The best PAM site was searched around the desired region with the help of <http://crispr.mit.edu/> website from MIT as a guide ((113), Zhang lab). Plasmids containing the guide RNA (gRNA) were made using either sewing PCR method with the primers MSo1204-1205, MSo1304-1305 and MSo1367-1340 (114), or traditional plasmid digestion and ligation using the

primers MSo1585-1586 (115). To ensure cutting efficiency, the gRNAs were tested on wild type worms prior to use for generating specific mutant strains using co-CRISPR injection strategy (115).

To generate tagged genes, we used the plasmid rescue method from the Goldstein lab that uses hygromycin antibiotic as a powerful selection against successful cutting and recombination events (101). Briefly, the 5' flanking arms were generated using primers MSo1402-1403 and the 3' flanking arms were generated using primers MSo1404-1405. Both arms were cloned into the pDD285 vector using Gibson assembly kit from NEB (116), Cat# E2611.

To generate deletion mutants, we used the co-CRISPR method by the Fire lab to select for worms that have a successful Cas9 cutting event (115). To generate full deletion, verified sgRNAs that were able to cut at the beginning and the end of the *Y34B4A.8* were co-injected with sgRNA targeted to *dpy-10*. Cutting of Cas9 on *dpy-10* locus will yield an observable phenotype on the dissecting microscope. Strain isolates were then checked using PCR genotyping procedure.

To generate specific point mutants, verified sgRNA and rescue oligos containing the desired point mutation as well as mutated PAM site were co-injected with *dpy-10* sgRNA. A silent mutation that inserts a new *Ava*I restriction enzyme site is also engineered on the rescue oligos (MSo1602) to ease the screening process of identifying the mutants.

All genetically engineered strains with resultant phenotype were singled out on separate plates and let to reproduce. Further DNA sequencing was done to verify

the mutations and inserts for all strains. All strains were backcrossed to wild type for at least three times to minimize possible off-target effects by the gRNAs and Cas9. Primers used for strain generation are listed in Table 5.

Table 5 List of DNA primers used in this study to generate knockout and tagged RGA-8 using the CRISPR method

MSo#	DNA Sequence	Comments
1204	TGAATTCCTCCAAGAACTCG	CMo16428 in (114)
1205	AAGCTTCACAGCCGACTATG	CMo16429 in (114)
1304	GGCTTTTACAGGTAAAATGGGT TTTAGAGCTAGAAATAGC	sgRNA construct, 5'
1305	CCATTTTACCTGTAAAAGCCAA ACATTTAGATTTGCAATTC	sgRNA construct, 5'
1367	GGAACCTTTGTGTCAGTTAGGT TTTAGAGCTAGAAATAGC	sgRNA construct, 3'
1368	CTAACTGACACAAAGGTTCCAA ACATTTAGATTTGCAATTC	sgRNA construct, 3'
1369	GCTCGGAATGGATATTGAAGG TTTTAGAGCTAGAAATAGC	sgRNA construct, 3'
1370	CTTCAATATCCATTCCGAGCAA ACATTTAGATTTGCAATTC	sgRNA construct, 3'
1402	acggtgtaaacgacggccagtcgccggca <u>GGTAGGTTTTGTTGGTAGCG</u>	Tagged Y34B4A.8, rescue construct, 5' arm
1403	CATGTTTTCTTTAATGAGCTCG GAGACCAT <u>CATTTTACCTGTAA</u> <u>AAGCGGC</u>	Tagged Y34B4A.8, rescue construct, 5' arm
1404	CGTGATTACAAGGATGACGAT GACAAGAGAG <u>GAGGTTGGGCAT</u> <u>CGTTTCAG</u>	Tagged Y34B4A.8, rescue construct, 3' arm
1405	tcacacaggaaacagctatgacctgttat <u>C</u> <u>TGTGCAGGCAACTCGTTTG</u>	Tagged Y34B4A.8, rescue construct, 3' arm
1585	TCTTG <u>GTGGACGCGTTTCCGC</u> <u>TGACT</u>	sgRNA for R277A mutation
1586	AAACAG <u>TCAGCGGAAACGCGT</u> <u>CCAC</u>	sgRNA for R277A mutation
1602	GTGATTTCTTCGGCAGAATGG AATGAATGAACGGGGTATCTTC <u>GCTGTCTCGGAAACGCGTCC</u>	R277A mutation rescue oligos. Bolded and underlined text is the R277A mutation. Bolded text is the

	AAAATCAAAGAATCCGCGCTG CCTTGGATGCTG	silent mutation to generate Aval restriction site.
--	---------------------------------------	--

Embryonic lethality count and statistical analysis. For RNAi-treated samples, bacteria expressing double-stranded RNA that is homologous to the desired gene were used to knockdown gene expression via feeding (117, 118). Most RNAis were obtained from the Driscoll lab library at Rutgers University or generated in the lab. RNAi feeding experiments were done at 23°C unless otherwise mentioned. Worms were synchronized and transferred onto a seeded plate containing RNAi-expressing bacteria corresponding to our genes of interest. Embryos were scored for lethality at either 48 hours (for *mel-11* RNAi) or 72 hours (for all other genes) after treatment. For genetic mutants, all strains were grown at 23°C on nematode growth media plate. Embryos were mounted on 3% agarose pad and scored for embryonic lethality.

Fluorescent imaging of live embryo. All imaging was done on Laser Spinning Disk Confocal Microscope with Yokogawa scan head on a Zeiss AxioImager Z1m Microscope. Images were captured on a Photometrics Evolve 512 EMCCD Camera using MetaMorph software. Live imaging was done at 40X magnification using 1.3NA oil immersion objective lens. Imaging was done in a temperature-controlled room that was set at 23°C. 2 to 4-cell stage embryos were dissected out from mother and mounted on 3% agarose pads. Z stacks were made across the entire embryo using motorized z-stage, approximately 27 to 32 z-stacks total, at 1µm intervals. The respective wild type that was imaged within the range of 3

days and with the same imaging condition were used as a control for each dataset to account for technical variability.

Imaging of NMY-2::GFP. Embryos were exposed at 30% laser power for 100ms at every 10 minutes for 2 hours in wild type. All mutants were imaged for 2 hours, similar to wild type, except for *mel-11* mutants, which were imaged for 3 hours.

Data analysis: The stage where the epidermal pocket cells had met at the ventral midline were selected, and rectangular box surrounding the pocket epidermal cells were drawn, and maximum intensity value was measured, similar to (12). At least five embryos were measured for every mutant (refer to specifics in the figure). Two-way ANOVA was performed to measure p-value with Bonferroni correction.

Figure Legends

Figure 6 CDC-42 controls morphogenesis in *C. elegans*.

(A) Cartoon representation of the process of epidermal morphogenesis in *C. elegans*. Purple represents the seam cells, and pink represents the ventral cells. In wild type, the ventral cells migrate to enclose the embryo, followed by an increase in length along the anterior to posterior axis of the seam cells (white double arrow). In the mutant, an increase of tension along the junction in the seam cells caused the embryo to burst and extrude internal cells (white arrow). (B) Representative time-lapse images of differential interference contrast (DIC, top row), and *dlg-1::gfp* fluorescence image (bottom row, marks three epithelial tissue - epidermal, intestinal and pharyngeal tissues) transgenic background of wild type embryo. **Pink line** signifies the start of *dlg-1::gfp* expression during which the epithelial cells are born, and ventral epidermal cells need to migrate towards the ventral midline, and dorsal epidermal cells need to undergo intercalation. These processes occur around 270min to 400min post-fertilization, and embryos that died during this time is termed to die during ventral enclosure and called gut on the exterior (Gex) phenotype. The **purple line** indicates the completion of the epidermal enclosure of all internal tissues in *C. elegans* and the start of constriction along the circumference of the worms and the stretching along the anteroposterior axis to elongate the worms to the right size. This occurs starting from 400min until hatching, and embryos that died during this period is referred to die during the elongation stage. Representative images for defective embryos for the respective

genotype in the last two columns for *wsp-1(gm324)* and *rga-8(pj60)*. (C) Percentage of embryonic lethality for respective stages described in B on *dlg-1::gfp* background for *cdc-42(RNAi)* (n=209), *toca-2(ng11);toca-1(tm2056)* (n=219), *rga-8(ok3242)* (n=511), *wsp-1(gm324)* (n=639), and *toca-2(ng11);toca-1(tm2056)rga-8(pj60)* (n=513) mutants for embryos that died during ventral enclosure (red) and elongation (purple) stage. (D) The intestinal phenotype for various mutants of *rga-8* is shown.

Figure 7. RGA-8, a GTPase activating protein (GAP), regulates CDC-42 and RHO-1, but not CED-10/Rac1.

Percentage embryonic lethality was scored for each genetic background on plates abundant with embryos. Embryos were collected and mounted on 3% agarose pad on glass slides to score for embryonic lethality under differential interference contrast (DIC) microscope. The n listed is the number of embryos scored for each genotype. Fisher's exact test was done to calculate significant. NS = not significant, and the p-values are listed. All worms are grown at 23°C unless otherwise indicated, as denoted in the blue box for 20°C and 25°C.

Figure 8. RGA-8 is enriched on the membrane in the epidermis and apically-enriched in the intestine.

(A) RGA-8 is endogenously tagged using CRISPR/Cas9 at N-terminus using red variant fluorescence marker, mKate2. (B-D) DIC and fluorescence image of the representative WT at approximately 240 minutes at the top row, and 360 minutes

at the bottom row. (B) DIC image representation of WT. The pattern of (C) mKate2::RGA-8, and (D) GFP::CDC-42 expression in WT embryo. (E) Cartoon representation of how images on (F-H) were generated. L1 larvae were imaged every 1 μ m across the entire circumference of the worm. Line scan was made, and all z-section was reconstructed to generate a cross-section of the larvae intestine. Cross section of mKate2::RGA-8 in the intestine of L1 larvae against (F) ERM-1::GFP, (G) DLG-1::GFP, and (H) ARP-2::GFP. (I) Close-up image of the epidermal cells from embryos at the stage where the embryo had successfully undergone ventral enclosure. Grey box indicates the region used to check for mKate::RGA-8 against (J) DLG-1::GFP, (K) ARP-2::GFP, (L) *plin-26::LifeAct::GFP*, and (M) CDC-42.

Figure 9. Transient co-localization of mKate2::RGA-8 on the epidermal membrane together with active CDC-42

(A) Localization of mKate2::RGA-8 was measured against localization of GFP::CDC-42 on the apical intestinal membrane. Line scan was done across apical intestinal membrane and showed that the peak of mKate2::RGA-8 and GFP::CDC-42 coincide (B) Localization of mKate2::RGA-8 was compared against localization of GBD::WSP-1::GFP on the apical intestinal membrane (C) Graph measuring apical to lateral ratio of GBD::WSP::GFP for the respective mutants (D-E) Localization of mKate2::RGA-8 was compared against localization of GBD::WSP-1::GFP in dorsal cells during dorsal intercalation. (D' and D'') Linescan was done along the membrane to depict transient enrichment of mKate2::RGA-8

at the medial tip of intercalating cells. (E') Linescan was done across the membrane to show transient enrichment of mKate2::RGA-8 on the membrane. (F) mKate2::RGA-8 maintain apical enrichment on the intestinal tissue upon *cdc-42 RNAi* treatment.

Figure 10. Defective CDC-42 pathway causes increased level of epidermal F-actin in *rga-8(pj60)*.

(A) Embryo representation to show the level of *plin-26::LifeAct::mCherry* on the migrating leading-edge epidermal cells during ventral enclosure. (B) Quantitation of *plin-26::LifeAct::mCherry* plotted for mean with 95% confidence interval. Measurement for (C) protrusion and (D) retraction rate of migrating leading-edge epidermal cells during ventral enclosure. (E) Close-up images for migrating leading-edge epidermal cells during ventral enclosure for wild type and *rga-8(pj60)* mutant. (F) Quantitation of *plin-26::LifeAct::GFP* plotted for mean with 95% confidence interval. Measurement for (G) protrusion and (H) retraction rate of migrating leading-edge epidermal cells during ventral enclosure.

Figure 11. Mutant *rga-8(pj60)* caused decreased myosin level in the epidermal pocket cells

(A) The time-lapse imaging of every 10 minutes of NMY-2/myosin II expression was shown starting from 230 minutes to 300 minutes after the first cleavage when the contralateral pocket cells meet at the ventral midline for wild type and other mutants. (B) Measurement of NMY-2/myosin II expression was done when the

contralateral pocket cells met at the ventral midline and plotted for mean with 95% confidence interval. Significance was calculated using ANOVA with Bonferroni's post-test. (C) Embryos with the double marker of NMY-2::GFP;mKate2::RGA-8 was visualized at the stage where the contralateral pocket cells meet at the ventral midline. Enlarged section of the pocket cells was shown to emphasize co-localization of NMY-2::GFP and mKate2::RGA-8.

Figure 12. Mutant *rga-8(pj60)* affects the timing of leading-edge cell migration and elongation

(A) Representative time-lapse images of embryos undergoing development were shown at their respective time for wild type and *rga-8(pj60)*. (B) Timing measurement of embryos undergoing elongation from two-fold stage to three-fold stage is plotted as mean with 95% confidence interval (n>30 for every genotype). (C) Timing measurement for embryos undergoing ventral enclosure, measured from the start of first protrusion in leading-edge cells to the final meeting at the ventral midline. Values were plotted as mean with 95% confidence interval.

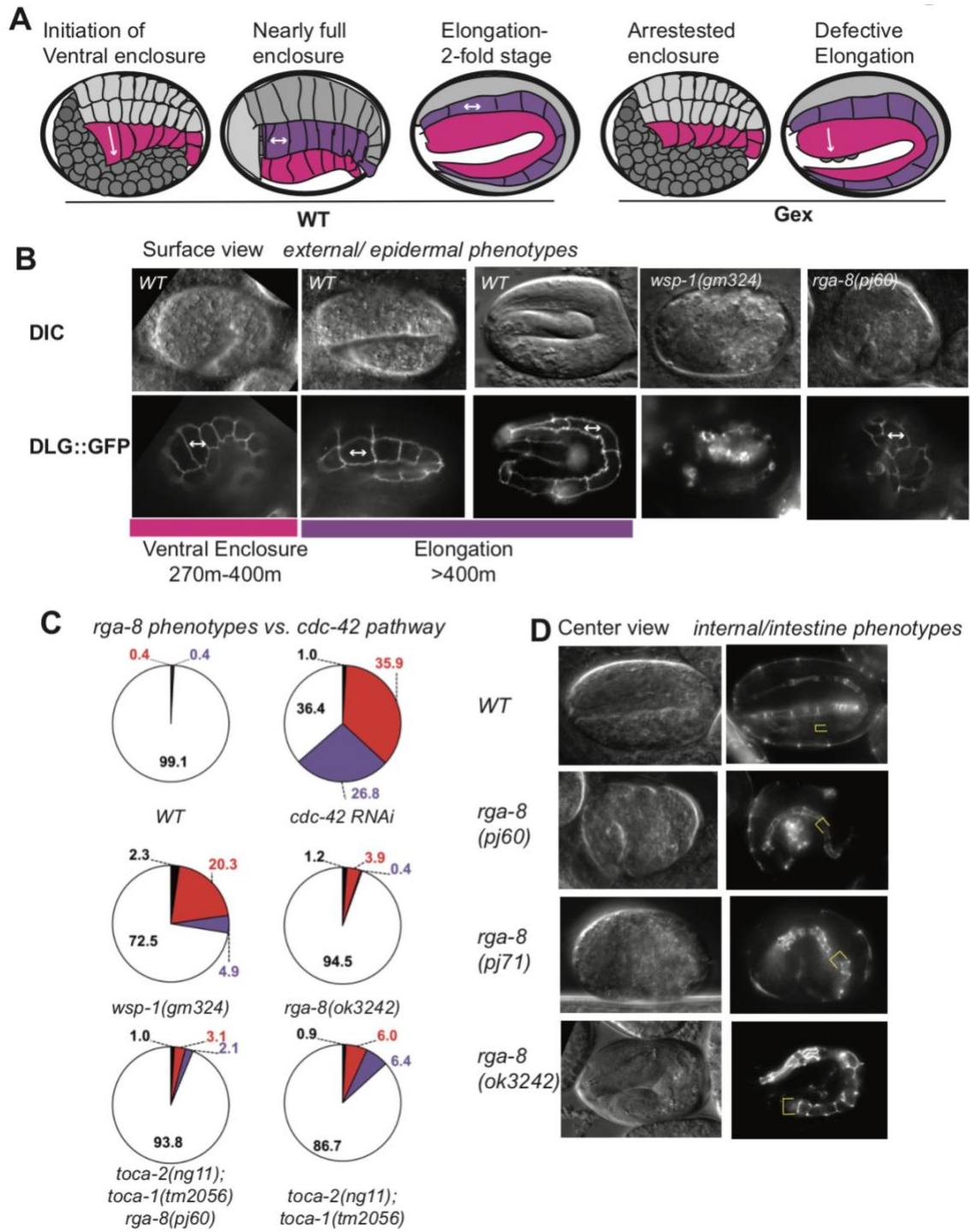


Figure 6 CDC-42 controls morphogenesis in *C. elegans*.

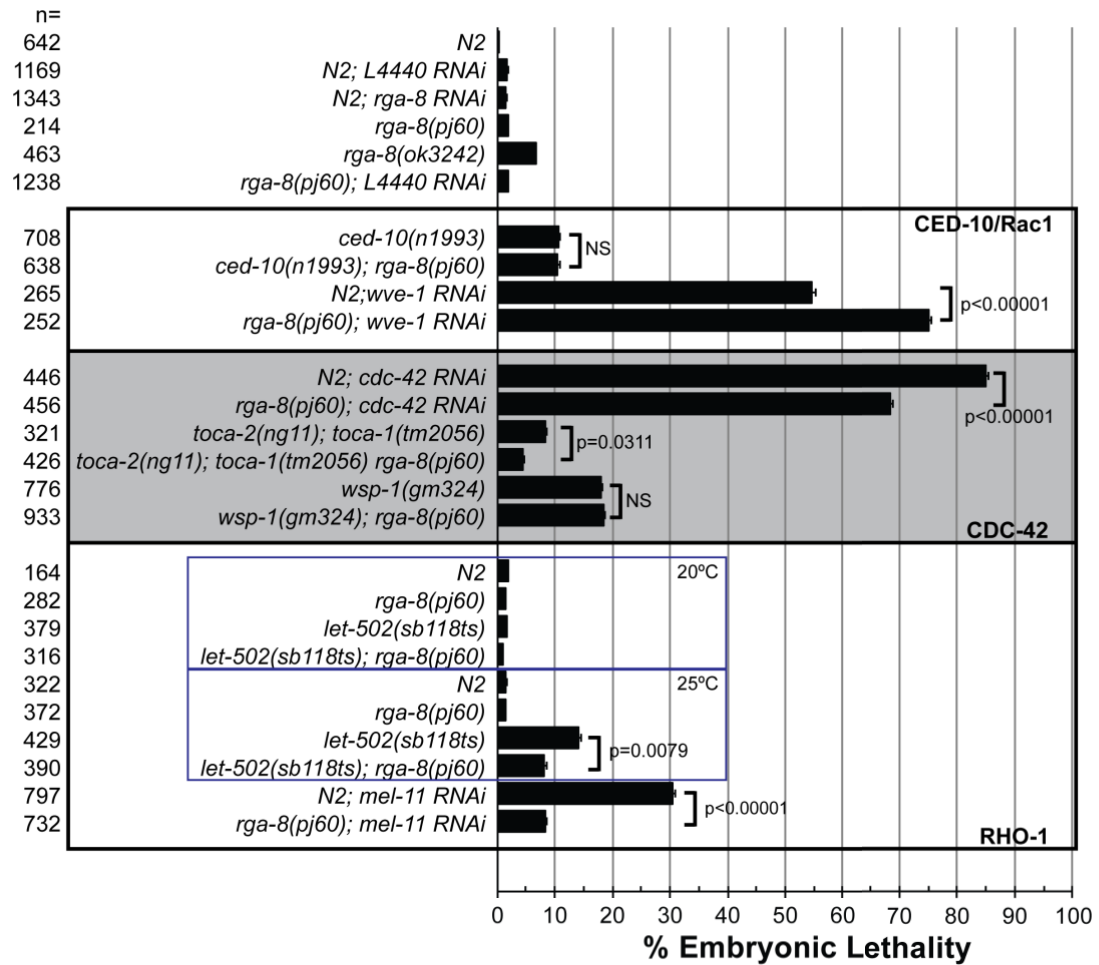


Figure 7 RGA-8, a GTPase activating protein (GAP), regulates CDC-42 and RHO-1, but not CED-10/Rac1

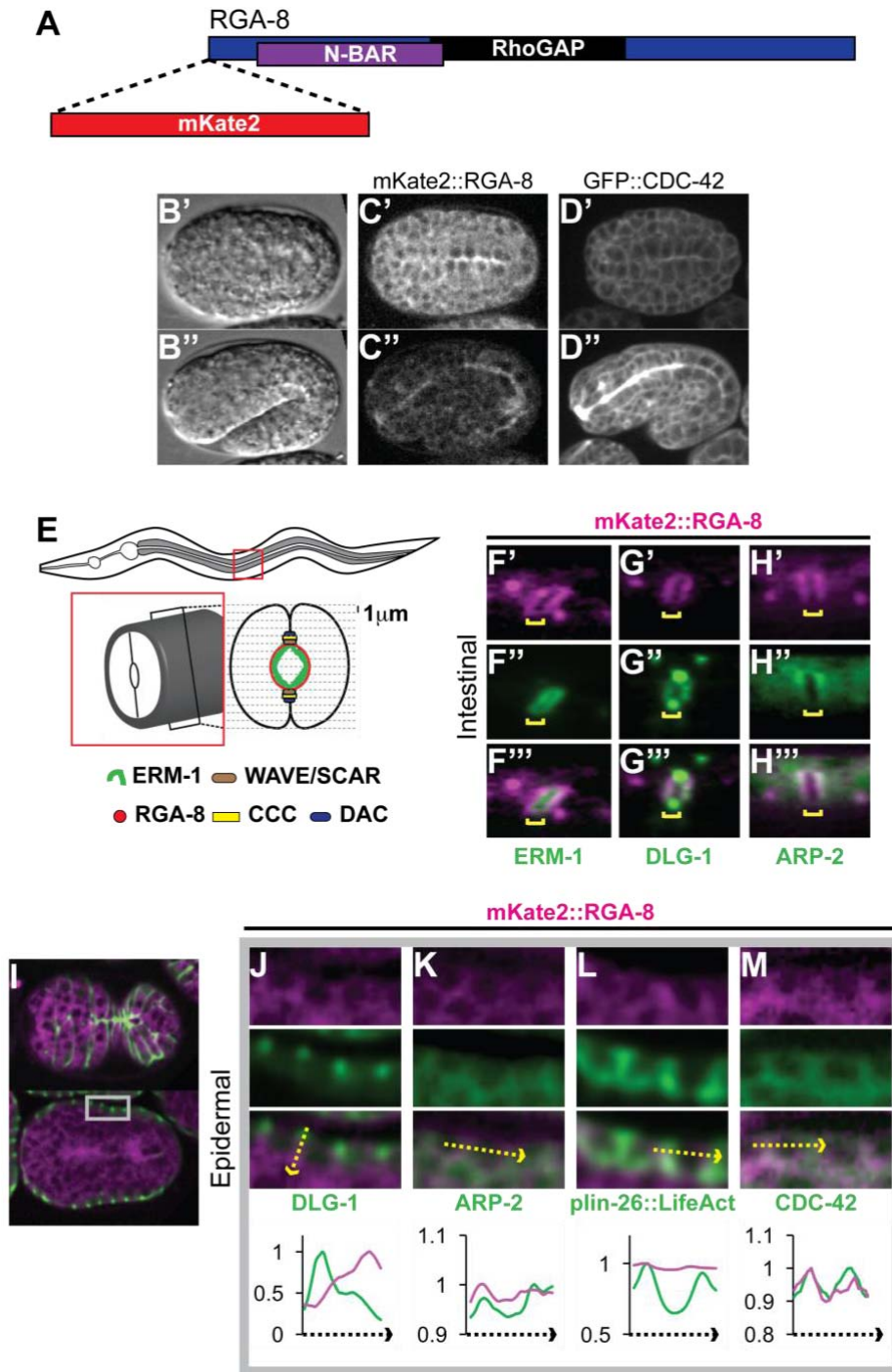


Figure 8 RGA-8 is enriched on the membrane in the epidermis and apically-enriched in the intestine.

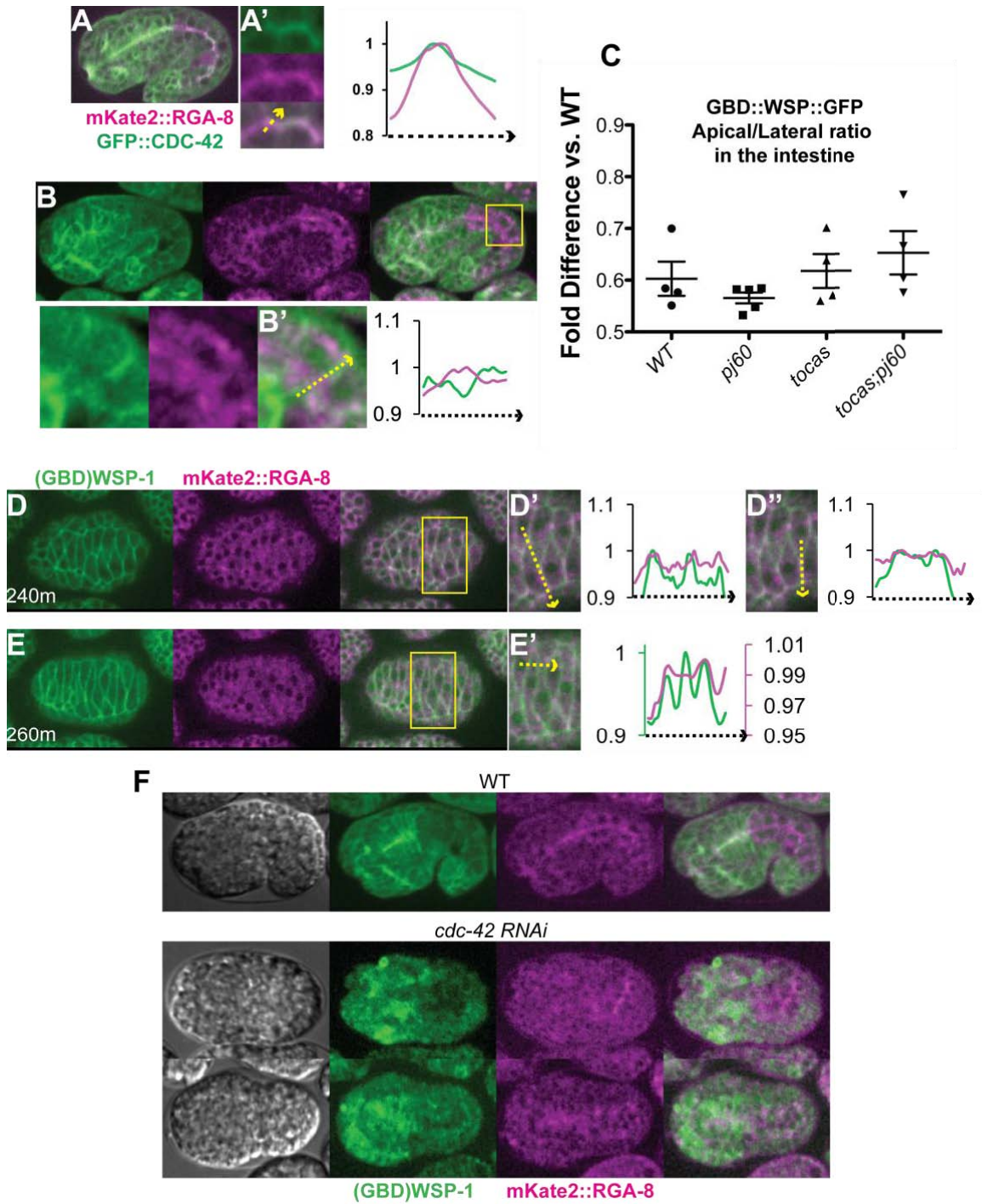


Figure 9 Transient co-localization of mKate2::RGA-8 on the epidermal membrane together with active CDC-42

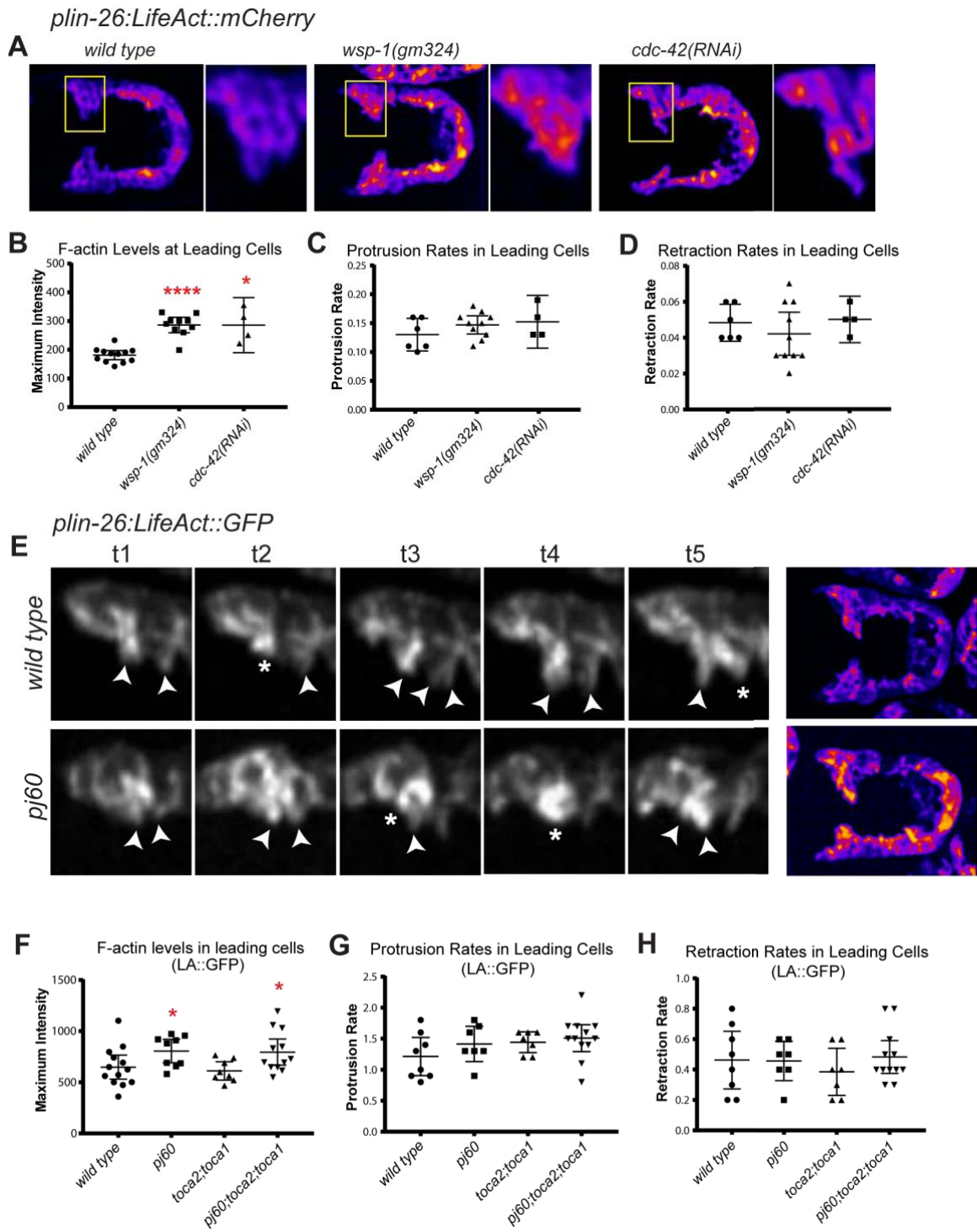


Figure 10 Defective CDC-42 pathway causes increased level of epidermal F-actin in *rga-8(pj60)*.

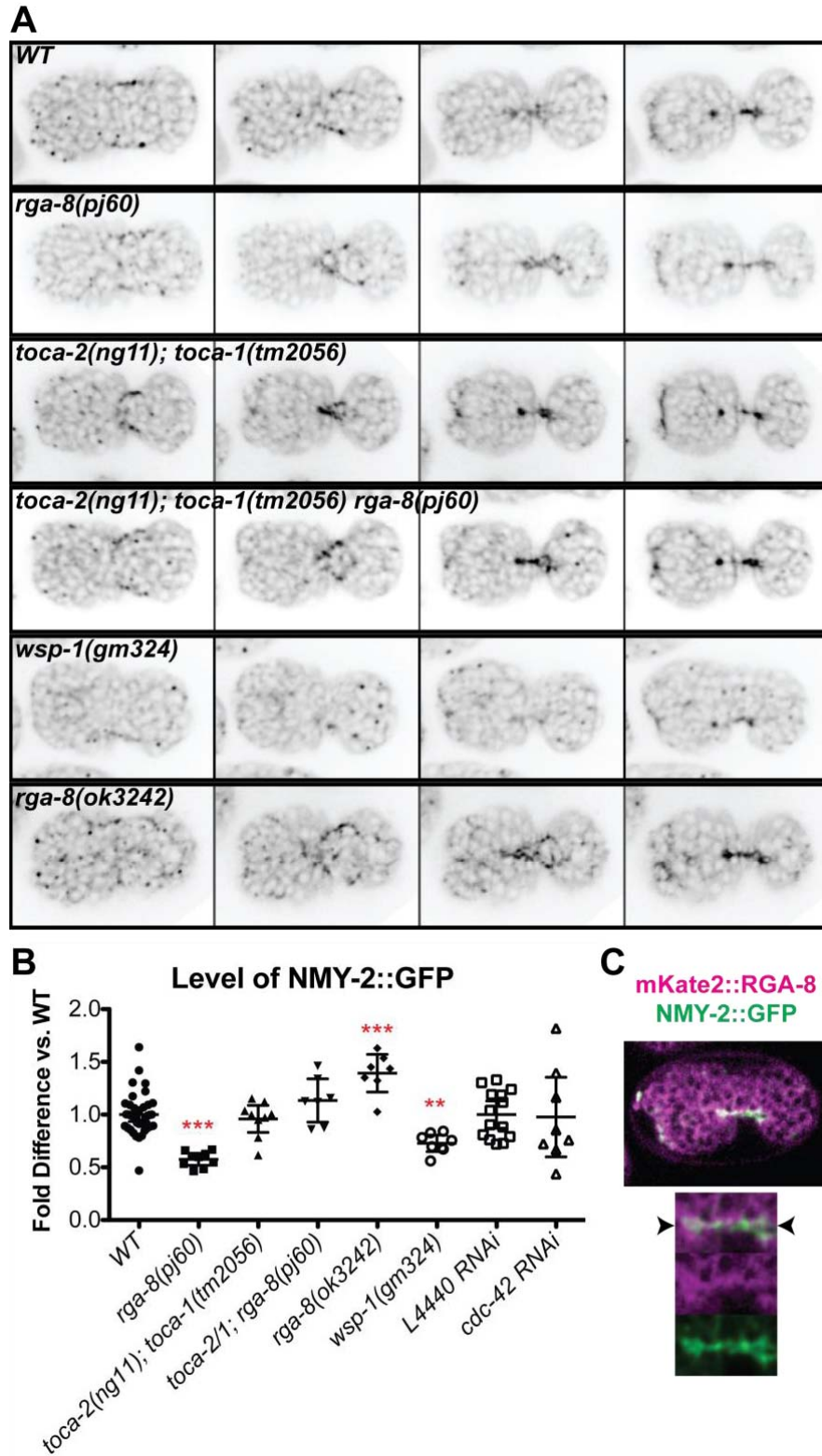


Figure 11 Mutant *rga-8(pj60)* caused decreased myosin level in the epidermal pocket cells

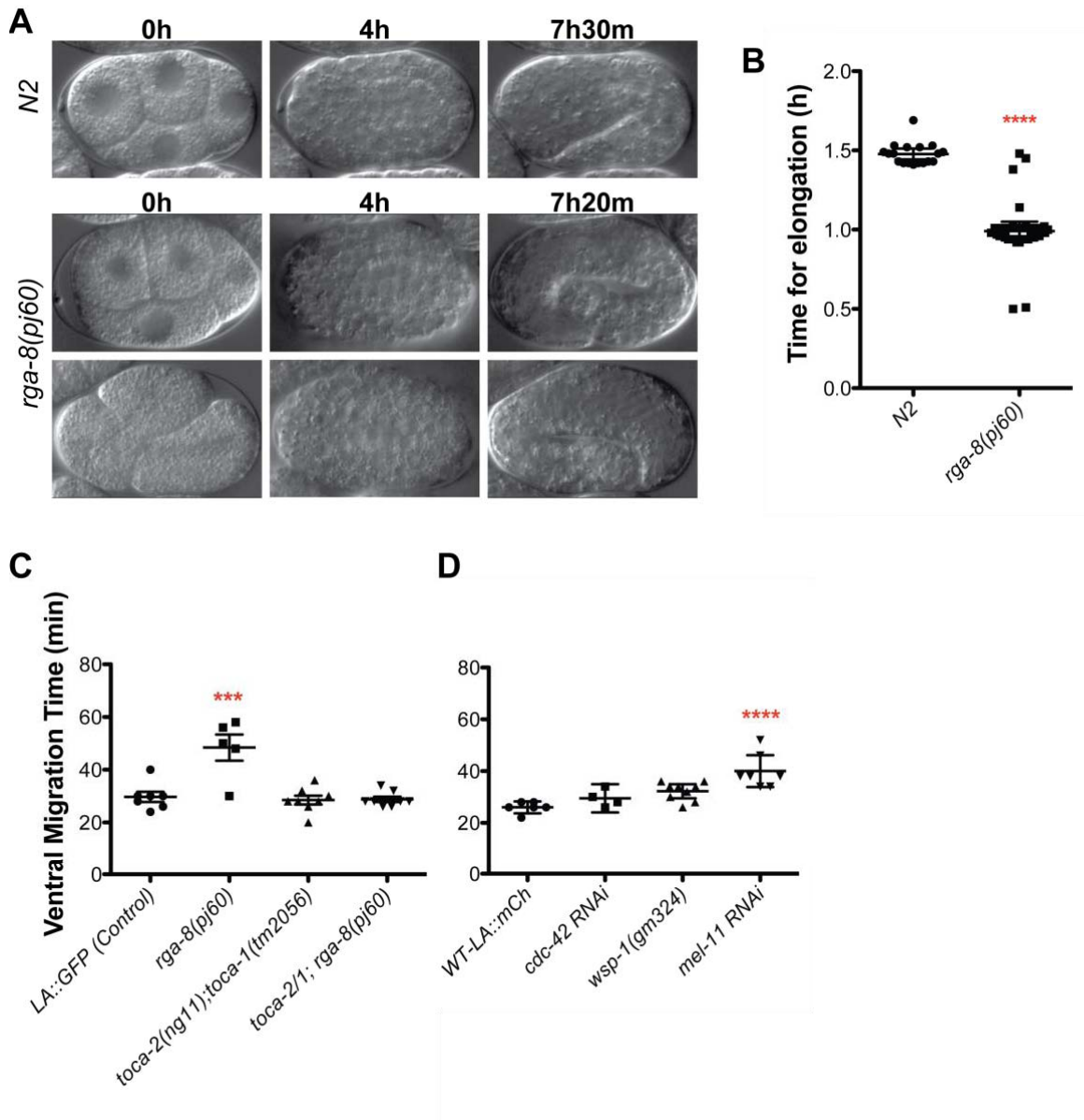


Figure 12 Mutant *rga-8(pj60)* affects the timing of leading-edge cell migration and elongation

**CHAPTER 3: The RhoGAP myosin 9/HUM-7
integrates signals to modulate RhoA/RHO-1
during embryonic morphogenesis in
*Caenorhabditis elegans***

As published:

A. G. Wallace, **H. Raduwan**, J. Carlet, M. C. Soto, The RhoGAP myosin 9/HUM-7 integrates signals to modulate RhoA/RHO-1 during embryonic morphogenesis in *C. elegans*. *Development*, (2018).

Results in Figure 13, Figure 14, Figure 15, Figure 16 and Figure 18A were contributed by AGW. JCM is an undergraduate student assisting AGW.

Results in Figure 17, and the rest of Figure 18 were contributed by HR.

Abstract

During embryonic morphogenesis, cells and tissues undergo dramatic movements under the control of F-actin regulators. Our studies of epidermal cell migrations in developing *C. elegans* embryos have identified multiple plasma membrane signals that regulate the Rac1 GTPase, thus regulating WAVE and Arp2/3 complexes, to promote branched F-actin formation and polarized enrichment. We describe here a pathway that acts in parallel to Rac1 to transduce membrane signals to control epidermal F-actin through the GTPase RHO-1/RhoA. RHO-1 had been shown to contribute to epidermal migrations through effects on underlying neuroblasts. We identify signals to regulate RHO-1-dependent events in the epidermis. HUM-7, the *C. elegans* homolog of human Myo9A and Myo9B, regulates F-actin dynamics during epidermal migrations. Genetics and biochemistry support that HUM-7 behaves as GAP for the RHO-1/RhoA and CDC-42 GTPases. Loss of HUM-7 enhances RHO-1-dependent epidermal cell behaviors. We identify SAX-3/ROBO as an upstream signal that contributes to attenuated RHO-1 activation through its regulation of HUM-7/Myo9. These studies identify a new role for RHO-1 during epidermal cell migrations, and suggest that RHO-1 activity is regulated by SAX-3/ROBO acting on the RhoGAP HUM-7.

Introduction

Cell migration is a highly regulated process that encompasses many biological phenomena, such as immune response, wound healing, cancer progression, tissue development, and neuron signaling. Cell migration is regulated by the cytoskeletal network inside the cells that consists of actin, tubulin, and intermediate filament. The cytoskeletal network is in turn regulated by the GTPase of the RHO family, a molecular switch that is active when bound to GTP and inactive when bound to GDP. Study of cell migration had been done on many tissues, and many players were found to contribute to the regulation of cell migration, yet there are still many open questions remain to be solved. In this chapter, we tried to address the questions of how RhoA/RHO-1 signaling is regulated during cell migration, using the *Caenorhabditis elegans*' embryonic development as a system.

C. elegans epidermal morphogenesis during embryonic development served as a great model system to study collective cell migration. Epidermal morphogenesis begins right when epidermal cells have fully differentiated at the dorsal and posterior end of the embryo. The two rows of dorsal cells interdigitate to form one row of the dorsal cell, in a process called dorsal intercalation (1, 6). The ventral-most cells at both the left and the right end of the embryo migrate to meet at the ventral midline, in a process termed ventral enclosure (1, 5). Failure for ventral epidermal cells to migrate towards the ventral midline caused the internal organs, such as the pharynx and intestine, to be pushed out, a phenotype

called gut on the exterior, Gex (38). Finally, the enclosed embryos undergo elongation resulting in a two-fold decrease in diameter and a four-fold increase in length to form the vermiform shape larvae (3, 4).

Ventral enclosure and dorsal intercalation have been shown to be regulated by actin cytoskeleton (3, 5). Further, previous work in the lab, as well as others, implicating the importance of a member for the RHO family GTPases, Rac1/CED-10 during *C. elegans* ventral enclosure (38, 39). Rac1/CED-10 was shown to regulate branched actin formation through WAVE/SCAR pathway in *C. elegans* during ventral enclosure (38, 39, 119). In addition, members of axonal guidance receptor families, UNC-40/Netrin, SAX-3/ROBO, and VAB-1/EphR, also regulate ventral enclosure, the null mutant of which caused variable penetrance of Gex phenotype (119). Another branched actin pathway regulated by CDC-42 GTPase has also been shown to control ventral enclosure, through WASP/WSP-1 (92, 93, 99, 100). Therefore, the two common branched actin pathways are important during ventral enclosure of *C. elegans* embryogenesis.

Elongation was shown to be primarily regulated by the actomyosin contractility (3, 4). In the vertebrate system, actomyosin contractility has been shown to be regulated by RhoA GTPase. In *C. elegans*, the non-muscle myosin 1 and 2 (NMY-1 and NMY-2) were shown to act redundantly to control elongation of *C. elegans* (44). The activity of NMY-2 has been shown to be regulated by phosphorylation and dephosphorylation of the regulatory myosin light chain (rMLC) in the vertebrate system. Phosphorylation and dephosphorylation of rMLC/MLC-4 are regulated by Rho-binding kinase (ROCK/LET-502) and myosin phosphatase

(MYPT/MEL-11), respectively. Indeed, rMLC/MLC-4 and ROCK/LET-502 have been implicated during the elongation process of *C. elegans*, mutants of which resulted in embryos that are defective during elongation. Removal of MYPT/MEL-11 caused a hypercontractility phenotype, resulting in embryos that rupture during elongation (46).

The GTPase is a molecular switch that is controlled by the state of guanine nucleotide bound to it. Hydrolysis of GTP to GDP caused the GTPase to be inactive, and this is regulated by GTPase-activating protein (GAP). Replacement of GDP with a new GTP caused the GTPase to be active, and this is regulated by guanine-exchange factor (GEF) protein. We proposed that these two families of protein might function upstream of the GTPase to relay signals from the receptor during ventral enclosure in *C. elegans*. In the screen to find the GAP involved during epidermal morphogenesis, we found a GAP, HUM-7/MyoIX to be important for regulating of RhoA/Rho-1 activity during epidermal morphogenesis.

The RhoGAP Myo9/Myosin IX is proposed to regulate multiple cellular functions including adhesion, cell migration, and immune function. Mammals have only two of these myosins, Myo9a, and Myo9b (Reviewed in (120)). Loss-of-function mutations or overexpression of these proteins has been linked to various cancers and immune defects. Some studies support a role for Myo9b in human intestinal diseases like inflammatory bowel disease and Crohn's disease (64-66). The complex structure of Myo9 proteins includes a C-terminal GAP domain that studies show attenuates RhoA activity. Myo9 proteins also have an N-terminal single headed processive myosin motor that moves the protein towards the plus,

or barbed, ends of F-actin fibers (56-61). Conserved RA (Ras associated) and C1 domains are less understood. The mouse knock out of Myo9a resulted in CNS and kidney defects (62, 63) that may involve changes in protein trafficking, while the mouse Myo9b knockout resulted in altered morphology and motility of immune cells (57) and impaired intestinal barrier function (58). A pathway has been proposed in a human lung cancer model where SLIT/ROBO acts to inhibit Myo9b, which releases RhoA. However, the reason why this double inhibitory pathway is needed to regulate RhoA, and how misregulated RhoA promotes lung cancer is unclear (121). In metastatic prostate cancer cell lines, Myo9b is elevated, while knockdown of Myo9b results in altered NMY2A (non-muscle myosin), and defective migrations, further supporting a function in RhoA attenuation (122). *C. elegans* has a single Myo9 homolog, HUM-7, which has been characterized extensively at the biochemical level. It was shown that this single-headed myosin motor is able to move processively towards the plus end of actin fibers (60). However, the *in vivo* role of HUM-7 has not been reported.

We sought novel regulators of morphogenesis and identified the Myo9/Myosin IX/HUM-7 protein. In this study, we characterize the contribution of Myo9/HUM-7 to *C. elegans* morphogenesis. We investigate which GTPases are affected by this RhoGAP, and place *hum-7* in a genetic pathway known to regulate actomyosin contractility. Additionally, we address how *hum-7* affects F-actin levels, polarization and dynamics, and how it compares to known RHO-1/RhoA pathway mutants, including *mel-11*. We also investigate the contribution of Myo IX/HUM-7 to axonal guidance. Genetic epistasis studies place this GAP

downstream of two receptors, SAX-3/ROBO and VAB-1/EphB, which are known to regulate F-actin during morphogenesis, and to modulate RHO-1 signaling.

Results

Three axonal guidance receptors are upstream regulators of F-actin during morphogenesis through their effects on WAVE/SCAR (Figure 13A) (123). To identify proteins that might connect the axonal guidance receptors to WAVE/SCAR regulation, we performed an RNAi screen to identify genes that enhance the low levels of embryonic lethality (14%) caused by loss of one of the axonal guidance receptors, UNC-40. We screened through a 2000-clone feeding RNAi library (124) which represents about 10% of all *C. elegans* genes and identified several enhancers of *unc-40* lethality using the putative null allele *unc-40(n324)*. RNAi depletion of HUM-7, an unconventional myosin heavy chain protein, increased *unc-40* embryonic lethality due to Gex-like failures in morphogenesis to 26%. *hum-7* was thus a candidate gene to act in parallel to *unc-40* during morphogenesis.

HUM-7 functions in post-embryonic axonal guidance and genetically interacts with WAVE/SCAR axonal guidance regulators in embryos and larvae.

To test if *hum-7* affects other signals that regulate the WAVE-1 complex, we fed *hum-7 RNAi* to animals missing other axonal guidance receptors. While loss of HUM-7 significantly increased the embryonic lethality caused by loss of UNC-40, it had no significant effect on the embryonic lethality due to *vab-1(dx31)* null mutation, and it suppressed the embryonic lethality caused by the *sax-3(ky123)* null mutation from 44% to 29% (Figure 13B). Therefore, loss of *hum-7*

had distinct effects on the three upstream signals that organize the cytoskeleton in developing embryos.

One human homolog of HUM-7, Myo9A, is mutated in patients with defects in the neuromuscular junction, leading to myasthenic syndrome (125). To test for HUM-7 post-embryonic roles, particularly in neurons, we characterized the loss of HUM-7 on six mechanosensory neurons, including the AVM neuron, that are easily visualized using the neuronal transgene *mec-4::gfp* (126). In a wild type background, the AVM neuron has a single round cell body and sends out one axonal projection that travels ventrally to the nerve cord and then anteriorly (Figure 13C). RNAi depletion of HUM-7 in the *mec-4::gfp* transgenic strain caused statistically significant increased AVM ventral migration defects.

To determine if *hum-7* and the axonal guidance receptor mutants interact genetically during postembryonic development, we analyzed the effects of *hum-7* RNAi on strains containing null alleles of the axonal guidance mutants and the *mec-4::gfp* transgene. The ventral migration defects caused by *unc-40(n324)* were enhanced from 50% to 62% by *hum-7* RNAi. In contrast, *sax-3(ky123)* ventral migration defects were suppressed from 51% to 39% by *hum-7* RNAi. There were no significant differences in ventral migration defects in *vab-1(dx31)* mutants fed *hum-7* RNAi (Figure 13C,D). Therefore, the post-embryonic genetic interactions paralleled the embryonic genetic interactions, suggesting a conserved function for HUM-7 throughout development.

HUM-7 functions in embryonic morphogenesis.

If HUM-7 is an important regulator of morphogenesis, it should have a phenotype on its own. Depleting *hum-7* via RNAi in a wild type (N2) background resulted in 6.5% embryonic lethality. The *hum-7(ok3054)* mutation generated by the *C. elegans* Knockout Consortium is a 653 bp deletion spanning the 3' end of the myosin domain and two IQ domains (binding sites for EF-hand proteins including regulatory myosin light chains and calmodulin) (127) (Figure 14A). We out-crossed this strain three times, and detected 5.8% embryonic lethality. Since RNAi and the small deletion could mask the true loss of function phenotype, we generated an almost full-length deletion using CRISPR, *hum-7(pj62)*, and observed similar phenotypes and slightly higher embryonic lethality of 9.5%. Approximately half of the dead embryos displayed a phenotype known as Gex (gut on the exterior), which occurs 100% of the time when any gene in the WAVE complex is removed. In Gex embryos, epidermal ventral migration fails, resulting in exposed internal organs like the pharynx and intestine, and the embryo dies (128). Other dead embryos displayed 2-fold arrest, indicating a defect at the next morphogenesis step, elongation. All of these *hum-7* phenotypes were observed in both *hum-7* deletion mutants and in *hum-7 RNAi* embryos, in similar percentages (Figure 14A-D Table 6). This is similar to putative null mutations in upstream regulators of F-actin, like *unc-40*, which are only 14% embryonic lethal. Therefore, loss of *hum-7* alone results in partially penetrant and strong morphogenesis phenotypes.

The *hum-7* CRISPR alleles and Consortium deletion were used to further probe *hum-7* genetic interactions with the axonal guidance genes. Testing the genetic interactions of *hum-7* using the two deletions, *ok3054* or *pj62*, gave similar results in combination with null mutations in *unc-40* (increased lethality), *sax-3* (suppressed lethality) or *vab-1* (no change) as we saw with *hum-7* RNAi (Figure 14C). This suggests RNAi causes strong loss of *hum-7* function. We used CRISPR to generate a point mutation in the GAP of *hum-7*, *pj63*, and found different effects. This Arginine to Alanine (R to A) mutation, predicted to perturb the GTPase activating function of RhoGAPs, resulted in increased lethality compared to the deletions (30%), and more than additive lethality in combination with *unc-40* and *vab-1*. Unlike deletion alleles, the *pj63* GAP mutant could not rescue *sax-3* embryonic lethality (Figure 14C). This result further supports an interaction between *hum-7* and *sax-3* and suggests SAX-3 may regulate HUM-7 activity.

HUM-7 functions as a GAP for RHO-1 and CDC-42, but not for CED-10/Rac1.

HUM-7 has strong sequence homology with myosin IX/Myo9 proteins from a variety of organisms and includes the typical N-terminal myosin and C-terminal RhoGAP domains (56, 57, 61, 62). HUM-7 has greater than 30% overall protein identity with human Myo9a and Myo9b (Figure 13E). While a *C. elegans* GAP that regulates the GTPase CED-10 during cell corpse engulfment has been identified (129, 130), this GAP, SRGP-1, is dispensable for embryonic viability, and has

limited morphogenesis phenotypes (131). We therefore tested if HUM-7 functions as a GAP for one or more *C. elegans* GTPases.

Genetic tests of GAP function: We hypothesized that if HUM-7 acts like a GAP for CED-10/Rac1, then loss of *hum-7* would rescue partial loss of CED-10/Rac1. However, while the *ced-10(n1993)* hypomorphic mutation resulted in 14% embryonic lethality, depletion of *hum-7* via RNAi in *ced-10(n1993)* increased embryonic lethality to 34% (Table 6, Figure 14D). An increase was seen with a second hypomorphic allele, *ced-10(n3246)* (Table 6). Thus *hum-7* and *ced-10* appear to function in parallel pathways.

To test if HUM-7 can function as a GAP for RHO-1/RhoA, we used a temperature sensitive allele of the known RhoGEF, *ect-2(ax751)*. This allele has been well characterized to partially knock down RHO-1 signaling (132). At 23°C, *ect-2(ax751)* resulted in 61% embryonic lethality on control RNAi, that dropped to 43% lethality in animals also depleted of *hum-7* via RNAi. Similarly, *ect-2 RNAi* leads to almost 100% dead embryos, but this drops to 84% dead embryos if *ect-2 RNAi* is fed to *hum-7* mutants (Figure 14D, Table 6). Further, all of the *ect-2* phenotypes, including poor differentiation that suggests *ect-2* defects in the early embryo, were suppressed by the loss of *hum-7* (Table 7).

To test if HUM-7 can function as a GAP for CDC-42, we used RNAi depletion of *cdc-42*, which in wild type animals resulted in embryonic lethality above 60%. In contrast, depletion of *cdc-42* via RNAi in the putative null strain *hum-7(ok3054)* resulted in embryonic lethality of only 27% (Table 6, Figure 14D).

The fact that loss of *hum-7* was able to suppress embryonic defects caused by partial loss of *cdc-42* or *rho-1* (using *ect-2(ax751)*) suggested *hum-7* acts in a pathway with *rho-1* and *cdc-42*. Since there are no other reports of a Myosin IX protein regulating *cdc-42*, we also tested if loss of *hum-7* could suppress the lethality of a known *cdc-42* effector, *wsp-1*. Deletion mutant *wsp-1(gm324)* results in 18.4% embryonic lethality that drops to 11.4% when these animals are depleted of *hum-7* via RNAi (Table 6).

Molecular tests of GAP function: To test if the HUM-7 GAP domain can bind to the activated form of specific GTPases we performed GST pull-down assays. Purified His-tagged GTPases in active (GTP-loaded) and inactive (GDP-loaded) form were individually tested for binding to the GAP domain of HUM-7. The GAP domain of HUM-7 bound strongly to GTP-loaded RHO-1 and CDC-42 and failed to bind GTP-loaded CED-10. No binding was observed between HUM-7 GAP and any of the GDP-loaded constructs tested for all three GTPases (Figure 14E). In short, HUM-7 behaves functionally, as well as molecularly, as a GAP for RHO-1 and CDC-42, but not CED-10.

HUM-7 is expressed in muscles.

If HUM-7 is important for embryonic development, we expect it to be expressed in embryos. We therefore created an N-terminus endogenously tagged allele of *hum-7*, *pj72*, via CRISPR. CRISPR tagged *gfp::hum-7* is faintly expressed in embryonic muscle, including the developing body wall muscles and pharynx (Figure 15A). Expression in other embryonic tissues, like neuroblasts and

epidermis, could not be determined with the CRISPR allele. Staining *gfp::hum-7* adults with monoclonal antibody 5.6 (133) which recognizes body wall muscles, confirmed the muscle enrichment (Figure 15B, enlarged boxed region).

The *gfp::hum-7* CRISPR strain was crossed to other strains to analyze expression in other tissues in larvae and adults. A strain carrying *gfp::hum-7* and *hmr-1::mKate2* (134) allowed us to compare expression in the central nervous system, pharynx and epidermis (Figure 15C). In the posterior pharyngeal bulb *gfp::hum-7* is expressed throughout, including the pm6 and pm7 cells that help the grinder contract during feeding (Worm Atlas), while *hmr-1::mKate2* is enriched only in apical regions, as expected. *hmr-1::mKate2* is expressed all through the nerve ring axons, while *gfp::hum-7* is expressed in adjacent cells, perhaps glia. Viewing this same strain on the surface shows that while *hmr-1::mKate2* is highly expressed in the seam cells, *gfp::hum-7* shows no obvious overlap in the seam cells (Figure 15C). A strain expressing RFP under control of the myosin heavy chain promoter, *Pmyo-3::rfp* (135), shares expression with *gfp::hum-7* in body wall muscles (Figure 15A). Therefore *gfp::hum-7* appears to have broad expression, with enrichment in several types of muscle tissue including regions of the pharynx, and in body wall muscles. Expression is not overall enhanced in neurons, but may include support cells for neurons. Expression does not appear enhanced in epidermal cells, although there is precedent for epidermal signal to appear striped due to impingement from muscle or pharynx (Worm Atlas). Antibody staining with antibodies specific to body wall muscle support that at least some of the striped signals are in muscle (Figure 15B).

***sax-3* regulates levels of *gfp::hum-7* in muscle**

hum-7 genetic interactions with the axonal guidance receptors led us to test if any of them might be upstream regulators of *gfp::hum-7*. Loss of *unc-40* or *vab-1* had limited effects on *gfp::hum-7*, but loss of *sax-3* resulted in significantly elevated levels of *gfp::hum-7* in expressing tissues. Measuring the effect on the posterior bulb, or body wall muscles, showed an increase of almost 100% (Figure 15E). The genetic and molecular interactions both suggest that *sax-3* is upstream of *hum-7* and that SAX-3 signaling, directly or indirectly, results in lower HUM-7 expression.

HUM-7 affects F-actin dynamics during the initial cell migrations required for epiboly.

Some embryonic phenotypes resulting from loss of HUM-7 resemble the Gex phenotype seen when members of the WAVE/SCAR complex are mutated (Figure 13A, Figure 14B). Loss of WAVE/SCAR components during epidermal cell migration leads to defects in F-actin levels, ventral F-actin enrichment and actin dynamics in the migrating epidermis (123, 136). We therefore tested HUM-7 effects on the actin cytoskeleton using two epidermal F-actin transgenic strains, *plin-26::vab-10 ABD (actin binding domain)::gfp (mcls51)* (137) and *plin26::Lifeact::mCherry* (138). These strains, which express an actin binding protein (*vab-10* ABD or Lifeact) under the *lin-26* epidermal promoter, enabled us to perform live imaging of actin levels, ventral enrichment and dynamics in the epidermis of embryos during morphogenesis. In wild-type embryos, early in

morphogenesis (250 minutes after the first cell division), F-actin becomes enriched at the ventral edge of the leading cells of the epidermis. When WAVE components are depleted via genetic mutation or RNAi overall F-actin levels drop (136). In *hum-7* mutants or *hum-7(RNAi)* embryos the overall levels of F-actin are higher than in wild type using the *plin-26::vab-10 ABD strain*, or *plin26::Lifeact::mCherry* strain (Figure 16A-E). We conclude that loss of *hum-7* increases epidermal F-actin levels. Since HUM-7 is not enriched in epidermis, these effects may be indirect.

In WAVE mutants, F-actin fails to enrich ventrally in the migrating cells and therefore fails to drive ventral enclosure (123, 136). However, in *hum-7* mutants, F-actin is correctly enriched ventrally in the leading cells (Figure 16C). Therefore, *hum-7* does not appear to regulate ventral enrichment.

We next compared actin dynamics in *hum-7* mutants, using F-actin reporters. Previous work using the *plin-26::vab-10 ABD* transgene showed that wild type ventral epidermal cells undergo frequent protrusions and retractions at the edge of the leading cells, while protrusions and retractions in WAVE/SCAR mutants occurred less frequently (123, 136). To assess the effects of *hum-7* on actin protrusion dynamics, we imaged F-actin using *plin26::Lifeact::mCherry*, every two minutes from 240 minutes to 400 minutes after first cleavage. Wild-type embryos exhibited dynamic protrusions at the edge of the leading cells, averaging 1.0 protrusion from five time points sampled during 8 minutes of enclosure. *hum-7* mutants averaged 1.6 protrusions per time point (Figure 16F,G, S1 Movie, S2 Movie (12)). Similar results were seen in movies made at 15 second intervals during the first 5 minutes of enclosure, which showed an increase from 1.1 to 1.6

protrusions per time point (Figure 16F,G). Therefore, the rate of protrusion formation is greater in *hum-7* mutants than in wild type, the opposite of the defect seen in WAVE mutants.

F-actin enrichment and dynamics were affected in *sax-3* mutants, and this depended, at least partially, on *hum-7*. Previous work using *plin-26::vab-10 ABD* showed that *sax-3(ky123)* embryos have relatively wild type levels of F-actin at the beginning of ventral enclosure, that becomes more disrupted as enclosure proceeds. The enclosure process was also delayed (123). *sax-3(ky123)* crossed into *plin26::Lifeact::mCherry* resulted in elevated F-actin during enclosure, while the double mutant with *hum-7* resulted in lower levels (Figure 16D,E). Average protrusions in the leading cells during enclosure were elevated in *sax-3* mutants, and this number also dropped in the double with *hum-7* (Figure 16F,G, from 2.2 to 1.6). Movies made at 15 second intervals showed the same pattern of average protrusions during enclosure, with elevated protrusions in *hum-7* and *sax-3* single mutants, and closer to wild type in the double (1.1 in controls, to 1.6 and 1.4 in *hum-7* and *sax-3* single mutants, respectively, and 1.2 in the double). The retraction rate in the 2 minute and 15s movies showed no significant change in *hum-7* or *sax-3* single mutants, or in double mutants (Figure 16H). Therefore, the increased F-actin levels seen in the single mutants correlate with increase numbers of protrusions at the leading edge, while the drop in F-actin in the double mutants correlates with protrusions and retractions closer to wild type.

HUM-7 regulates timing of epidermal morphogenesis.

Mutations in WAVE/SCAR, or its upstream regulators, including UNC-40/DCC/Netrin Receptor, SAX-3/Robo Receptor and VAB-1/Ephrin Receptor, lead to delayed migrations (123). We compared the timing of enclosure in *hum-7* mutants and found that while a low percent of embryos arrest partway through enclosure, embryos on average are not delayed, and some can enclose faster than wild type. For example, in one set of experiments 1/7 embryos arrested, while 2/7 embryos enclosed significantly faster than wild type. In Movies S1 and S2 (12) the *hum-7(ok3054)* embryo in the center achieves ventral enclosure faster than wild type while the *hum-7(ok3054)* embryo on the right arrests during enclosure. We saw similar results in the other *hum-7* mutants, (*pj62*, 20% faster and *pj63*, 10% faster), when compared to wild type embryos and timed from 240 minutes after first cleavage to ventral enclosure, by 300 minutes. Together, these results demonstrate a role for HUM-7 in the regulation of F-actin dynamics that contribute to the correct initiation of epidermal cell migrations during epidermal enclosure, and correct timing of morphogenetic events.

HUM-7 functions as a GAP upstream of RHO-1 to regulate embryonic morphogenesis.

The role of the GTPases RhoA/RHO-1 and Cdc42/CDC-42 in the ventral enclosure step of morphogenesis is only beginning to be described (139). In contrast, the role of RHO-1 in a later morphogenetic step, epidermal elongation, is exceedingly well studied (137, 140-143). Since *hum-7* behaved genetically and

molecularly like a candidate GAP for RHO-1 (and CDC-42), we investigated if *hum-7* mutants have defects in RHO-1-dependent processes, like elongation. As shown in Figure 14B, half of dying *hum-7* embryos show defects in elongation, including swelling of the anterior region. This defect is shown by known RHO-1 pathway mutants, including *rga-2*, a RHO-1 GAP that acts during elongation but not during ventral enclosure (140) (thin arrows, Figure 14B, Table 6).

If *hum-7* is a GAP for RHO-1, loss of HUM-7 might suppress mutations that decrease Rho-dependent contractility, like *let-502*/RHO-1 Kinase, and enhance mutations that increase Rho-dependent contractility, like *mel-11*/Myosin Phosphatase. These genetic interactions have been demonstrated for the RHO GAP *rga-2* (140). The *let-502 ts* allele, *sb118ts*, resulted in 75% or 98% lethality at 25°C or 25.5°C, respectively. However this lethality dropped to 60% or 72%, respectively, when we crossed in *hum-7(ok3054)* (Figure 17A, Table 6). In a wild-type background, *mel-11* RNAi resulted in 36% lethality, which was enhanced to 60% in a *hum-7* background (Table 6, Figure 17A). Interestingly, our initial RNAi screen for enhancers of *unc-40* embryonic lethality identified both *hum-7* and *mel-11*. These results support that *hum-7* may be a GAP for RHO-1.

The effects of RhoA signaling on cell migration might occur through the activation of actomyosin contractility controlled by non-muscle myosin, NMY-2 in the epidermis. Crossing *nmy-2::gfp* with *Plin-26::Lifeact::mCherry* to visualize the epidermis revealed *nmy-2::gfp* puncta in the epidermal focal plane (Figure 17), as previously shown (144). During ventral enclosure, myosin puncta are enriched towards the leading edge of migrating cells, and at the midline as the cells meet

(Figure 17A,B). We depleted *hum-7* via mutation or RNAi, and found brighter *nmy-2::gfp* puncta in all tissues of the embryo. To measure effects on ventral enclosure, we measured the robust *nmy-2::gfp* epidermal signal as the pocket cells met at the midline. Plotting the maximum intensity showed an increase of 20% in *hum-7* mutants relative to controls (Figure 18C).

We tested how two proposed upstream regulators of *hum-7* affected *nmy-2::gfp* levels during ventral pocket cell meeting. A null mutation in *sax-3, ky123*, led to a 20% decrease in the pocket cell signal while a null mutation in *vab-1, dx31*, led to 20% increase (Figure 18B,C). These results suggest both SAX-3 and VAB-1 regulate actomyosin contractility in the migrating epidermal cells. To test if *hum-7* is required for these changes we removed *hum-7* via RNAi in each strain. In the *vab-1(dx31); hum-7* RNAi strain the myosin levels are somewhere in the middle, closer to wild type, which suggests the effects of VAB-1 on HUM-7 may be indirect. In contrast, the levels of *nmy-2::gfp* in the *sax-3(ky123); hum-7(RNAi)* strain resembled the levels of *hum-7(RNAi)* (elevated) further supporting that SAX-3 acts through HUM-7.

Discussion

HUM-7, a new component in the RHO-1 pathway that appears to attenuate RHO-1 signaling

The analysis of Rho GAPs has been complicated by their sheer number. Even in *C. elegans*, which has fewer GAPs than mammals, there are 23 proteins with GAP domains to regulate the low number of small Rho GTPases. Our analysis of one of these 23 GAP proteins has revealed exciting connections between axonal guidance receptors, the known players in RHO-1 signaling, and the movements of the epidermis during ventral enclosure. Our findings support a requirement for RHO-1 and CDC-42 attenuation by the previously uncharacterized RhoGAP, HUM-7/Myosin 9. *hum-7* mutants have low penetrance ventral enclosure defects, coupled with highly penetrant increased actin dynamics, suggesting that increased actin dynamics in epidermal protrusions interferes with the normal processes that accompany cellular migration. In single cell migration systems down regulation of actomyosin contractility is required to allow persistent migration in one direction (145). A similar event may be occurring in the migration of single axons, as we show here (Figure 13) that loss of HUM-7 alters neuronal migrations. One interpretation of our results is that in a sheet migration of the embryonic epidermis, increased actomyosin contractility interferes with persistent migration. Evidence in several systems suggests increased F-actin structures of one type can interfere with F-actin structures of another type (Reviewed in (146)). Since HUM-7 is a candidate GAP for both RHO-1 and CDC-42, loss of HUM-7 may lead to

increased formin assembly that would decrease G-actin available for branched actin assembly by Arp2/3. Our movies of *hum-7* mutants show higher F-actin formation and increased myosin, but they do not distinguish which form of F-actin is forming (linear or branched). Therefore HUM-7 may have a role attenuating activity levels of RHO-1 and CDC-42 so that RAC-1 based F-actin structures form correctly.

Axonal guidance receptors regulate the RHO-1 pathway

Our results suggest that HUM-7 plays an important role coordinating the response to external polarity cues by modulating RHO-1 activity to permit the correct levels and dynamics of actin required for proper cellular movements. HUM-7's role in embryonic morphogenesis was discovered through a screen for enhancers of the partially penetrant morphogenesis defects caused by loss of an axonal guidance receptor, UNC-40/DCC (Figure 13). *hum-7* showed distinct genetic interactions with each of three axonal guidance pathway receptors. Particularly intriguing was the rescue of embryonic lethality for *sax-3(ky123)* null animals, from 44% to 29% when *hum-7* is removed via RNAi or genetic mutations (Figure 13B, Figure 14C). Since HUM-7 is proposed to regulate the RHO-1 pathway, we tested if the axonal guidance mutants affected embryonic non-muscle myosin, using the *nmy-2::gfp* CRISPR strain. Loss of SAX-3/ROBO alters NMY-2::GFP levels, and this is epistatic to *hum-7*, suggesting *sax-3* and *hum-7* are in a genetic pathway that regulates NMY-2. The connection between SAX-3 and HUM-7 is further supported by the fact that loss of *sax-3* results in elevated expression

of GFP::HUM-7 levels measured using a CRISPR line (Figure 15E). Our results support that SAX-3 is a positive regulator of RHO-1 signaling during the migrations of epidermal enclosure, and that SAX-3 acts, at least in part, through negative regulation of the RhoGAP HUM-7 (Figure 17E). Since loss of *hum-7* does not fully rescue loss of SAX-3, it is clear SAX-3 has other targets during ventral enclosure. While loss of *hum-7* suppressed *sax-3* phenotypes (Figure 16D-H), just as it partially suppressed *sax-3* lethality (Figure 14C), the double mutant phenotype was different from *hum-7* alone. This suggested *sax-3* has other targets besides *hum-7*, and that these targets promote F-actin in the epidermis (Figure 16D,E).

It is possible that VAB-1/EphrinB also regulates HUM-7, to regulate the RHO-1 pathway. Overall loss of *vab-1* has opposite effects as loss of *sax-3*. For example, in *vab-1* mutants levels of *nmy-2::gfp* increase while in *sax-3* mutants they decrease (Figure 17B). In support of this, loss of *vab-1* enhances loss of MEL-11, just like loss of *hum-7*, and similarly increased levels of *nmy-2::gfp*. However, the effects of VAB-1 on the RHO-1 pathway are probably not directly through HUM-7. Loss of *vab-1* did not significantly affect *gfp::hum-7* levels (Figure 15D,E).

Axonal guidance receptors regulate the RHO-1 pathway in epidermis.

During ventral enclosure, *rho-1* and *nmy-2* are clearly needed in the underlying neuroblasts (144). Analysis of the pattern of *nmy-2::gfp* in combination with transgenes only expressed in the epidermis confirms there are important *nmy-2::gfp* puncta that form during ventral enclosure (Figure 17). Our findings that these epidermal *nmy-2::gfp* puncta are altered in embryos missing the axonal

guidance receptors, SAX-3/ROBO and VAB-1/EphB, supports an important role for these proteins in guiding the epidermal migrations directly or indirectly (Figure 18). While it is accepted that SAX-3 can rescue epidermal migrations when expressed only in the epidermis or the underlying neuroblasts (147) how VAB-1 influences epidermal migrations is more controversial, since only a subset of epidermal cells are proposed to express VAB-1 (148). In this context, it is intriguing that the strongest HUM-7 expression is not in the epidermis, or neuroblasts, but in the underlying muscle cells (Figure 15). Since We have not tested where SAX-3 and HUM-7 are required for the regulation of epidermal morphogenesis. Therefore the effects of SAX-3 on HUM-7 and the effects of both on the epidermis may not be direct.

HUM-7 and RHO-1 pathway affect actin dynamics

SAX-3/ROBO regulation of HUM-7/Myo9 to regulate RHO-1/RhoA is conserved from human cells (lung cancer) to *C. elegans*. Homologs of HUM-7, Myo9A and Myo9B, are proposed to regulate cellular behaviors as GAPs that act on the RhoA GTPase. Many of the proposed phenotypes can be explained as resulting from excess RhoA signaling. What is not as clear is what are the downstream effects of this excess RhoA signaling, and what signals regulate the behavior of this unusual RhoGAP with a processive myosin motor. We used a complex tissue migration, ventral enclosure, to measure several aspects of RhoA signaling and ask how it can perturb the dynamics of the tissue migration. As the first analysis of Myosin9 function in *C. elegans*, we have uncovered many features

of morphogenesis that depend on Myo9, and have begun to place them in signaling pathways.

We describe here that axonal guidance in *C. elegans* depends on HUM-7/Myosin9, which appears to receive signals through SAX-3/ROBO, and possibly VAB-1/EphrinB. These interactions are conserved in embryos, where they regulate epidermal cell migrations. The signals, originating from the axonal guidance receptors, alter non-muscle myosin expression in the migrating epidermal cells. The pathway we uncover here, from SAX-3/ROBO to HUM-7/Myo9, to modulate RHO-1/RhoA (Figure 17E), has been proposed to function in human lung cancer tissue culture cells. The altered timing of the migrations in *hum-7* mutant embryos suggests one consequence of misregulated RhoA in the absence of this RhoGAP is overactive RhoA that leads to excess protrusions at the leading edge, without a matching increase in retractions. This change may create various problems. It is possible the protrusions are too stable, due to decreased turnover of RhoA-GTPase. While this may lead to occasional faster migrations, it may also make the cells less responsive to their environment. For migrating epidermal cells, this could reduce detection of tension in the underlying neuroblasts thought to help guide the migrations. The defects in *hum-7* mutants, therefore, may combine failure to properly transmit signals within the epidermal cells, and also, failure to detect signals from cells in neighboring tissues. Tissue-specific rescue experiments of *hum-7* to resolve this would be challenging, since the overall lethality is so low. However, future experiments will need to address the tissue specificity of the signals, and of HUM-7 function in receiving these signals,

to address how the epidermis and neuroblasts cooperate during this complex migration.

Materials and Methods

Strains: The following strains were used in this study: MT324 *unc-40(n324)*, CX3198 *sax-3(ky123)*, CZ337 *vab-1(dx31)*, FT48 *xnls16[dlg-1::gfp]*, VC2436 *hum-7(ok3054)*, OX615 *hum-7(ok3054); dlg-1::gfp*, WM43 *gex-3(zu196)/DnT1*, MT5013 *ced-10(n1993)*, MT9958 *ced-10(n3246)*, JH2754 *ect-2(ax751)*, OX646 *hum-7(ok3054); ect-2(ax751)*, JJ1473 *zuls45[nmy-2::gfp]*, OX630 *hum-7(ok3054); nmy-2::gfp*, ML1154 *mcls51[plin26::vab-10 ABD::gfp]*, OX595 *hum-7(ok3054); plin26::vab-10 ABD::gfp*, SK4005 *zdls5[mec-4::gfp]*, OX350 *unc-40(n324); mec-4::gfp*, OX213 *sax-3(ky123); mec-4::gfp*, IC136 *vab-1(dx31); mec-4::gfp*, HR1157 *let-502(sb118ts)*, OX644 *hum-7(ok3054) let-502(sb118ts)*, OX635 *hmp-1(fe4); hum-7(ok3054)*, OX681 *gfp::hum-7*, OX714 *hum-7(pj62)*, OX715 *hum-7(pj63)*, ML773 *rga-2(hd102)/hln1 [unc-54(h1040)]*, OX645 *hum-7(ok3054) rga-2(hd102)/hln1 [unc-54(h1040)]*, HR483 *mel-11(sb56) unc-4(e120)/mnC1[dpy-10(e128) unc-52(e444)]*.

In vitro binding assay: This assay was based on (129). GTP-loaded and GDP-loaded GTPase constructs for CDC-42, CED-10 and RHO-1 were gifts from the Hengartner lab. The HUM-7 GAP domain construct (aa1540-1727) was cloned into the pGEX-4T2 GST vector. All the GTPase constructs were His-tagged and purified using His-Bind resin (Novagen). The GST-tagged HUM-7 construct was purified using Glutathione Sepharose 4B beads (GE Healthcare) based on manufacturers instructions. For the pull-down assay, 30µg of purified GST-tagged

proteins were incubated with 10 μ g His-tagged proteins at 4°C for two hours. Pull-downs were performed with GST beads, proteins were separated on 12% acrylamide gels, and blots were probed with antibody to His (Millipore). The GST binding assay was done at least twice using the same batch of GST-HUM-7-GAP for all of the pull-downs, and at least two sets of HIS-GTPase lysates.

RNA interference: All RNAi used in this study was administered by the feeding protocol as in (123). RNAi were constructed by cloning cDNA's of the genes into the L4440 vector and transforming them into HT115 competent cells. Small overnight bacterial cultures were diluted 1:250 and grown until the OD600 was close to 1. The culture was pelleted and resuspended in LB media containing 100 μ g/ml Ampicillin and 1mM IPTG.

Embryonic Lethality counts and imaging: Synchronized L1 worms were plated on AMP/IPTG plates containing the appropriate RNAi bacteria. Plates were cultured at 23°C for three days. Temperature sensitive mutants like *ect-2(ax751)* were cultured at three different temperatures, 15°C, 20°C and 23°C. After the three-day incubation, embryos were mounted on 3% agarose pads and lethality was counted. Embryos shown in images and graphs were cultured at 23°C unless stated otherwise.

Neuronal Migration Analysis: For *mec-4::gfp* neuronal analysis, synchronized L1 worms were plated on AMP/IPTG plates containing the appropriate RNAi bacteria

and cultured for 2-3 days at 20°C. L4440 empty vector was used as the control RNAi. The effectiveness of *hum-7* RNAi was monitored by counting the percent embryonic lethality. After incubation, L4 worms were mounted onto 3% agarose pads with 10mM levamisole to prevent frequent movement and scored for phenotypes within 15 minutes of mounting. The AVM mechanosensory neuron was checked for ventral migration defects. The table in Figure 13D is based on more than 200 worms per genotype.

RNAi-feeding Screen: To generate liquid cultures of the RNAi genes, 150µl of LB broth containing the appropriate antibiotic was pipetted into 96-well plates. Using a 96-well pin, frozen glycerol stocks of RNAi genes were transferred to the liquid media. The culture was inoculated overnight at 37°C with shaking. Cultures were spotted on 24-well NGM plates containing 2% lactose and 25µg/ml carbenicillin and grown overnight at room temperature. Approximately 20 L1 worms with the *unc-40(n324)* genotype were seeded onto the 24-well plates containing the RNAi bacteria. Worms were grown at 23°C for about three days and then their progeny screened for embryonic lethality. Clones that produced greater than 15% lethality in combination with *unc-40(n324)* were selected for secondary screening. We were particularly interested in selecting clones that had good differentiation and phenotypes that resemble Gex.

Live Imaging: Some late stage *hum-7* embryos (<2%) showed a subtle phenotype in which they developed correctly but flattened when mounted on pads for imaging.

This flat appearance may be related to the fact that hum-7 embryos behave osmotically sensitive, and have to be mounted in Egg Salts instead of water to prevent arrest during live imaging studies. Thus all embryos shown in this study were mounted in Egg Salts. For all live imaging shown, embryos at the 2 to 4 cell stage were dissected from adult hermaphrodites and mounted onto 3% agarose pads, covered with #1.5 cover slip, and sealed with Vaseline. Embryos were then incubated at 23°C for 240 minutes. Imaging was done in a temperature-controlled room set to 23°C on a Laser Spinning Disk Confocal Microscope with a Yokogawa scan head, on a Zeiss AxioImager Z1m Microscope using the Plan-Apo 63X/1.4NA or Plan-Apo 40X/1.3NA oil lenses. Images were captured on a Photometrics Evolve 512 EMCCD Camera using MetaMorph software, and analyzed using ImageJ. Using the ImageJ software, 4D movies were constructed by projecting Z-stacks at maximum intensity. All measurements were performed on raw data. For actin and myosin measurements, background intensity was subtracted by using a box or line of the same size and measuring average intensity in the same focal plane, near the embryo.

Actin Intensity measurements: To measure actin levels and dynamics, we performed live imaging of strains *plin-26::vab-10(ABD)::gfp* (Figure 16A) and *plin-26::Lifeact::mCherry* (Figure 16D). Following the 240-minute incubation of 2-4 cell embryos, embryos were imaged at 2-minute intervals for at least 120 minutes.

Figure 16A : F-actin levels were calculated in the leading cells at three different time points in minutes after first cleavage: 250/early, when migrations begin;

260/middle, when migration is underway and 280/late, when the ventral cells meet. Figure 16D shows the middle time point to allow comparison of actin levels between WT, *hum-7* and the *sax-3* mutant. To compare actin levels in the leading cells, ImageJ *box tool* was used to construct a rectangle (dotted box in figure) around the ventral edge of the leading cells (box size) and the maximum intensity was recorded.

Quantitation of F-actin intensity: Using GraphPad Prism, the maximum intensity for each analyzed embryo was graphed using a scatter plot displaying the mean with 95% Confidence Intervals (Figure 16E).

Actin Protrusion Analysis: We measured actin dynamics by evaluating protrusions and retractions in the two leading cells during early enclosure on one side of the embryo. Time “0” corresponds to the first appearance of epidermal pocket cell protrusions, at approximately 250 minutes after first cleavage in wild type. Since this is delayed in mutants like *sax-3*, timing based on the early pocket cell protrusion aligns the actin dynamics developmentally (119). For the 2 min. interval movies we examined 5 time points during the first 8 minutes of enclosure. For the 15s interval movies we examined 20 time points during the first 5 minutes of enclosure. The average number of protrusions or retractions seen in 5 time points (2 min. movies) or 20 time points (15s movies) is shown or mentioned in Results. For 2 min movies n= 10, 10, 8, 8 for controls, *hum-7*, *sax-3* and the double. For the 15s movies n= 4, 13, 6, 4 for controls, *hum-7*, *sax-3* and the double. Protrusion and retraction rates calculated from the 2 min and 15s movies were graphed using

a scatter plot displaying the mean with 95% Confidence Intervals (Figure 16E-H and text).

Imaging for *plin-26::LifeAct::mCherry;NMY-2::GFP* strains: Live imaging was done at 40X magnification using 1.3NA oil immersion objective lens. Imaging was done in a temperature-controlled room that was set at 23°C. Embryos were exposed at 30% laser power for 100ms for GFP filter at every 10 minutes, and at 35% laser power for 100ms for mCherry filter at every 2 minutes. Z stacks were made across the entire embryo using motorized z-stage, approximately 27 to 32 z-stacks total, at 1µm intervals. Controls and mutants were imaged within 3 days, under the same imaging condition for each dataset to account for technical variability.

Myosin measurements for Figure 18: To compare myosin levels as pocket cells meet, a rectangular box enclosing the pocket cells as they first touch (approximately 320min) was drawn (yellow box in Figure 18C), Time points shown and measured are those when the epidermal cells first touch based on epidermal F-actin signal. To measure myosin puncta on the same focal plane as the epidermis, we co-localized the highest *Plin-26::LIFEACT::mCherry* intensity with *NMY-2::GFP* and recorded the highest of three measurements per embryo (Figure 18B). Maximum intensity values were recorded after subtracting the average background fluorescence. The graph in Figure 18B records the relative level of *NMY-2::GFP*, after normalization of either WT, or WT on control RNAi, to 1.

Statistical Analysis:

For grouped data (Figure 16E, 3F, Figure 16E-H, 6B), statistical significance was established by performing a two-way Analysis of Variance (ANOVA) followed by the Bonferroni multiple comparison post-test. For ungrouped data (Figure 13B, 1D, Figure 14C, 2D, Figure 18A) an unpaired t-test, the unequal variance (Welch) t test, was used. Error bars show 95% confidence intervals. Asterisks (*) denote p values *= $p < .05$, ** = $p < 0.001$, *** = $p < 0.0001$. All statistical analysis was performed using GraphPad Prism.

Acknowledgments

We would like to thank the NCRR-funded *Caenorhabditis* Genetics center, Jeremy Nance, and Paul Mains for strains, and Lucas Neukomm for GTPase constructs. We thank Rutgers undergraduate Vipin Palukuri for technical assistance. Thanks to Chris Rongo, Monica Driscoll and Andy Singson for helpful comments on the manuscript and Alisa Piekny for helpful discussions.

Figure Legends

Figure 13. HUM-7/Myosin 9 interacts genetically with axonal guidance receptors and is required during embryonic morphogenesis.

A. Axonal guidance receptors regulate the CED-10/Rac1 GTPase. Active CED-10 recruits the WAVE/SCAR complex to turn on Arp2/3, which promotes branched actin nucleation. Knock down of any WAVE/SCAR pathway component leads to full embryonic lethality, while null mutations in upstream regulators cause partial embryonic lethality. To identify new morphogenesis regulators, we screened for enhancers of *unc-40* embryonic lethality.

B. The effects of loss of HUM-7 on embryonic lethality in axonal guidance receptor mutants. Genetic null mutants of three axonal guidance receptors (UNC-40, SAX-3 and VAB-1) were crossed into *dlg-1::gfp* to make scoring easier and treated with *hum-7* RNAi. For this and all graphs shown in this study, error bars show 95% confidence interval. Statistical significance: * = $p < .05$, ** = $p < 0.001$, *** = $p < 0.0001$. For panels B & D statistical significance was determined by Welch's, or unequal variances, t-test. $n > 600$ embryos. See also Table 6.

C. Postembryonic effects of HUM-7 on regulators of the WAVE/SCAR pathway. The *mec-4::gfp (zdl5)* transgene is expressed in six mechanosensory neurons. Wild type AVM axon migrates ventrally then anteriorly. Mutants show initial migrations in other directions, including a complete loss of ventral migration (*sax-3(ky123)*). Micrographs show representative ventral migration patterns of AVM axon, reflected in cartoons below (green cells). Black line = ventral nerve cord.

Second neuron is the ALM, shown to orient the worm positioned anterior to the left.

D. Table summarizing ventral migration AVM defects. More than 200 neurons were analyzed for each genotype.

E. *C. elegans* HUM-7 shares similar domains and sequence homology with human Myo9a and Myo9b. All three proteins possess a Ras-associated (RA) domain, which is embedded in the Ubitiquin (UBQ) domain of human Myosin-IXa, a myosin 9/IX domain and a RhoGAP domain. Both human Myo9 proteins have one phorbol ester/diacylglycerol-binding domain (C1) while HUM-7 has two. The percent sequence identity between *C. elegans* HUM-7 and the human Myosin 9 proteins are listed between domains (within labeled domains) and overall (on right).

Figure 14. HUM-7/Myosin 9 interacts genetically and molecularly with Rho GTPases.

A. Molecular model of the *C. elegans* Myosin IX protein, HUM-7, includes N-terminal myosin, two IQ, two C1 and RhoGAP domains. Genetic mutations from the *C. elegans* Consortium (*ok3054* deletion) or from our CRISPR studies are indicated: *pj62* deletion, *pj63* GAP mutant and *pj72* endogenous CRISPR N-terminal GFP tag, OX681 *hum-7(pj72[*gfp::hum-7*]* (see Fig. 3).

B. Embryonic morphogenesis defects in *hum-7* mutants observed with DIC optics. Embryos are positioned with anterior to the left and dorsal up here and elsewhere unless otherwise noted. Thicker white arrows indicate anterior intestine while thinner arrows indicate anterior pharynx. Some *hum-7* mutants arrest during

ventral enclosure (top row), similar to embryos missing *ced-10/Rac1* or WAVE complex components like *gex-3*. *Bottom row*: Other *hum-7* embryos arrest at the 2-fold stage, similar to mutants that regulate RHO-1. Single white arrow points to swollen anterior region, a RHO-1 pathway phenotype. All embryos shown were grown at 23°C and mounted in Egg Salts (See Materials and Methods).

C. Embryonic lethality percentages in genetic doubles of *hum-7* and axonal guidance mutants. At least 900 embryos were counted for each genotype.

D. Embryonic lethality percentages in genetic and RNAi doubles of *hum-7* and GTPase mutants. We analyzed the three main *C. elegans* GTPases (RHO-1, CED-10 and CDC-42). We combined a hypomorphic allele of CED-10 (*ced-10(n1993)*) with *hum-7* RNAi, RNAi of *cdc-42* with the *hum-7(ok3054)* mutant allele, and a hypomorphic allele of a RHO-1 guanine exchange factor (*ect-2(ax751)*) with *hum-7* RNAi. n>600 per genotype. See also Table 6.

E. The GAP domain of HUM-7 was tagged with GST and used in a GST pull-down assay to test binding between three HIS-tagged GTPases (RHO-1, CDC-42 and CED-10) in both the active GTP-bound (Q63L, Q61L and Q61L) and inactive GDP-bound (T19N, T17N and T17N) states. The pull-down assays were performed with double the concentrations of the loading controls shown. The GST binding assay was done at least twice.

Figure 15. HUM-7 is expressed in muscles, and regulated by SAX-3/ROBO.

GFP::HUM-7 expression in 3-fold embryos (top panel, A), young adults (A mid and lower panels, B and C) and L4 larvae (D). **A.** Beginning in late embryos,

GFP::HUM-7 expression is enriched in the body wall muscles, as shown by overlap with Pmyo-3::RFP. Strong signal in the posterior bulb of the pharynx begins in late embryos.

B. HUM-7 expression in the striated muscle fibers was verified in the larvae by double-labeling with anti-muscle antibody 5.6 (149) in young adults.

C. Comparison of expression to HMR-1::mKATE2. HMR-1/E-Cdh is enriched at apical epithelia (top panel, epidermal seam cells; bottom panel, apical pharynx) and in the nerve ring (boxed region, anterior arrow).

D. Effects of mutations in axonal guidance proteins on levels of GFP::HUM-7. White arrows point to the posterior bulb of the pharynx, yellow lines cross body wall muscle. Maximum intensity at the pharynx, **E**, and body wall muscles, **F**, was compared.

Figure 16 HUM-7 affects F-actin levels and dynamics in migrating epidermis during embryonic morphogenesis.

F-actin levels in embryos during epidermal enclosure visualized by Plin-26::vab-10-ABD::GFP (137) for panels A- C and Plin-26::LIFEACT::mCherry (103) for panels D-H.

A, B. Epidermal F-actin levels in *hum-7(ok3054); plin-26::vab-10(ABD)::gfp*. Embryos were imaged at two-minute intervals beginning at 240 minutes after first cleavage. Images shown here represent embryos at the early (250 min), middle (270 min) and late (285 min) stages of epidermal enclosure. Yellow boxes: highest signal was measured in the leading cells. Embryos were pseudo-colored using the

“Fire” function in Image J, and intensity is shown from low (blue) to high (yellow). See also S1 Movie.

C. Ventral enrichment of F-actin in migrating epidermal cells in *hum-7(ok3054)* embryos. Close-ups of representative epidermal leading cells with the ventral (V) edge at the bottom and the dorsal (D) region at top. Intensity of F-actin in the leading cells during protrusion initiation was analyzed with a ventral to dorsal line through the leading cells (Plot Profile tool, ImageJ). Two graphs use different y-axis scales due to higher F-actin levels in *hum-7(ok3054)*. n=10 embryos per genotype. See also S2 Movie.

D. *plin-26::Lifeact::mCherry* transgenic line (103), in control animals and embryos depleted of *hum-7*, *sax-3* or both.

E. The maximum F-actin intensity measured in ventral leading edge cells 270 minutes after first cleavage using ImageJ, “line tool”.

F,G, H. Effects of *hum-7* and *sax-3* on the rate of dynamic actin protrusions. Using movies shown in D, average F-actin protrusions or retractions per time point in two leading cells. **F:** representative images. Arrows mark protrusions and asterisks mark retractions. Beginning at leading edge migration, average protrusions (G) and retractions (H) during 8-minute period were measured. For this panel only the exposure of individual images are enhanced to better show protrusions and retractions. See also S2 Movie.

Figure 17 NMY-2::GFP colocalizes with F-actin in epidermal cells during enclosure.

A. Cartoon of embryos, ventral side up, during ventral enclosure. Magenta: epidermis; gray: neuroblasts.

B-E. To measure myosin in the epidermal cell focal plane, endogenously tagged *nmy-2::gfp* (myosin) was crossed into *plin-26::Lifeact::mCherry* (F-actin), which is expressed only in epidermis. WT embryos incubated at 23°C are shown at three different z-planes, 1 μm apart, three time points after first cleavage. **B.** 270 minutes: four leading edge cells have almost met at ventral midline. In leading edge cells, fluorescence intensity was measured: (B') from ventral to dorsal in middle of cell, to compare ventral enrichment of NMY-2::GFP and F-actin; (B'') from ventral to dorsal along lateral cell boundary; and (B''') across two cell-cell membranes of the same cell. Color of surrounding box indicates z plane used. **C.** 290 minutes: leading edge cells have met at ventral midline, pocket cells have not. (C') Intensity measured across two pocket cells that have not met. **D.** 300 minutes: pocket cells meet at ventral midline. **E.** Orthogonal view of the middle of z-plane from **D** shows overlapping signals of myosin and epidermal F-actin.

Figure 18 SAX-3/HUM-7/RHO-1 regulate non-muscle myosin, NMY-2, in epidermal cells.

A. Genetic interactions of *hum-7*, *sax-3*, *vab-1* and known RHO-1 pathway mutants *let-502* and *mel-11*. Experiments shown were done at 23°C except for the *let-502(sb118ts)* experiments done at 25.5°C.

B. Quantitation of NMY-2::GFP levels in the ventral pocket cells at 300 minutes, when pocket cells of control embryos meet at midline. Graph shows mean maximal

fluorescent intensity at pocket cells, relative to WT or relative to control RNAi, normalized to 1. **C.** Representative images of embryos used in B. Yellow boxes: region measured. **D.** SAX-3 is proposed to negatively regulate HUM-7, which functions as a GAP to attenuate RHO-1 activity and thus reduce actomyosin contractility through NMY-2, non-muscle myosin heavy chain 2. We propose tight regulation of NMY-2-dependent acto-myosin contractility promotes timely ventral enclosure.

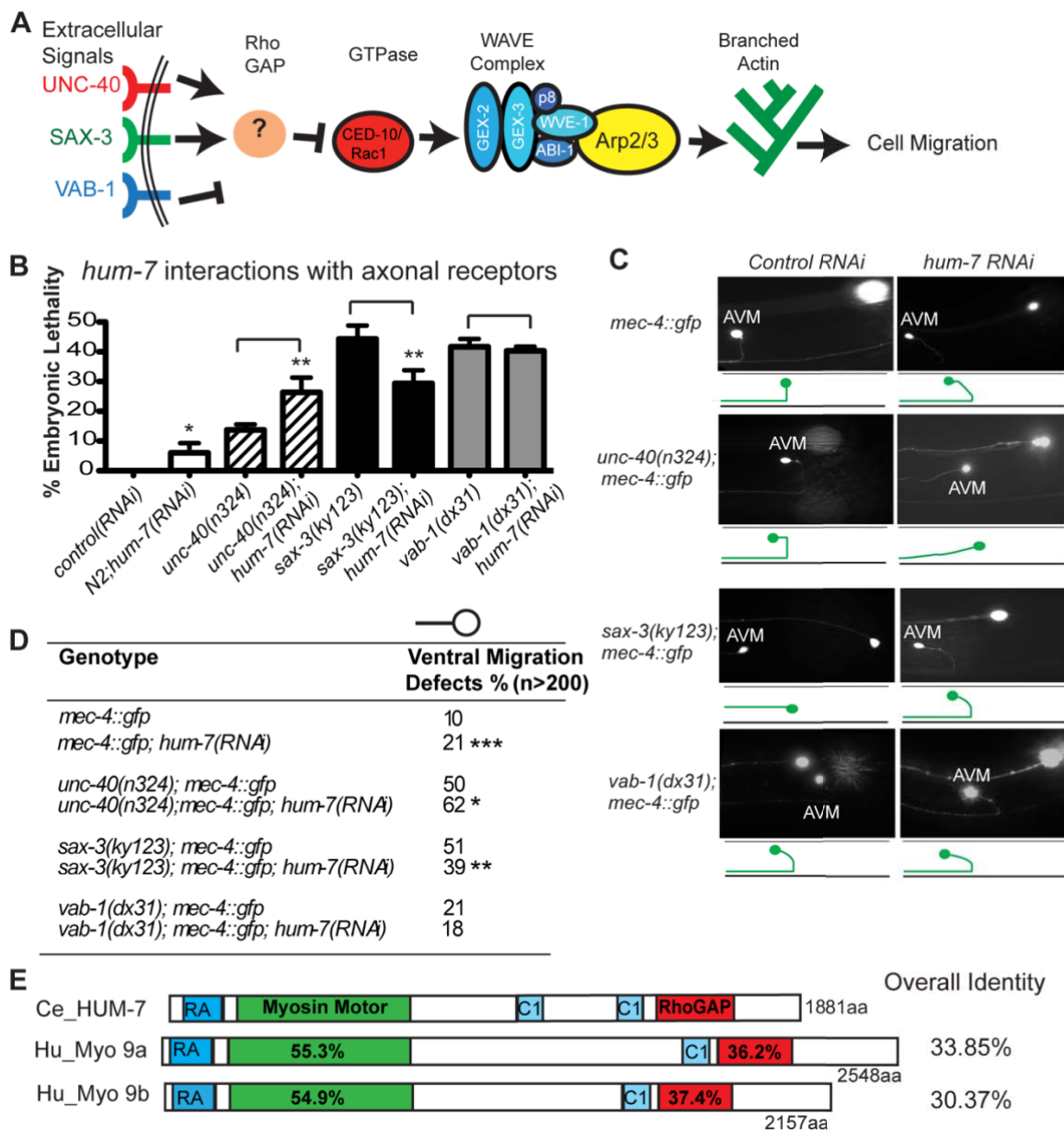


Figure 13 HUM-7/Myosin 9 interacts genetically with axonal guidance receptors and is required during embryonic morphogenesis.

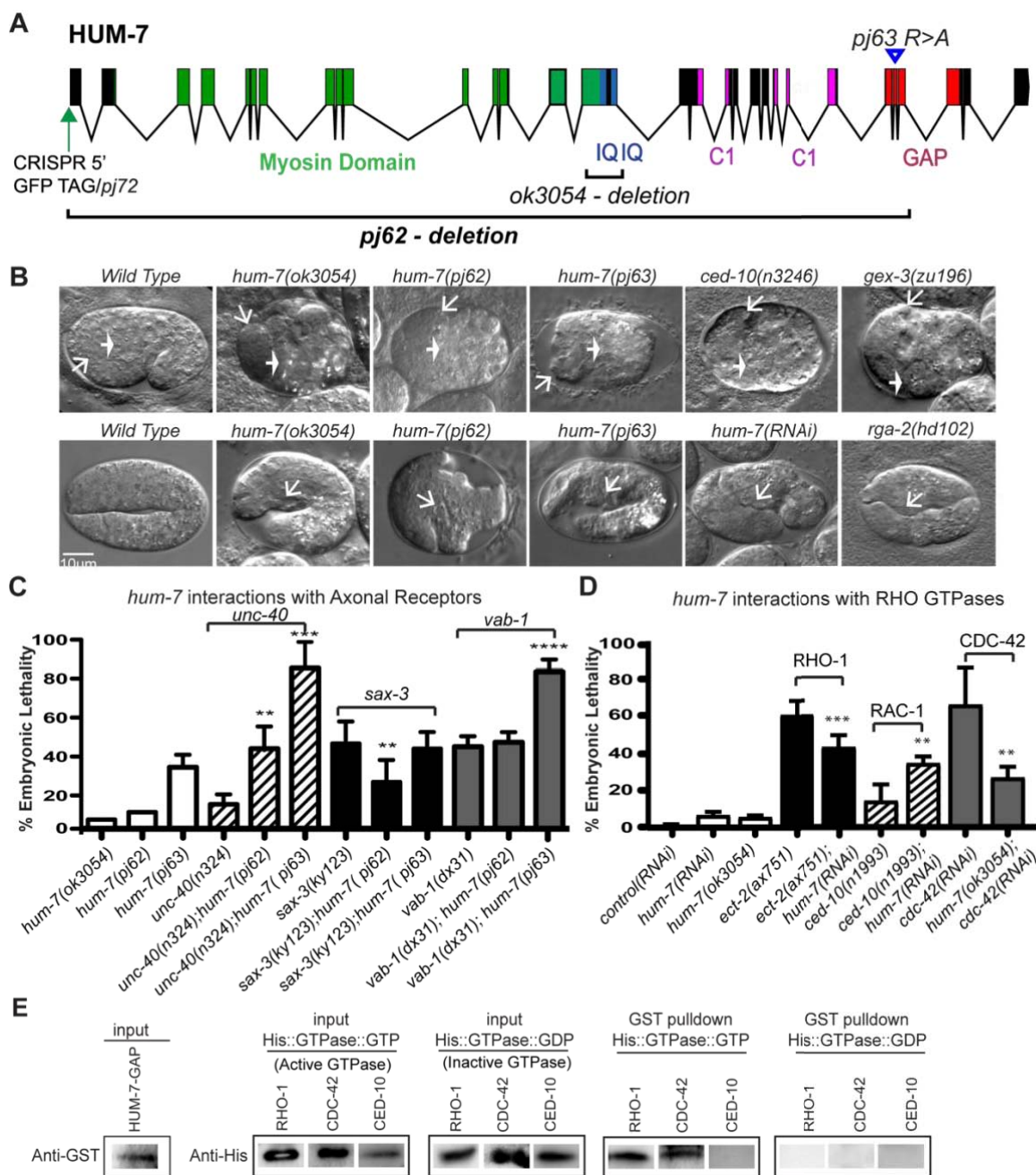


Figure 14 HUM-7/Myosin 9 interacts genetically and molecularly with Rho GTPases.

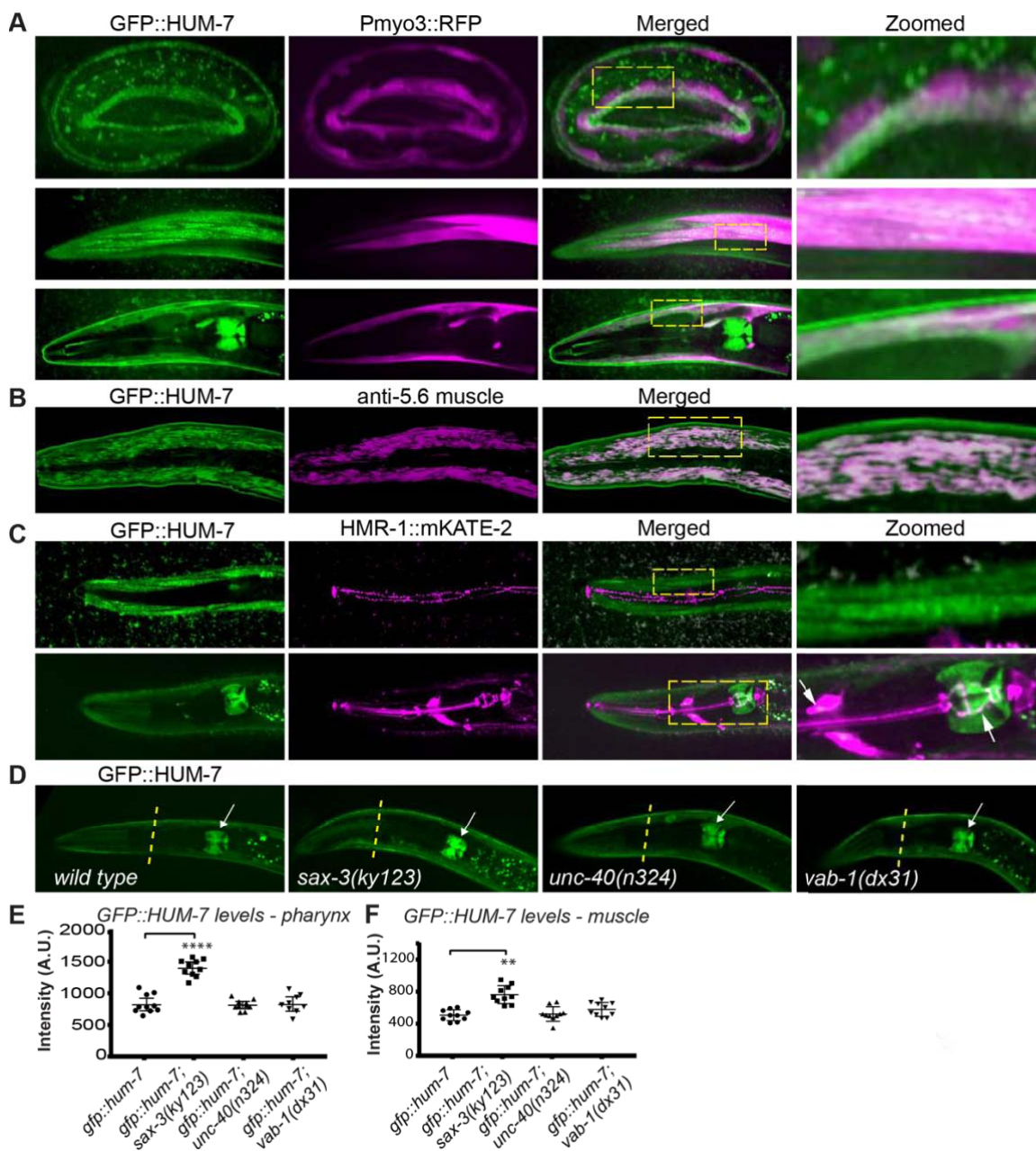


Figure 15 HUM-7 is expressed in muscles and regulated by SAX-3/ROBO.

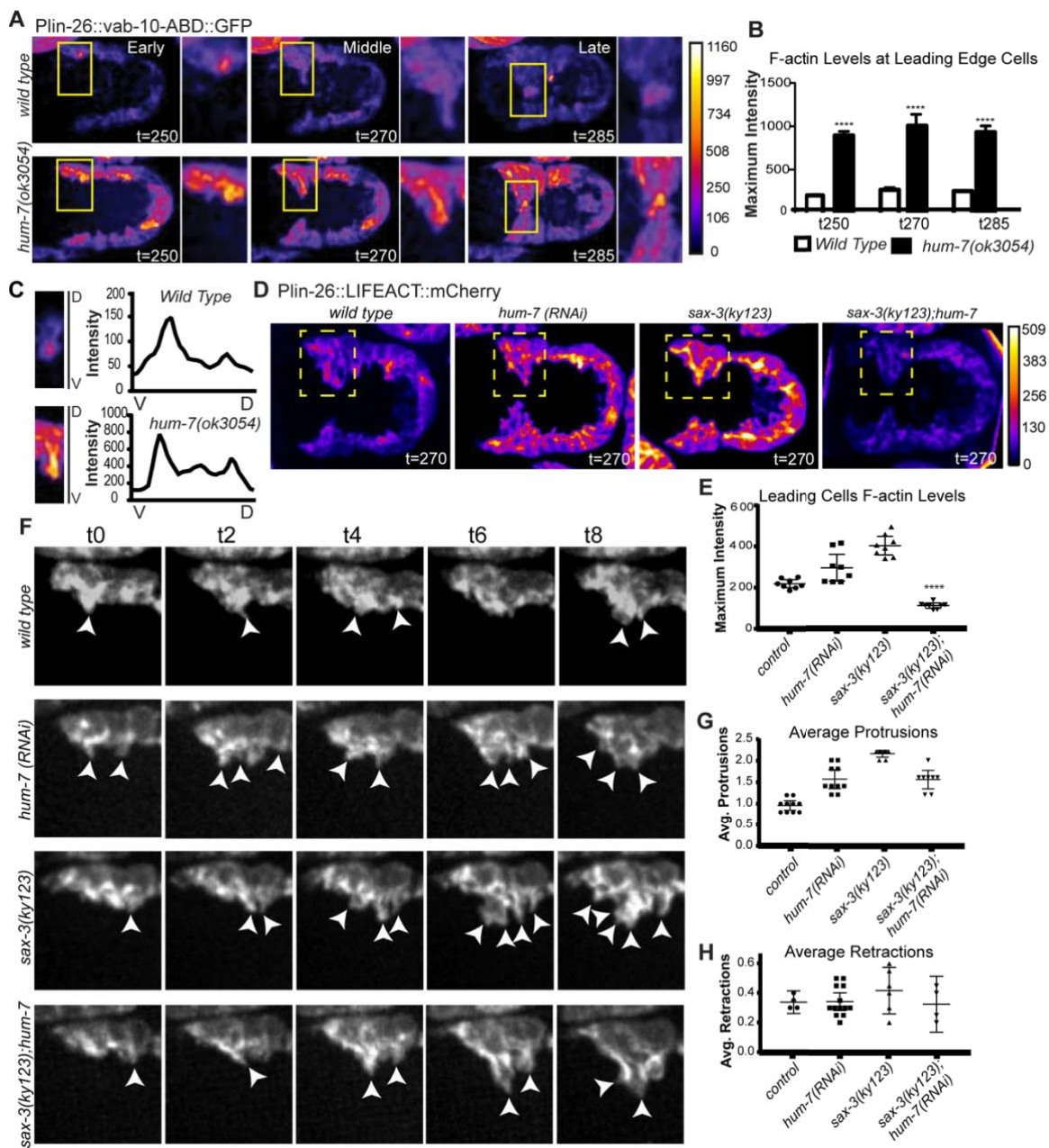


Figure 16 HUM-7 affects F-actin levels and dynamics in migrating epidermis during embryonic morphogenesis.

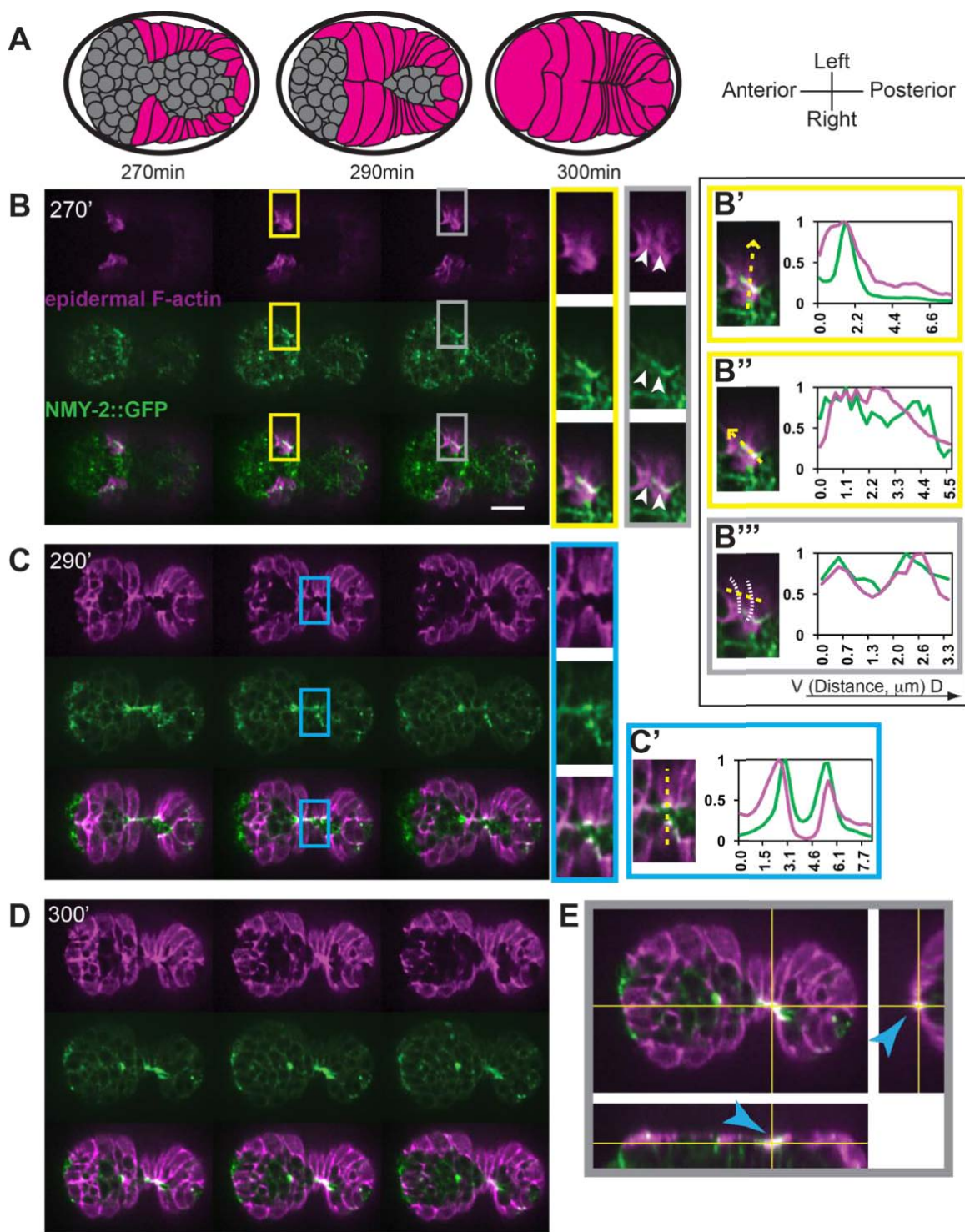


Figure 17 NMY-2::GFP colocalizes with F-actin in epidermal cells during enclosure.

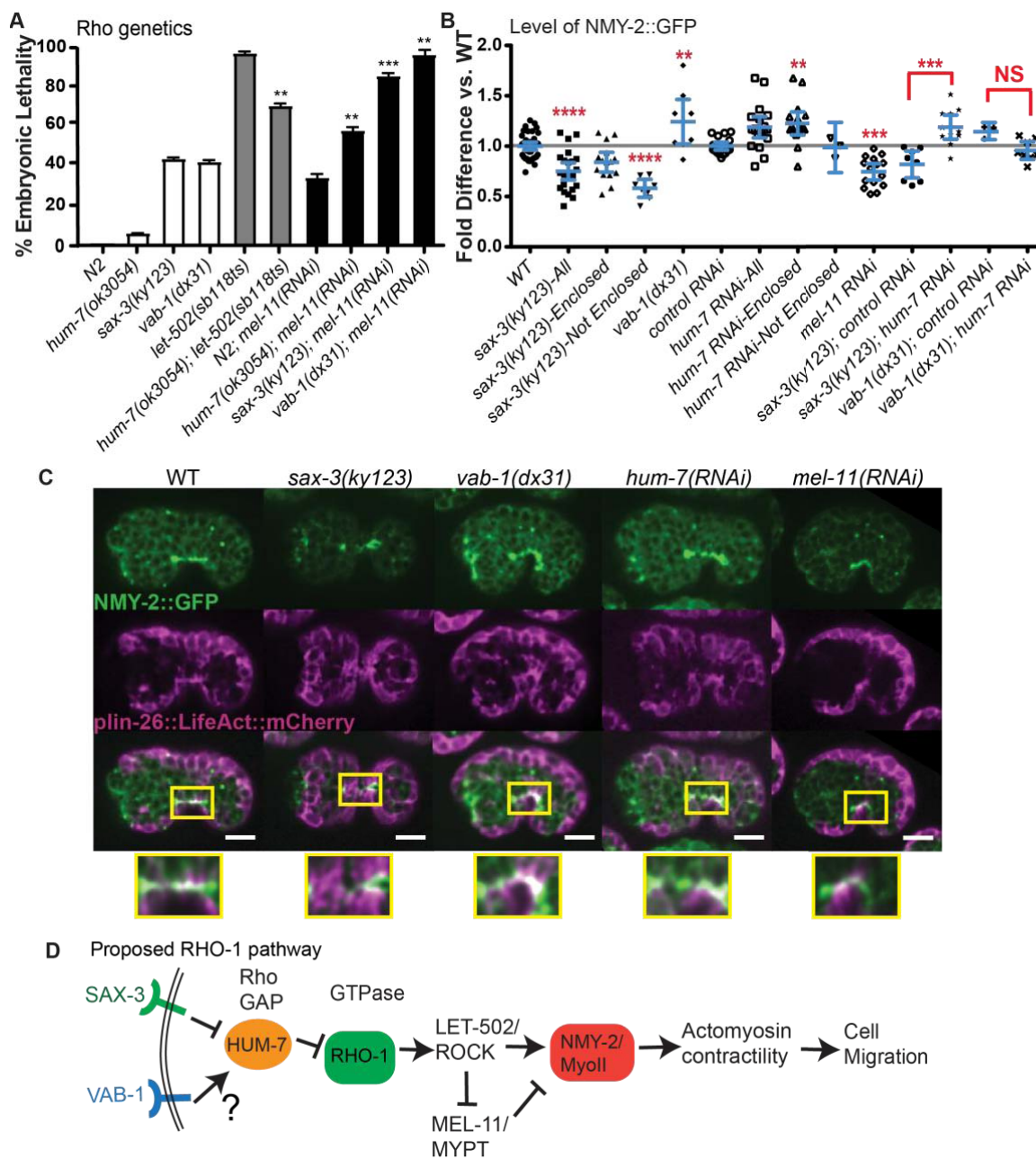


Figure 18 SAX-3/HUM-7/RHO-1 regulate non-muscle myosin, NMY-2, in epidermal cells

Table 6 Embryonic lethality due to the loss of *hum-7*.Related to *Figure 13B*, *Figure 14C-D*, *Figure 17A-B*.

Genotype	Temp	% Lethality^a	n^b
<i>N2; control RNAi^c</i>	20°C	0.33	1273
<i>N2; hum-7(RNAi)</i>	20°C	6.53	1929
<i>hum-7(ok3054); control(RNAi)</i>	20°C	5.53	1574
<i>ect-2(ax751)</i>	20°C	42.3	2112
<i>ect-2(ax751); hum-7(RNAi)</i>	20°C	27.77	2386
<i>ced-10(n1993); control(RNAi)</i>	20°C	14.13	1094
<i>ced-10(n1993); hum-7(RNAi)</i>	20°C	34.37	676
<i>ced-10(n3246); control(RNAi)</i>	20°C	14.6	1434
<i>ced-10(n3246); hum-7(RNAi)</i>	20°C	33.03	1317
<i>N2; cdc-42(RNAi)</i>	20°C	65.9	1006
<i>hum-7(ok3054); cdc-42(RNAi)</i>	20°C	26.6	1126
<i>wsp-1(gm324); control(RNAi)</i>	23°C	18.4	880
<i>wsp-1(gm324); hum-7(RNAi)</i>	23°C	11.4	1044
<i>unc-40(n324); control(RNAi)</i>	20°C	13.67	655
<i>unc-40(n324); hum-7(RNAi)</i>	20°C	26.33	683
<i>sax-3(ky123); control(RNAi)</i>	20°C	44.33	777
<i>sax-3(ky123); hum-7(RNAi)</i>	20°C	29.33	981
<i>vab-1(dx31); control(RNAi)</i>	20°C	41.67	617
<i>vab-1(dx31); hum-7(RNAi)</i>	20°C	40.33	710
<i>N2; control RNAi</i>	23°C	1	1509
<i>N2; hum-7(RNAi)</i>	23°C	6	2016
<i>hum-7(ok3054); control(RNAi)</i>	23°C	5.8	1123
<i>N2; rga-2(RNAi)</i>	23°C	6	2158
<i>hum-7(ok3054); rga-2(RNAi)</i>	23°C	3	1851
<i>ect-2(ax751); control(RNAi)</i>	23°C	60.6	1808
<i>ect-2(ax751); rga-2(RNAi)</i>	23°C	48.8	1822
<i>N2; let-502(RNAi)</i>	23°C	26.7	1064
<i>hum-7(ok3054); let-502(RNAi)</i>	23°C	16.2	1120
<i>let-502(sb118ts)</i>	25.5°C	98	1052
<i>hum-7(ok3054) let-502(sb118ts)</i>	25.5°C	72	1221
<i>N2; mel-11(RNAi)</i>	23°C	35.6	936
<i>hum-7(ok3054); mel-11(RNAi)</i>	23°C	59.5	902

<i>hum-7(pj62) Full Length Deletion</i>	23°C	9.5	1570
<i>hum-7(pj63) GAP mutant</i>	23°C	32.8	1004
<i>hum-7(pj62),unc-40(n324)</i>	23°C	42	612
<i>hum-7(pj63);unc-40(n324)</i>	23°C	84.3	650
<i>hum-7(pj63);sax-3(ky123)</i>	23°C	41.8	698
<i>hum-7(pj63);vab-1(dx31)</i>	23°C	82.2	702
<i>sax-3(ky123);hum-7(pj62)</i>	23°C	24.9	661
<i>sax-3(ky123);mel-11 (RNAi)</i>	23°C	87.1	601
<i>sax-3(ky123);let-502 (RNAi)</i>	23°C	49.4	774
<i>sax-3(ky123);nmy-2 (RNAi)</i>	23°C	95.5	791
<i>vab-1(dx31);hum-7(pj62)</i>	23°C	44.7	883
<i>vab-1(dx31);mel-11 (RNAi)</i>	23°C	98.7	849
<i>vab-1(dx31);let-502 (RNAi)</i>	23°C	12	617
<i>vab-1(dx31);nmy-2 (RNAi)</i>	23°C	96.2	640

Genotype	Temp	% Lethality^a	n^b
<i>unc-40(n324); control(RNAi)</i>	20°C	13.67	655
<i>unc-40(n324); hum-7(RNAi)</i>	20°C	26.33	683
<i>sax-3(ky123); control(RNAi)</i>	20°C	44.33	777
<i>sax-3(ky123); hum-7(RNAi)</i>	20°C	29.33	981
<i>vab-1(dx31); control(RNAi)</i>	20°C	41.67	617
<i>vab-1(dx31); hum-7(RNAi)</i>	20°C	40.33	710

Footnotes:

^a Lethality counts were done after plating L4 hermaphrodites for three days at the stated temperature.

^b Lethality counts from at least three experiments are shown.

^c The empty vector L4440 was used to make control RNAi food.

Table 7 Terminal embryonic phenotypes caused by loss of *hum-7*.

Genotype	Phenotypes - %			Total % lethal	n
	Poor differentiation ^a	Gex	2-fold defects ^b		
<i>N2; control RNAi</i> ^c	0	0.3	0.7	1	1507
<i>N2; hum-7(RNAi)</i>	0.1	2.3	3.6	6	913
<i>hum-7(ok3054); control RNAi</i>	0	2.5	3.3	5.8	833
<i>N2; rga-2(RNAi)</i>	0	2.4	3.6	6	1071
<i>hum-7(ok3054); rga-2(RNAi)</i>	0.1	1.6	1.3	3	1008
<i>ect-2(ax751); control RNAi</i>	2	27	31	60.6	1808
<i>ect-2(ax751); hum-7(RNAi)</i>	1	17	25	43	995

Footnotes:

^a Embryos scored by DIC showed cells without specific fates, and some had fewer cells.

^b Includes 2-fold arrest and rupture at the 2-fold stage.

^c The empty vector L4440 was used to make control RNAi food.

^d All experiments done at 23°C.

CONCLUSION

There are many advantages on the use of *C. elegans* as a model system to study biological processes. *C. elegans* is a small nematode that has a short life cycle, making it a very attractive model system to be used to study developmental processes. In addition, *C. elegans*' transparent body allows researchers to view the fine details of the organism under the Nomarski (differential interference contrast, DIC) optics. Coupled with the use of fluorescent protein, live-imaging of *C. elegans* can be done to study the progression of biological process *in vivo*. Many other features of *C. elegans* that make it a very attractive model system in biology are large brood size, low maintenance, fixed cell number and development, and long-term cryopreservation (150).

However, one main challenge to study morphogenesis, in general, is the requirement of tissue-tissue interaction for efficient and precise morphogenetic movement. This makes it difficult to distinguish whether a mutant generated is acting in a cell-autonomous or non-cell autonomous manner. One approach in the field is to generate a homozygous mutant and re-introduce protein expression in a tissue-specific manner. However, several reported cases showed that rescue can be done in several tissue types individually, which further complicates the analysis of the phenotype. One possibility is that each protein may have a different function in different tissue types. One protein might be crucial in one tissue type but is dispensable in another. In this thesis, we add two more proteins to be involved in the signaling pathway involved during epidermal morphogenesis (12).

Additional information gained from this thesis

1. Actomyosin contractility role during ventral enclosure

Actomyosin contractility in the epidermal cells has been shown to regulate epidermal morphogenesis during elongation stage of *C. elegans* embryogenesis (3, 4). This is regulated by the action of non-muscle myosin 1 and 2 (NMY-1 and NMY-2) on the actin filament along the lateral epidermal seam cells (151). Myosin is regulated by the phosphorylation and dephosphorylation of its regulatory myosin light chain (MLC-4/rMLC) through the action of Rho-binding kinase (ROCK/LET-502) and myosin phosphatase (MYPT/MEL-11), respectively. Phosphorylated myosin induced contractility, thereby increasing the tension along the actin filaments, while dephosphorylated myosin released the tension along the actin filaments. Mutations on rMLC/ MLC-4, NMY-1, NMY-2 or ROCK/ LET-502, all caused shortened *C. elegans* larvae, suggesting severe elongation defects (45, 151, 152), consistent with their role in positively regulating the actomyosin contractility. Mutation of MYPT/MEL-11 caused hypercontractility of the epidermal cells during elongation, causing embryonic rupture (45, 46), consistent with its role to negatively regulating the actomyosin contractility. While the role of actomyosin contractility regulated by RhoA/RHO-1 had been clearly defined during elongation, not much is known about its role during ventral enclosure. Our study tries to shed the light on its role.

First, we draw similarity for the role of actomyosin contractility from the observation of the rate of leading-edge epidermal cells migration during ventral enclosure. Faster or delayed ventral enclosure rate might be a phenotype of

actomyosin, the ability of the cells to move efficiently without disrupting the entire integrity and maintain their stiffness. We saw mutants with delayed epidermal leading-edge cells migration in our study. Second, we quantify the amount of measurable NMY-2/myosin II in the migrating ventral cells. We show that the level of NMY-2/myosin II in the contralateral pocket cells as they meet at the ventral midline can be faithfully measured and we can correlate this level with the ability for the cells to distribute contractility during cell migration for efficient ventral enclosure. Indeed, we saw that mutants with low NMY-2/myosin II usually have delayed leading-edge cells migration (Figure 12). Further analysis will need to be done to verify the role of NMY-2/myosin II in the migrating epidermal cells.

2. Additional Rho GTPase activating protein (GAP) work to regulate epidermal morphogenesis

In this study, we discovered two other players of *C. elegans* epidermal morphogenesis. One is HUM-7/MyoIX, shown to be working with RHO-1/RhoA GTPase to regulate actomyosin contractility (12). RNAi treatment of *let-502* on *hum-7* mutant resulted in rescue of embryonic lethality, while RNAi treatment of *mel-11* on the same mutant resulted in enhancement of embryonic lethality, suggesting that HUM-7 works in the RhoA/RHO-1 pathway (12). As expected, we saw *hum-7* mutant caused an increase in NMY-2/MyosinII level in the migrating pocket epidermal cells. This is consistent with HUM-7/MyoIX reported role to inactivate RhoA/RHO-1 in the vertebrate system (153). Therefore, removing the inactivating signal caused an increase RhoA/RHO-1 activity, which is reflected in

increased NMY-2/MyoII level at the membrane front of migrating epidermal pocket cells during *C. elegans* epidermal morphogenesis.

Surprisingly, we saw a decrease in NMY-2/MyosinII level in the migrating pocket epidermal cells in embryos treated with *mel-11 RNAi*. This is inconsistent with its role to inactivate dephosphorylation activity of MLC-4/rMLC that reduced the activity of NMY-2/MyosinII. During elongation, MLC-4/rMLC and LET-502/ROCK had been shown to act on the lateral seam cells to control actomyosin contractility (45, 152). Instead, expression of MEL-11/MYPT was shown to have low expression in the dorso-ventral epidermal cells (46). This complementary pattern of expression in different tissues suggest that myosin is controlled differently in these two types of cells. Our measurement was done right when the ventral enclosure had finished and on the ventral epidermal cells, suggesting that there are either (1) additional players or (2) different mechanisms for NMY-2/Myosin II dephosphorylation in the RhoA/RHO-1 pathway during ventral enclosure. Further study will need to be done to understand the role of MEL-11/MYPT on NMY-2/MyosinII during ventral epidermal enclosure in *C. elegans*.

Another player is RGA-8, which we show to be work with CDC-42 GTPase (Chapter 2). CDC-42 has been shown to be involved in some processes that occur during the epidermal morphogenesis stage of *C. elegans* embryonic development. In one study, CDC-42 was shown to be involved in dorsal intercalation, a process that occurs simultaneously during ventral enclosure. During this process, CDC-42 functions together with the PAR complex to efficiently form and orient the cell tips towards the direction of intercalation (43). Additionally, CDC-42 was also shown to

be required in the elongation process; it regulates proper attachment of junctional actin. Without *cdc-42*, the circumferential actin belt fails to properly attach to the cell membrane, eventually causing the embryos to rupture due the loss of junctional integrity during elongation. Interestingly, Zilberman et al also observed a role of CDC-42 during ventral enclosure but did not characterize its role during this process further (96). Another study examined the role of CDC-42 during ventral enclosure and found a different GAP, RGA-7/SPV-1, that regulates CDC-42 in this process. In this study, CDC-42 pathway was shown to be involved in the actin protrusions of the leading-edge cells and the formation of new junctions as the leading-edge cells from the opposite ends meet at the ventral midline (99). We are at an exciting moment for understanding the role of CDC-42 during different stages of epidermal morphogenesis.

In my study, we focused on the role of CDC-42 on ventral enclosure and addressed two key biological questions; (1) which GTPase activating protein (GAP) interactor of CDC-42 regulates ventral enclosure, and (2) which downstream pathway of CDC-42 does the GAP protein control. We found a GAP, RGA-8, that functions together with CDC-42 to regulate ventral enclosure by regulating the level and dynamics of actin and non-muscle myosin (NMY-2) in the epidermal cells (Figure 5, 6, 9, 10). As an inactivating signal for the GTPase CDC-42, we screened for the inability of each of the 23 GAPs candidate in *C. elegans* (54) to rescue embryonic lethality in the *cdc-42 RNAi* hypomorphic mutant. We found RGA-8 regulates CDC-42 based on *cdc-42 RNAi* lethality rescue on *rga-8* null allele, *pj60*. The mutant *pj60* can also rescue the lethality of *toca-2(ng11);toca-*

1(tm2056) double mutant, a well-known interactor of CDC-42 to regulate branched actin pathway via the action of WSP-1/WASP (97). Interestingly, *wsp-1(gm324); rga-8(pj60)* double mutants resulted to the same embryonic lethality as *wsp-1(gm324)* mutants, which could indicate *wsp-1* is epistatic to *rga-8*. Collectively, our genetics data suggests that WSP-1 functions downstream of TOCA-1/TOCA-2 and RGA-8 (Figure 2). Interestingly, we found that RGA-8 affect both F-actin and NMY-2/myosin II accumulation in the cells. Therefore, we found an additional pathway that controls NMY-2/myosin II during ventral enclosure by CDC-42 GTPase.

Future directions

To further understand the role of actomyosin contractility during specific stages of epidermal morphogenesis in *C. elegans*, there is a need for epidermal-specific expression of NMY-2::GFP to study the exact pattern of migrating and elongating epidermal cells. Further, an epidermal-specific mutant of the GTPase can be generated to see if there's any effect on epidermal-specific NMY-2::GFP. Our study raised more questions on the role of NMY-2/myosin II in the migrating cells. Mainly, what is the role of NMY-2/myosin II in the migrating epidermal cells? During migration, cells generate several actomyosin-dependent structures, including focal adhesions, and stress fibers. In addition, NMY-2/myosin II had also been shown to be involved in regulating actin turnover. Therefore, future studies are needed to understand further the molecular regulation involved during epidermal morphogenesis in *C. elegans*.

APPENDIX I: Cloning

CRISPR strategy to generate mutants and fluorescent-tagged genes

Acknowledgement: I would like to express my gratitude to Helen Ushakov for helping with microinjection of the plasmid constructs into the worm germ line for most of the strains generated in this thesis. I would also like to thank Eric Larsen and Andre G. Wallace for technical assistance and helpful discussions during generation of the strains using the CRISPR strategy.

INTRODUCTION

Bacteria and archaea have evolved immune defense system that use RNA-directed enzyme, to degrade foreign DNA. The system is called clustered regularly interspaced short palindromic repeat (CRISPR)/CRISPR-associated (Cas), CRISPR/Cas in short, and is vastly diversified across bacterial species and can be categorized into four types (154-156). Type II of the CRISPR-Cas system was engineered as a tool for robust and precise gene editing technology, using the enzyme Cas9 (113, 157-160). First popularized in 2013, this strategy is adapted into biological research as a tool for precision genomic modifications in multiple systems. In *C. elegans* field, several methods were developed to generate the most efficient tools to modify the genomic DNA by several labs using CRISPR method (114, 115, 161-163). In this section, I summarized the strategies in detail that were used during the course of my thesis project to generate the specific mutants in Chapter 2.

RESULTS

Step 1: Find a good PAM site

Cas9 enzyme requires the protospacer adjacent motif (PAM) site, characterized by the NGG sequence at the 3' end of the desired cut site (158). CRISPR target PAM sequence was manually searched at, or near, the desired mutation site. Consequently, the selected desired region for cutting was screened on the CRISPR MIT website generated by Zhang lab to account for off-target effects. In most cases, the gRNA with the least number of off-targets loci on the same chromosome will be used for further experiment.

Step 2: Generation of single-guide RNA (sgRNA)

The Cas9 requires two types of RNA to perform sequence-specific cleavage of targeted double-stranded DNA. The first is the CRISPR RNA (crRNA) containing the targeted sequence for DNA cleavage, and the second is the trans-activating CRISPR RNA (tracr-RNA) required by the Cas9 enzyme to assist in the cleavage (158). In multiple systems, it was shown that fusing both RNA types into single-guide RNA (sgRNA) is sufficient to induce the DNA cleavage by Cas9. In the *C. elegans* system, sgRNA expressed under the U6 small nuclear RNA (snRNA) is cloned into any plasmid vector to allow for expression of sgRNA (162). Below are the two strategies used to generate sgRNA throughout the thesis.

Strategy 1: Sewing PCR

To generate the sgRNA, we used a sewing PCR method that was used by the Mello lab (Figure 19, (114)). First, the left arm of the construct was generated with the primer pair MSo1204 and a reverse primer containing the cut site region (eg, MSo1305). This arm contains the U6 promoter and ends with the homologous sequence that is upstream of the PAM site, where the desired cut site will be. The

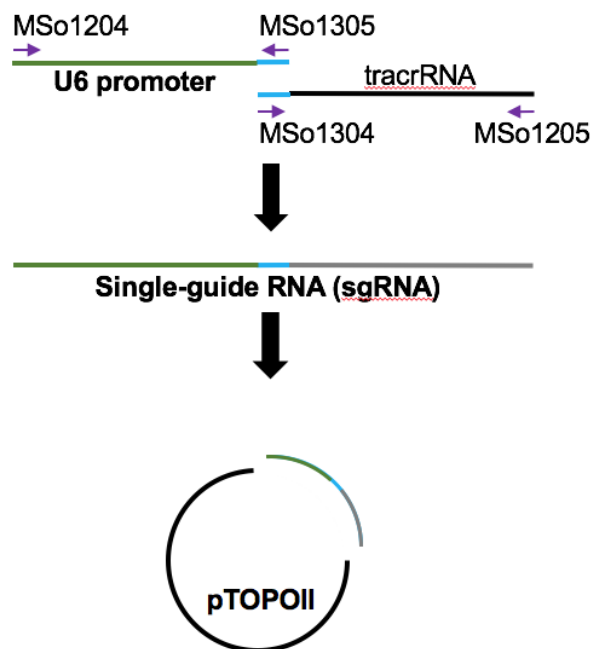


Figure 19 Sewing PCR strategy to generate the sgRNA

Source: (114)

second right arm of the PCR was generated with the primer pair MSo1205 and a forward primer containing the same cut site region (eg, MSo1304). This arm starts with the homologous sequence that is immediately upstream of the PAM site (eg, complementary to MSo1305) and is contiguous to the tracrRNA sequence that is required for DNA cutting activity by the Cas9 enzyme. These two PCR products were mixed at 1:1 ratio and diluted to 1:10 and 1:50. The diluted mixture was then used as a template for PCR with primer MSo1204 and MSo1205, generating a single, contiguous PCR product. The sewn PCR product was gel-purified and cloned into TOPO-II vector using the protocol provided by the company (Invitrogen,

Catalog# K800-20). All clones were verified by DNA sequencing prior to further use. All primers used are listed in Table 8.

Strategy 2: Plasmid cloning

As the lab progresses to using the CRISPR method more heavily, a new strategy from the Fire lab provides a more efficient way to generate sgRNA (115). I used this method to generate all of my strains in Chapter 2 (RGA-8 R277A).

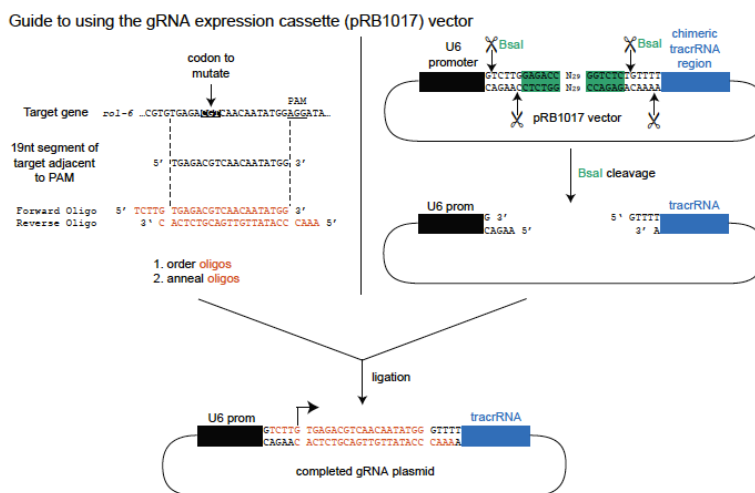


Figure 20 Generation of sgRNA in a plasmid vector

Source: (115).

Plasmid pJP118 (referred to as pBR1017 in (115) and Figure 20) were cut with Bsal restriction enzyme. Two complementary primers flanked with Bsal overhang were designed upstream of the PAM site and annealed in a reaction tube. These primers were then ligated to the digested pJP118 and cloned into *E. coli* DH5 α . The resultant plasmids were sequenced prior to further use in the CRISPR experiment. All primers generated in this method are listed in Table 8.

Step 3: Screening for sgRNA-guided cutting efficiency

Prior to using the sgRNAs for their intended purpose, they were tested independently to ensure that they are able to guide Cas9 for cutting the *C. elegans* genome. To this end, we employed co-CRISPR injection strategy with verified sgRNA and rescue primer that identifies successful cutting events based on observable phenotypes (115). Briefly, the sgRNAs to be tested were injected together with another sgRNA known to work on a targeting gene, *dpy-10*.

Successful cutting event will result in a dominant Dpy mutation

that can easily be seen on dissecting microscope. In addition, the injection mix contains a rescue primer on the same gene that will result in a point mutation with a dominant Rol phenotype. Two sgRNAs were tested at the same time to check for successful cutting events.

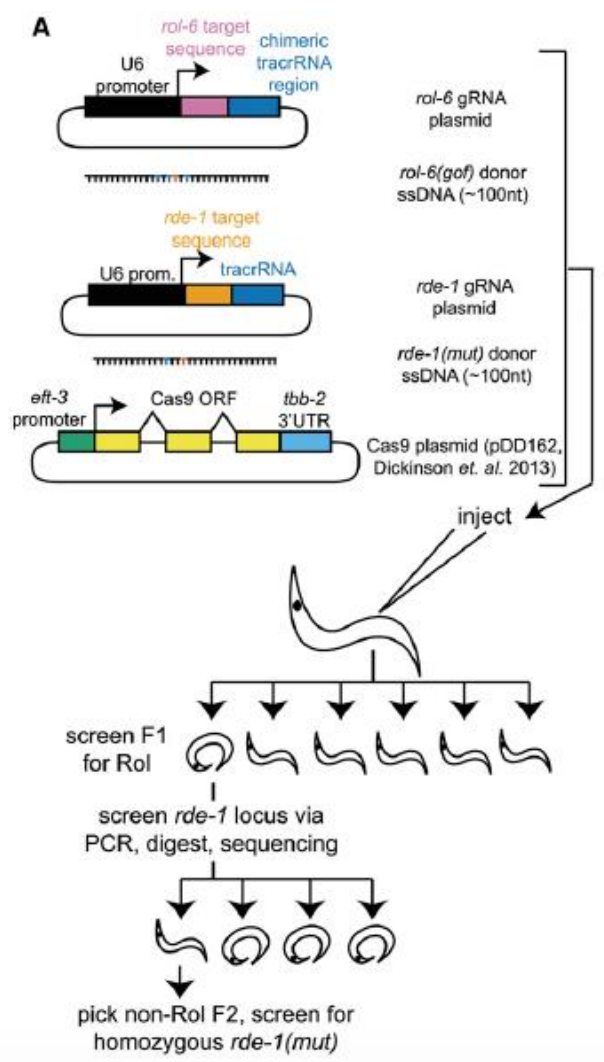


Figure 21 co-CRISPR injection strategy

To verify cutting was successfully guided by the sgRNA, DNA extracted from the F1 worm is amplified around the targeted cut site and sent for sequencing. Several papers reported that cutting usually occurs at 3 nucleotides upstream of the PAM site, resulting to an insertion-deletion (indel) mutation due to the non-specific non-homologous end-joining (NHEJ) DNA repair mechanism (164). A successful cutting event will result in heterozygous mutant strain, with either one of its DNA strand retains the wild type sequence, while another will attain mutation near the PAM site, or both of the strands will be mutated, but result in different indels (162). The sequencing reaction will start as a clean DNA sequence with well-defined peaks that then starts to give double peaks or spurious, overlapping peaks after cutting had occurred (162). Once cutting was confirmed, the sgRNA was used for subsequent strain generation (ie, mutants or endogenously tagged proteins). All primers used to sequence the locus containing the PAM site are listed in Table 8.

Step 4A: Generating fluorescent-tagged genes

There are two methods being used by the organisms to repair the double-stranded break induced by the sequence-specific Cas9 cutting events. The first is through non-homologous end joining (NHEJ) that caused non-specific rescue around the cutting region, causing indel mutation. The second is through sequence-specific homologous recombination repair (164). To generate fluorescent-tagged genes at endogenous loci, the homologous recombination method is favored to ensure no adverse mutation occurring on the gene. To this end, the use of plasmid-mediated

homologous repair containing the flanking sequence homologous to the flanking sequence around the Cas9 cut site was used (101). In brief, 500-1000bp of sequence upstream and downstream of the PAM site were PCR amplified and cloned into the respective clone of desired fluorescence marker (Table 8, (101)). The successful worm containing tagged genes will have hygromycin-resistance gene, that is later removed from the organism through heat-shock express Cre-Lox system (101).

Step 4B: Generating knockout or deletion mutants

The successful sgRNAs that were able to cut at both end of the desired region of deletion were injected simultaneously with co-injection marker, as in when sgRNAs were tested (see Step 3, (163)). A successful Cas9 cutting event will usually yield a heterozygous mutant, with one strand containing the WT DNA size while another strand yield a smaller DNA size. The size difference should be roughly the size in between the location of the two sgRNAs injected. Successful knockout generations were screened using PCR by looking for size shift of the DNA band. The strains were then backcrossed for a minimum of four times to wildtype to eliminate the possible off-site cutting by the sgRNA and co-injection marker.

Step 4C: Generating point mutation

To generate arginine to alanine mutation at amino acid 277 (R277A), rescue oligos were designed around the region of desired mutation by introducing the

desired mutation and a new silent-mutant containing unique *Ava*I restriction digest site for ease of screening. To screen for successful mutation, PCR was done around the region of mutation and digested with *Ava*I before running the PCR on 1% gel.

CONCLUSION

CRISPR-Cas9 system is a powerful technology to generate sequence-specific mutation in any model system (158). The use of CRISPR-Cas9 was suggested to push beyond the boundaries of technological method used to generate specific strains in research, but also as tools in medicine and agriculture (165-168). Since 2013, more CRISPR-Cas9 strategy was further developed in *C. elegans* system to generate conditional knockout by expressing Cas9 under tissue-specific promoter or heat-shock promoter (169-171). Therefore, CRISPR-Cas9 is a promising method that continues to evolve to meet the research needs.

Table 8 List of primers used to generate CRISPR line

MSo#	DNA Sequence	Use	Project
1204	TGAATTCCTCCAAGAAGCTCG		
1205	AAGCTTCACAGCCGACTATG		
1304	GGCTTTTACAGGTAAAATGG GTTTTAGAGCTAGAAATAGC	sgRNA construct, 5'	RGA-8
1305	CCATTTTACCTGTAAAAGC CAAACATTTAGATTTGCAATTC		
1346	GATGCGGCAAAGAGGATTGC	To verify sgRNA cut at 5'	
1347	CTGTGCAGGCAACTCGTTTG		
1367	GGAACCTTTGTGTCAGTTAG GTTTTAGAGCTAGAAATAGC	sgRNA construct, 3'	
1368	CTAACTGACACAAAGGTTT CAAACATTTAGATTTGCAATTC		

1369	GCTCGGAATGGATATTGAAG GTTTTAGAGCTAGAAATAGC		
1370	CTTCAATATCCATTCCGAG CAAACATTTAGATTTGCAATTC		
	1410,1411,1412,1413	To verify sgRNA cut at 3'	
1308	ACGATGGCCAAGTTTGAAGCG	To verify deletion mutant	
1364	TACTGCACTCGTCTGAATGC		
1452	TGCATACCGGATGGGATGAC		
1585	TCTTG GTGGACGCGTTTCCGCTGACT	sgRNA for R277A	
1586	AAAC AGTCAGCGGAAACGCGTCCAC		
1602	GTGATTTCTTCGGCAGAATGGAAT GAA TGAACGGGGTATCTTC GCT GTCTCG GGA AACGCGTCCAAAATCAAAGAATCC GCG CTGCCTTGGATGCTG	Rescue oligos for R277A	
1285	AGACTTCGGAGTATCGGCAC	To verify RGA-8 R277A mutant	
1595	GAGAGGATGATTGGTAGGTG		
1402	ACGTTGTAAAACGACGGCCAGTCGC CGGCA GGTAGGTTTTGTTGGTAGCG	SEC construct, 5' arm on pDD285	
1403	CATGTTTTCTTTAATGAGCTCGGAG ACCAT CATTTTACCTGTAAAAGCGGC		
1404	CGTGATTACAAGGATGACGATGACA AGAGA GAGGTTGGGCATCGTTTCAG	SEC construct, 3' arm on pDD285	
1405	TCACACAGGAAACAGCTATGACCAT GTTAT CTGTGCAGGCAACTCGTTTG		
1618	TCTTG TCGTCCAGATCGTCCTGATA	sgRNA construct, 5'	CED-5
1619	AAAC TATCAGGACGATCTGGACGA		
1635	GAACCTCTGTCAACTTGTCG	To verify sgRNA pair MSo1618 and MSo1619	
1637	TGAAGTGAGTGAGTACTAG		
1564	TCTTG GTTTGTGGTGTAGGATATC	sgRNA at 5'	CED-10
1565	AAAC GATATCCTACACCACAAAC		
1549	CTTTTCTCTCGAAATTCGATGAC	Test successful cutting	
1533	CTATTTTTCCAGTTTTTGGCC		

1573	ACGTTGTAAAACGACGGCCAGTCGC CGGCA TTGACGATTTTCCAGCCG	SEC construct, 5' arm on pDD282	
1574	TCCAGTGAACAATTCTTCTCCTTTAC TCAT TTGTGGGGAGCTCCG	SEC construct, 5' arm on pDD282	
1576	CGTGATTACAAGGATGACGATGACA AGAGA CAAGCGATCAAATGTGTCGTC	SEC construct, 3' arm on pDD282	
1577	TCACACAGGAAACAGCTATGACCAT GTTAT CACCATTTTCCCAGCTTTTGG	SEC construct, 3' arm on pDD282 and pDD287	
1578	CATGTTTTCTTTAATGAGCTCGGAG ACCAT TTGTGGGGAGCTCCG	SEC construct, 5' arm on pDD287	
1579	GAGCAGAAGTTGATCAGCGAGGAA GACTTG CAAGCGATCAAATGTGTCGTC	SEC construct, 3' arm on pDD287	
1584	GTCACGACGTTGTAAAACGACGGCC AGTCG TTGACGATTTTCCAGCCG	SEC construct, 5' arm on pDD287	

Generation of RNAi Clone

INTRODUCTION

The use of RNA to knockdown gene expression was first introduced in 1998 when it was shown that *C. elegans* worms injected with double-stranded RNA resulted in potent and specific gene inactivation (172). Subsequent studies showed that RNA interference (RNAi) can be performed simply by feeding the worms with bacteria expressing dsRNA (117). Since then, RNAi had been the preferred tool to study gene function, especially for essential genes. In this section, I will discuss on the generation of RNAi feeding clone for *let-502* gene.

METHODS AND MATERIALS

Molecular biology reagents: *E. coli* DH5 α , L4440 vector, and *E. coli* HT115

Table 9 Primers used to generate *let-502* RNAi clone.

Bolded letters represent the sequence used to amplify *let-502* gene

Primer #	DNA Sequence
MSo1707	ACCGGCAGATCTGATATCATCGAT CTCTTCGAATGAAAGCTGCC
MSo1708	CCCCTCGAGGTCGACGGTATCGAT AGTTGATACAAGTGCCTCGG
MSo1709	CCCCTCGAGGTCGACGGTATCGAT AGAGCTCTTGAAATCGTGC

RESULT AND DISCUSSION

PCR was done on *C. elegans*' cDNA library using two sets of primer pair, which are MSo1707 with MSo1708, and MSo1707 with MSo1709. Primer pair MSo1707 with MSo1708 generated PCR product of 656bp, while the primer pair

MSo1707 with MSo1709 generated PCR product of 3018bp. The PCR product was recombined on L4440 plasmid (117) digested with *Cla*I, and ligated using Gibson Assembly kit from NEB (116), Cat# E2611. The recombined plasmid was transformed on *E. coli* DH5 α and sequence verified by Sanger sequencing. Verified plasmid was cloned into *E. coli* HT115 strain, the preferred bacterial food for *C. elegans*.

The resultant plasmid was given pMC number and tested for embryonic lethality. I found that the lethality for plasmid pMC249 to be 52.7%, while the embryonic lethality for plasmid pMC250 to 85.7% (Table 10). Therefore, I concluded that knockdown of *let-502* indeed caused embryonic lethality as had been reported other study (11), and that the larger the region used to generate the RNAi construct, the higher the embryonic lethality count.

Table 10 The embryonic lethality count of the constructed plasmid for *let-502* gene.

Plasmid#	Primer pair	Alive	Dead	% Embryonic Lethality
pMC249	MSo1707 MSo1708	182	203	52.7
pMC250	MSo1707 MSo1709	19	114	85.7
L4440	NA	175	1	0.5

REFERENCE

1. I. D. Chin-Sang, A. D. Chisholm, Form of the worm: genetics of epidermal morphogenesis in *C. elegans*. *Trends Genet* **16**, 544-551 (2000).
2. F. Landmann, S. Quintin, M. Labouesse, Multiple regulatory elements with spatially and temporally distinct activities control the expression of the epithelial differentiation gene *lin-26* in *C. elegans*. *Dev Biol* **265**, 478-490 (2004).
3. J. E. Sulston, E. Schierenberg, J. G. White, J. N. Thomson, The embryonic cell lineage of the nematode *Caenorhabditis elegans*. *Dev Biol* **100**, 64-119 (1983).
4. J. R. Priess, D. I. Hirsh, *Caenorhabditis elegans* morphogenesis: the role of the cytoskeleton in elongation of the embryo. *Dev Biol* **117**, 156-173 (1986).
5. E. M. Williams-Masson, A. N. Malik, J. Hardin, An actin-mediated two-step mechanism is required for ventral enclosure of the *C. elegans* hypodermis. *Development* **124**, 2889-2901 (1997).
6. E. M. Williams-Masson, P. J. Heid, C. A. Lavin, J. Hardin, The cellular mechanism of epithelial rearrangement during morphogenesis of the *Caenorhabditis elegans* dorsal hypodermis. *Dev Biol* **204**, 263-276 (1998).
7. W. B. Raich, C. Agbunag, J. Hardin, Rapid epithelial-sheet sealing in the *Caenorhabditis elegans* embryo requires cadherin-dependent filopodial priming. *Curr Biol* **9**, 1139-1146 (1999).
8. M. C. Soto, Sequential Rosettes Drive *C. elegans* Ventral Nerve Cord Assembly. *Dev Cell* **41**, 121-122 (2017).
9. D. A. Starr *et al.*, *unc-83* encodes a novel component of the nuclear envelope and is essential for proper nuclear migration. *Development* **128**, 5039-5050 (2001).
10. T. T. Vuong-Brender, X. Yang, M. Labouesse, *C. elegans* Embryonic Morphogenesis. *Curr Top Dev Biol* **116**, 597-616 (2016).
11. N. Fotopoulos *et al.*, *Caenorhabditis elegans* anillin (*ani-1*) regulates neuroblast cytokinesis and epidermal morphogenesis during embryonic development. *Dev Biol* **383**, 61-74 (2013).
12. A. G. Wallace, H. Raduwan, J. Carlet, M. C. Soto, The RhoGAP myosin 9/HUM-7 integrates signals to modulate RhoA/RHO-1 during embryonic morphogenesis in *C. elegans*. *Development*, (2018).
13. B. D. Williams, R. H. Waterston, Genes critical for muscle development and function in *Caenorhabditis elegans* identified through lethal mutations. *J Cell Biol* **124**, 475-490 (1994).
14. G. R. Francis, R. H. Waterston, Muscle organization in *Caenorhabditis elegans*: localization of proteins implicated in thin filament attachment and I-band organization. *J Cell Biol* **101**, 1532-1549 (1985).
15. R. Francis, R. H. Waterston, Muscle cell attachment in *Caenorhabditis elegans*. *J Cell Biol* **114**, 465-479 (1991).

16. H. Zhang, M. Labouesse, The making of hemidesmosome structures in vivo. *Dev Dyn* **239**, 1465-1476 (2010).
17. H. Zhang *et al.*, A tension-induced mechanotransduction pathway promotes epithelial morphogenesis. *Nature* **471**, 99-103 (2011).
18. P. K. Mattila, P. Lappalainen, Filopodia: molecular architecture and cellular functions. *Nat Rev Mol Cell Biol* **9**, 446-454 (2008).
19. M. Krause, A. Gautreau, Steering cell migration: lamellipodium dynamics and the regulation of directional persistence. *Nat Rev Mol Cell Biol* **15**, 577-590 (2014).
20. V. Vasioukhin, C. Bauer, M. Yin, E. Fuchs, Directed actin polymerization is the driving force for epithelial cell-cell adhesion. *Cell* **100**, 209-219 (2000).
21. W. Wood *et al.*, Wound healing recapitulates morphogenesis in Drosophila embryos. *Nat Cell Biol* **4**, 907-912 (2002).
22. S. Lommel *et al.*, Actin pedestal formation by enteropathogenic Escherichia coli and intracellular motility of Shigella flexneri are abolished in N-WASP-defective cells. *EMBO Rep* **2**, 850-857 (2001).
23. S. B. Snapper *et al.*, N-WASP deficiency reveals distinct pathways for cell surface projections and microbial actin-based motility. *Nat Cell Biol* **3**, 897-904 (2001).
24. C. Le Clainche, M. F. Carrier, Regulation of actin assembly associated with protrusion and adhesion in cell migration. *Physiol Rev* **88**, 489-513 (2008).
25. K. G. Campellone, M. D. Welch, A nucleator arms race: cellular control of actin assembly. *Nat Rev Mol Cell Biol* **11**, 237-251 (2010).
26. T. D. Pollard, Regulation of actin filament assembly by Arp2/3 complex and formins. *Annu Rev Biophys Biomol Struct* **36**, 451-477 (2007).
27. K. Clark, M. Langeslag, C. G. Figdor, F. N. van Leeuwen, Myosin II and mechanotransduction: a balancing act. *Trends Cell Biol* **17**, 178-186 (2007).
28. M. Vicente-Manzanares, X. Ma, R. S. Adelstein, A. R. Horwitz, Non-muscle myosin II takes centre stage in cell adhesion and migration. *Nat Rev Mol Cell Biol* **10**, 778-790 (2009).
29. E. D. Goley, M. D. Welch, The ARP2/3 complex: an actin nucleator comes of age. *Nature reviews. Molecular cell biology* **7**, 713-726 (2006).
30. O. Alekhina, E. Burstein, D. D. Billadeau, Cellular functions of WASP family proteins at a glance. *J Cell Sci* **130**, 2235-2241 (2017).
31. J. D. Rotty, C. Wu, J. E. Bear, New insights into the regulation and cellular functions of the ARP2/3 complex. *Nat Rev Mol Cell Biol* **14**, 7-12 (2013).
32. N. Ibarra, A. Pollitt, R. H. Insall, Regulation of actin assembly by SCAR/WAVE proteins. *Biochem Soc Trans* **33**, 1243-1246 (2005).
33. T. Takenawa, S. Suetsugu, The WASP-WAVE protein network: connecting the membrane to the cytoskeleton. *Nat Rev Mol Cell Biol* **8**, 37-48 (2007).
34. S. Eden, R. Rohatgi, A. V. Podtelejnikov, M. Mann, M. W. Kirschner, Mechanism of regulation of WAVE1-induced actin nucleation by Rac1 and Nck. *Nature* **418**, 790-793 (2002).

35. A. R. Bresnick, Molecular mechanisms of nonmuscle myosin-II regulation. *Curr Opin Cell Biol* **11**, 26-33 (1999).
36. M. A. Conti, R. S. Adelstein, Nonmuscle myosin II moves in new directions. *J Cell Sci* **121**, 11-18 (2008).
37. M. S. Shutova, T. M. Svitkina, Mammalian nonmuscle myosin II comes in three flavors. *Biochem Biophys Res Commun* **506**, 394-402 (2018).
38. M. C. Soto *et al.*, The GEX-2 and GEX-3 proteins are required for tissue morphogenesis and cell migrations in *C. elegans*. *Genes Dev* **16**, 620-632 (2002).
39. F. B. Patel *et al.*, The WAVE/SCAR complex promotes polarized cell movements and actin enrichment in epithelia during *C. elegans* embryogenesis. *Dev Biol* **324**, 297-309 (2008).
40. E. Walck-Shannon, D. Reiner, J. Hardin, Polarized Rac-dependent protrusions drive epithelial intercalation in the embryonic epidermis of *C. elegans*. *Development* **142**, 3549-3560 (2015).
41. E. A. Lundquist, P. W. Reddien, E. Hartwig, H. R. Horvitz, C. I. Bargmann, Three *C. elegans* Rac proteins and several alternative Rac regulators control axon guidance, cell migration and apoptotic cell phagocytosis. *Development* **128**, 4475-4488 (2001).
42. Y. Y. Bernadskaya, F. B. Patel, H. T. Hsu, M. C. Soto, Arp2/3 promotes junction formation and maintenance in the *Caenorhabditis elegans* intestine by regulating membrane association of apical proteins. *Mol Biol Cell* **22**, 2886-2899 (2011).
43. E. Walck-Shannon *et al.*, CDC-42 Orients Cell Migration during Epithelial Intercalation in the *Caenorhabditis elegans* Epidermis. *PLoS Genet* **12**, e1006415 (2016).
44. A. J. Piekny, J. L. Johnson, G. D. Cham, P. E. Mains, The *Caenorhabditis elegans* nonmuscle myosin genes *nmy-1* and *nmy-2* function as redundant components of the *let-502*/Rho-binding kinase and *mel-11*/myosin phosphatase pathway during embryonic morphogenesis. *Development* **130**, 5695-5704 (2003).
45. A. Wissmann, J. Ingles, J. D. McGhee, P. E. Mains, *Caenorhabditis elegans* LET-502 is related to Rho-binding kinases and human myotonic dystrophy kinase and interacts genetically with a homolog of the regulatory subunit of smooth muscle myosin phosphatase to affect cell shape. *Genes Dev* **11**, 409-422 (1997).
46. A. Wissmann, J. Ingles, P. E. Mains, The *Caenorhabditis elegans* *mel-11* myosin phosphatase regulatory subunit affects tissue contraction in the somatic gonad and the embryonic epidermis and genetically interacts with the Rac signaling pathway. *Dev Biol* **209**, 111-127 (1999).
47. C. Gally *et al.*, Myosin II regulation during *C. elegans* embryonic elongation: LET-502/ROCK, MRCK-1 and PAK-1, three kinases with different roles. *Development* **136**, 3109-3119 (2009).
48. P. Madaule, R. Axel, A novel ras-related gene family. *Cell* **41**, 31-40 (1985).

49. C. D. Nobes, A. Hall, Rho, rac, and cdc42 GTPases regulate the assembly of multimolecular focal complexes associated with actin stress fibers, lamellipodia, and filopodia. *Cell* **81**, 53-62 (1995).
50. A. Hall, Rho GTPases and the actin cytoskeleton. *Science* **279**, 509-514 (1998).
51. S. Etienne-Manneville, A. Hall, Rho GTPases in cell biology. *Nature* **420**, 629-635 (2002).
52. J. L. Bos, H. Rehmann, A. Wittinghofer, GEFs and GAPs: critical elements in the control of small G proteins. *Cell* **129**, 865-877 (2007).
53. L. J. Neukomm, S. Zeng, A. P. Frei, P. A. Huegli, M. O. Hengartner, Small GTPase CDC-42 promotes apoptotic cell corpse clearance in response to PAT-2 and CED-1 in *C. elegans*. *Cell Death Differ* **21**, 845-853 (2014).
54. L. J. Neukomm *et al.*, Loss of the RhoGAP SRGP-1 promotes the clearance of dead and injured cells in *Caenorhabditis elegans*. *Nat Cell Biol* **13**, 79-86 (2011).
55. J. Cherfils, M. Zeghouf, Regulation of small GTPases by GEFs, GAPs, and GDIs. *Physiol Rev* **93**, 269-309 (2013).
56. S. K. Chandhoke, M. S. Mooseker, A role for myosin IXb, a motor-RhoGAP chimera, in epithelial wound healing and tight junction regulation. *Molecular Biology of the Cell* **23**, 2468-2480 (2012).
57. P. J. Hanley *et al.*, Motorized RhoGAP myosin IXb (Myo9b) controls cell shape and motility. *Proceedings of the National Academy of Sciences* **107**, 12145-12150 (2010).
58. P. S. Hegan *et al.*, Mice lacking myosin IXb, an inflammatory bowel disease susceptibility gene, have impaired intestinal barrier function and superficial ulceration in the ileum. *Cytoskeleton* **73**, 163-179 (2016).
59. A. Inoue, J. Saito, R. Ikebe, M. Ikebe, Myosin IXb is a single-headed minus-end-directed processive motor. *Nature Cell Biology* **4**, 302 (2002).
60. W. Liao, K. Elfrink, M. Bähler, Head of Myosin IX Binds Calmodulin and Moves Processively toward the Plus-end of Actin Filaments. *The Journal of Biological Chemistry* **285**, 24933-24942 (2010).
61. T. Omelchenko, A. Hall, Myosin-IXA Regulates Collective Epithelial Cell Migration by Targeting RhoGAP Activity to Cell-Cell Junctions. *Current Biology* **22**, 278-288 (2012).
62. M. Abouhamed *et al.*, Myosin IXa Regulates Epithelial Differentiation and Its Deficiency Results in Hydrocephalus. *Molecular Biology of the Cell* **20**, 5074-5085 (2009).
63. S. Thelen, M. Abouhamed, G. Ciarimboli, B. Edemir, M. Bähler, Rho GAP myosin IXa is a regulator of kidney tubule function. *American Journal of Physiology-Renal Physiology* **309**, F501-F513 (2015).
64. P. Li *et al.*, A meta-analysis of the relationship between MYO9B gene polymorphisms and susceptibility to Crohn's disease and ulcerative colitis. *Human Immunology* **77**, 990-996 (2016).
65. M. Prager *et al.*, Myosin IXb variants and their pivotal role in maintaining the intestinal barrier: A study in Crohn's disease. *Scandinavian Journal of Gastroenterology* **49**, 1191-1200 (2014).

66. M.-J. Wang *et al.*, MYO9B gene polymorphisms are associated with the risk of inflammatory bowel diseases. *Oncotarget* **7**, 58862-58875 (2016).
67. M. C. Parrini *et al.*, SH3BP1, an exocyst-associated RhoGAP, inactivates Rac1 at the front to drive cell motility. *Mol Cell* **42**, 650-661 (2011).
68. A. Elbediwy *et al.*, Epithelial junction formation requires confinement of Cdc42 activity by a novel SH3BP1 complex. *J Cell Biol* **198**, 677-693 (2012).
69. L. Chan Wah Hak *et al.*, FBP17 and CIP4 recruit SHIP2 and lamellipodin to prime the plasma membrane for fast endophilin-mediated endocytosis. *Nat Cell Biol* **20**, 1023-1031 (2018).
70. N. Richnau, P. Aspenstrom, Rich, a rho GTPase-activating protein domain-containing protein involved in signaling by Cdc42 and Rac1. *J Biol Chem* **276**, 35060-35070 (2001).
71. C. D. Wells *et al.*, A Rich1/Amot complex regulates the Cdc42 GTPase and apical-polarity proteins in epithelial cells. *Cell* **125**, 535-548 (2006).
72. N. Richnau, A. Fransson, K. Farsad, P. Aspenstrom, RICH-1 has a BIN/Amphiphysin/Rvsp domain responsible for binding to membrane lipids and tubulation of liposomes. *Biochem Biophys Res Commun* **320**, 1034-1042 (2004).
73. U. Salzer, J. Kostan, K. Djinovic-Carugo, Deciphering the BAR code of membrane modulators. *Cell Mol Life Sci* **74**, 2413-2438 (2017).
74. B. J. Peter *et al.*, BAR domains as sensors of membrane curvature: the amphiphysin BAR structure. *Science* **303**, 495-499 (2004).
75. A. Frost *et al.*, Structural basis of membrane invagination by F-BAR domains. *Cell* **132**, 807-817 (2008).
76. C. Mim *et al.*, Structural basis of membrane bending by the N-BAR protein endophilin. *Cell* **149**, 137-145 (2012).
77. K. Takano, K. Toyooka, S. Suetsugu, EFC/F-BAR proteins and the N-WASP-WIP complex induce membrane curvature-dependent actin polymerization. *EMBO J* **27**, 2817-2828 (2008).
78. H. Miki, H. Yamaguchi, S. Suetsugu, T. Takenawa, IRSp53 is an essential intermediate between Rac and WAVE in the regulation of membrane ruffling. *Nature* **408**, 732-735 (2000).
79. S. Suetsugu *et al.*, Optimization of WAVE2 complex-induced actin polymerization by membrane-bound IRSp53, PIP(3), and Rac. *J Cell Biol* **173**, 571-585 (2006).
80. D. L. Rocca, S. Martin, E. L. Jenkins, J. G. Hanley, Inhibition of Arp2/3-mediated actin polymerization by PICK1 regulates neuronal morphology and AMPA receptor endocytosis. *Nat Cell Biol* **10**, 259-271 (2008).
81. J. Kostan *et al.*, Direct interaction of actin filaments with F-BAR protein pacsin2. *EMBO Rep* **15**, 1154-1162 (2014).
82. N. M. Drager *et al.*, Bin1 directly remodels actin dynamics through its BAR domain. *EMBO Rep* **18**, 2051-2066 (2017).
83. D. D. Tang, B. D. Gerlach, The roles and regulation of the actin cytoskeleton, intermediate filaments and microtubules in smooth muscle cell migration. *Respir Res* **18**, 54 (2017).

84. X. H. Jaglin, J. Chelly, Tubulin-related cortical dysgeneses: microtubule dysfunction underlying neuronal migration defects. *Trends Genet* **25**, 555-566 (2009).
85. Y. Ding, J. Xu, J. S. Bromberg, Regulatory T cell migration during an immune response. *Trends Immunol* **33**, 174-180 (2012).
86. T. J. Shaw, P. Martin, Wound repair: a showcase for cell plasticity and migration. *Curr Opin Cell Biol* **42**, 29-37 (2016).
87. P. Martin, S. M. Parkhurst, Parallels between tissue repair and embryo morphogenesis. *Development* **131**, 3021-3034 (2004).
88. A. Nurnberg, T. Kitzing, R. Grosse, Nucleating actin for invasion. *Nat Rev Cancer* **11**, 177-187 (2011).
89. E. T. Roussos, J. S. Condeelis, A. Patsialou, Chemotaxis in cancer. *Nat Rev Cancer* **11**, 573-587 (2011).
90. R. P. Stevenson, D. Veltman, L. M. Machesky, Actin-bundling proteins in cancer progression at a glance. *J Cell Sci* **125**, 1073-1079 (2012).
91. S. Brenner, The genetics of *Caenorhabditis elegans*. *Genetics* **77**, 71-94 (1974).
92. M. Sawa *et al.*, Essential role of the *C. elegans* Arp2/3 complex in cell migration during ventral enclosure. *J Cell Sci* **116**, 1505-1518 (2003).
93. J. Withee, B. Galligan, N. Hawkins, G. Garriga, *Caenorhabditis elegans* WASP and Ena/VASP proteins play compensatory roles in morphogenesis and neuronal cell migration. *Genetics* **167**, 1165-1176 (2004).
94. K. T. Kumfer *et al.*, CGEF-1 and CHIN-1 regulate CDC-42 activity during asymmetric division in the *Caenorhabditis elegans* embryo. *Mol Biol Cell* **21**, 266-277 (2010).
95. A. Beatty, D. G. Morton, K. Kempfues, PAR-2, LGL-1 and the CDC-42 GAP CHIN-1 act in distinct pathways to maintain polarity in the *C. elegans* embryo. *Development* **140**, 2005-2014 (2013).
96. Y. Zilberman, J. Abrams, D. C. Anderson, J. Nance, Cdc42 regulates junctional actin but not cell polarization in the *Caenorhabditis elegans* epidermis. *J Cell Biol* **216**, 3729-3744 (2017).
97. S. Kurisu, T. Takenawa, The WASP and WAVE family proteins. *Genome Biol* **10**, 226 (2009).
98. M. F. Carrier, A. Ducruix, D. Pantaloni, Signalling to actin: the Cdc42-N-WASP-Arp2/3 connection. *Chem Biol* **6**, R235-240 (1999).
99. M. H. Ouellette, E. Martin, G. Lacoste-Caron, K. Hamiche, S. Jenna, Spatial control of active CDC-42 during collective migration of hypodermal cells in *Caenorhabditis elegans*. *J Mol Cell Biol* **8**, 313-327 (2016).
100. C. Giuliani *et al.*, Requirements for F-BAR proteins TOCA-1 and TOCA-2 in actin dynamics and membrane trafficking during *Caenorhabditis elegans* oocyte growth and embryonic epidermal morphogenesis. *PLoS Genet* **5**, e1000675 (2009).
101. D. J. Dickinson, A. M. Pani, J. K. Heppert, C. D. Higgins, B. Goldstein, Streamlined Genome Engineering with a Self-Excising Drug Selection Cassette. *Genetics* **200**, 1035-1049 (2015).

102. V. Gobel, P. L. Barrett, D. H. Hall, J. T. Fleming, Lumen morphogenesis in *C. elegans* requires the membrane-cytoskeleton linker erm-1. *Dev Cell* **6**, 865-873 (2004).
103. S. Havrylenko *et al.*, WAVE binds Ena/VASP for enhanced Arp2/3 complex-based actin assembly. *Mol Biol Cell* **26**, 55-65 (2015).
104. B. Goldstein, I. G. Macara, The PAR proteins: fundamental players in animal cell polarization. *Dev Cell* **13**, 609-622 (2007).
105. B. D. Grant, J. G. Donaldson, Pathways and mechanisms of endocytic recycling. *Nat Rev Mol Cell Biol* **10**, 597-608 (2009).
106. D. Wernike, Y. Chen, K. Mastronardi, N. Makil, A. Piekny, Mechanical forces drive neuroblast morphogenesis and are required for epidermal closure. *Dev Biol* **412**, 261-277 (2016).
107. R. Zaidel-Bar *et al.*, The F-BAR domain of SRGP-1 facilitates cell-cell adhesion during *C. elegans* morphogenesis. *J Cell Biol* **191**, 761-769 (2010).
108. C. Wang *et al.*, Rac GTPase activating protein 1 promotes oncogenic progression of epithelial ovarian cancer. *Cancer Sci* **109**, 84-93 (2018).
109. R. Stone, 2nd *et al.*, Identification of genes correlated with early-stage bladder cancer progression. *Cancer Prev Res (Phila)* **3**, 776-786 (2010).
110. S. Saigusa *et al.*, Clinical significance of RacGAP1 expression at the invasive front of gastric cancer. *Gastric Cancer* **18**, 84-92 (2015).
111. H. Imaoka *et al.*, RacGAP1 expression, increasing tumor malignant potential, as a predictive biomarker for lymph node metastasis and poor prognosis in colorectal cancer. *Carcinogenesis* **36**, 346-354 (2015).
112. S. Sasidharan *et al.*, WAVE regulates Cadherin junction assembly and turnover during epithelial polarization. *Dev Biol* **434**, 133-148 (2018).
113. P. D. Hsu *et al.*, DNA targeting specificity of RNA-guided Cas9 nucleases. *Nat Biotechnol* **31**, 827-832 (2013).
114. H. Kim *et al.*, A co-CRISPR strategy for efficient genome editing in *Caenorhabditis elegans*. *Genetics* **197**, 1069-1080 (2014).
115. J. A. Arribere *et al.*, Efficient marker-free recovery of custom genetic modifications with CRISPR/Cas9 in *Caenorhabditis elegans*. *Genetics* **198**, 837-846 (2014).
116. D. G. Gibson *et al.*, Enzymatic assembly of DNA molecules up to several hundred kilobases. *Nat Methods* **6**, 343-345 (2009).
117. L. Timmons, A. Fire, Specific interference by ingested dsRNA. *Nature* **395**, 854 (1998).
118. R. S. Kamath, M. Martinez-Campos, P. Zipperlen, A. G. Fraser, J. Ahringer, Effectiveness of specific RNA-mediated interference through ingested double-stranded RNA in *Caenorhabditis elegans*. *Genome Biol* **2**, RESEARCH0002 (2001).
119. Y. Y. Bernadskaya, A. Wallace, J. Nguyen, W. A. Mohler, M. C. Soto, UNC-40/DCC, SAX-3/Robo, and VAB-1/Eph polarize F-actin during embryonic morphogenesis by regulating the WAVE/SCAR actin nucleation complex. *PLoS Genet* **8**, e1002863 (2012).

120. T. Omelchenko, Regulation of collective cell migration by RhoGAP myosin IXA. *Small GTPases* **3**, 213-218 (2012).
121. R. Kong *et al.*, Myo9b is a key player in SLIT/ROBO-mediated lung tumor suppression. *The Journal of Clinical Investigation* **125**, 4407-4420 (2015).
122. Katarzyna A. Makowska, Ruth E. Hughes, Kathryn J. White, Claire M. Wells, M. Peckham, Specific Myosins Control Actin Organization, Cell Morphology, and Migration in Prostate Cancer Cells. *Cell Reports* **13**, 2118-2125 (2015).
123. Y. Y. Bernadskaya, A. Wallace, J. Nguyen, W. A. Mohler, M. C. Soto, UNC-40/DCC, SAX-3/Robo, and VAB-1/Eph Polarize F-Actin during Embryonic Morphogenesis by Regulating the WAVE/SCAR Actin Nucleation Complex. *PLoS Genetics* **8**, e1002863 (2012).
124. D. Sieburth *et al.*, Systematic analysis of genes required for synapse structure and function. *Nature* **436**, 510-517 (2005).
125. E. O'Connor *et al.*, Identification of mutations in the MYO9A gene in patients with congenital myasthenic syndrome. *Brain* **139**, 2143-2153 (2016).
126. T. W. Yu, J. C. Hao, W. Lim, M. Tessier-Lavigne, C. I. Bargmann, Shared receptors in axon guidance: SAX-3/Robo signals via UNC-34/Enabled and a Netrin-independent UNC-40/DCC function. *Nat Neurosci* **5**, 1147-1154 (2002).
127. M. Bähler, A. Rhoads, Calmodulin signaling via the IQ motif. *FEBS Letters* **513**, 107-113 (2002).
128. M. C. Soto *et al.*, The GEX-2 and GEX-3 proteins are required for tissue morphogenesis and cell migrations in *C. elegans*. *Genes & Development* **16**, 620-632 (2002).
129. L. J. Neukomm *et al.*, Getting rid of damaged goods: Loss of RhoGAP SRGP-1 promotes the clearance of dead and injured cells in *C. elegans*. *Nature cell biology* **13**, 10.1038/ncb2138 (2011).
130. L. J. Neukomm, S. Zeng, A. P. Frei, P. A. Huegli, M. O. Hengartner, Small GTPase CDC-42 promotes apoptotic cell corpse clearance in response to PAT-2 and CED-1 in *C. elegans*. *Cell Death and Differentiation* **21**, 845-853 (2014).
131. R. Zaidel-Bar *et al.*, The F-BAR domain of SRGP-1 facilitates cell-cell adhesion during *C. elegans* morphogenesis. *The Journal of Cell Biology* **191**, 761-769 (2010).
132. S. Zonies, F. Motegi, Y. Hao, G. Seydoux, Symmetry breaking and polarization of the *C. elegans* zygote by the polarity protein PAR-2. *Development (Cambridge, England)* **137**, 1669-1677 (2010).
133. D. M. Miller, III, I. Ortiz, G. C. Berliner, H. F. Epstein, Differential localization of two myosins within nematode thick filaments. *Cell* **34**, 477-490 (1983).
134. Daniel J. Marston *et al.*, MRCK-1 Drives Apical Constriction in *C. elegans* by Linking Developmental Patterning to Force Generation. *Current Biology* **26**, 2079-2089 (2016).

135. R. Viveiros, H. Hutter, D. G. Moerman, Membrane extensions are associated with proper anterior migration of muscle cells during *Caenorhabditis elegans* embryogenesis. *Developmental Biology* **358**, 189-200 (2011).
136. F. B. Patel *et al.*, The WAVE/SCAR complex promotes polarized cell movements and actin enrichment in epithelia during *C. elegans* embryogenesis. *Developmental biology* **324**, 297-309 (2008).
137. C. Gally *et al.*, Myosin II regulation during *C. elegans* embryonic elongation: LET-502/ROCK, MRCK-1 and PAK-1, three kinases with different roles. *Development* **136**, 3109-3119 (2009).
138. S. Havrylenko *et al.*, WAVE binds Ena/VASP for enhanced Arp2/3 complex-based actin assembly. *Molecular Biology of the Cell* **26**, 55-65 (2015).
139. N. Fotopoulos *et al.*, *Caenorhabditis elegans* anillin (*ani-1*) regulates neuroblast cytokinesis and epidermal morphogenesis during embryonic development. *Developmental biology* **383**, 61-74 (2013).
140. M. Diogon *et al.*, The RhoGAP RGA-2 and LET-502/ROCK achieve a balance of actomyosin-dependent forces in *C. elegans* epidermis to control morphogenesis. *Development* **134**, 2469-2479 (2007).
141. E. Martin *et al.*, *pix-1* Controls Early Elongation in Parallel with *mel-11* and *let-502* in *Caenorhabditis elegans*. *PLoS ONE* **9**, e94684 (2014).
142. A. J. Piekny, J.-L. F. Johnson, G. D. Cham, P. E. Mains, The *Caenorhabditis elegans* nonmuscle myosin genes *nmy-1* and *nmy-2* function as redundant components of the *let-502*/Rho-binding kinase and *mel-11*/myosin phosphatase pathway during embryonic morphogenesis. *Development* **130**, 5695-5704 (2003).
143. A. J. Piekny, A. Wissmann, P. E. Mains, Embryonic morphogenesis in *Caenorhabditis elegans* integrates the activity of LET-502 Rho-binding kinase, MEL-11 myosin phosphatase, DAF-2 insulin receptor and FEM-2 PP2c phosphatase. *Genetics* **156**, 1671-1689 (2000).
144. D. Wernike, Y. Chen, K. Mastronardi, N. Makil, A. Piekny, Mechanical forces drive neuroblast morphogenesis and are required for epidermal closure. *Developmental Biology* **412**, 261-277 (2016).
145. U. Theisen, E. Straube, A. Straube, Directional Persistence of Migrating Cells Requires Kif1C-Mediated Stabilization of Trailing Adhesions. *Developmental cell* **23**, 1153-1166 (2012).
146. C. Suarez, D. R. Kovar, Intermolecular competition for monomers governs actin cytoskeleton organization. *Nature reviews. Molecular cell biology* **17**, 799-810 (2016).
147. S. Ghenea, J. R. Boudreau, N. P. Lague, I. D. Chin-Sang, The VAB-1 Eph receptor tyrosine kinase and SAX-3/Robo neuronal receptors function together during *C. elegans* embryonic morphogenesis. *Development* **132**, 3679-3690 (2005).
148. R. Ikegami *et al.*, Semaphorin and Eph Receptor Signaling Guide a Series of Cell Movements for Ventral Enclosure in *C. elegans*. *Current Biology* **22**, 1-11 (2012).

149. D. M. Miller, 3rd, I. Ortiz, G. C. Berliner, H. F. Epstein, Differential localization of two myosins within nematode thick filaments. *Cell* **34**, 477-490 (1983).
150. A. K. Corsi, B. Wightman, M. Chalfie, A Transparent window into biology: A primer on *Caenorhabditis elegans*. *WormBook*, 1-31 (2015).
151. A. J. Piekny, P. E. Mains, Squeezing an egg into a worm: *C. elegans* embryonic morphogenesis. *ScientificWorldJournal* **3**, 1370-1381 (2003).
152. C. A. Shelton, J. C. Carter, G. C. Ellis, B. Bowerman, The nonmuscle myosin regulatory light chain gene *mlc-4* is required for cytokinesis, anterior-posterior polarity, and body morphology during *Caenorhabditis elegans* embryogenesis. *J Cell Biol* **146**, 439-451 (1999).
153. M. Abouhamed *et al.*, Myosin IXa regulates epithelial differentiation and its deficiency results in hydrocephalus. *Mol Biol Cell* **20**, 5074-5085 (2009).
154. P. Horvath, R. Barrangou, CRISPR/Cas, the immune system of bacteria and archaea. *Science* **327**, 167-170 (2010).
155. D. Bhaya, M. Davison, R. Barrangou, CRISPR-Cas systems in bacteria and archaea: versatile small RNAs for adaptive defense and regulation. *Annu Rev Genet* **45**, 273-297 (2011).
156. B. Wiedenheft, S. H. Sternberg, J. A. Doudna, RNA-guided genetic silencing systems in bacteria and archaea. *Nature* **482**, 331-338 (2012).
157. M. Jinek *et al.*, A programmable dual-RNA-guided DNA endonuclease in adaptive bacterial immunity. *Science* **337**, 816-821 (2012).
158. P. Mali, K. M. Esvelt, G. M. Church, Cas9 as a versatile tool for engineering biology. *Nat Methods* **10**, 957-963 (2013).
159. F. A. Ran *et al.*, Double nicking by RNA-guided CRISPR Cas9 for enhanced genome editing specificity. *Cell* **154**, 1380-1389 (2013).
160. F. A. Ran *et al.*, Genome engineering using the CRISPR-Cas9 system. *Nat Protoc* **8**, 2281-2308 (2013).
161. D. J. Dickinson, J. D. Ward, D. J. Reiner, B. Goldstein, Engineering the *Caenorhabditis elegans* genome using Cas9-triggered homologous recombination. *Nat Methods* **10**, 1028-1034 (2013).
162. A. E. Friedland *et al.*, Heritable genome editing in *C. elegans* via a CRISPR-Cas9 system. *Nat Methods* **10**, 741-743 (2013).
163. A. Paix *et al.*, Scalable and versatile genome editing using linear DNAs with microhomology to Cas9 Sites in *Caenorhabditis elegans*. *Genetics* **198**, 1347-1356 (2014).
164. S. Xu, The application of CRISPR-Cas9 genome editing in *Caenorhabditis elegans*. *J Genet Genomics* **42**, 413-421 (2015).
165. M. Sachdeva *et al.*, CRISPR/Cas9: molecular tool for gene therapy to target genome and epigenome in the treatment of lung cancer. *Cancer Gene Ther* **22**, 509-517 (2015).
166. C. Gao, The future of CRISPR technologies in agriculture. *Nat Rev Mol Cell Biol* **19**, 275-276 (2018).
167. A. Eid, M. M. Mahfouz, Genome editing: the road of CRISPR/Cas9 from bench to clinic. *Exp Mol Med* **48**, e265 (2016).

168. F. A. Khan *et al.*, CRISPR/Cas9 therapeutics: a cure for cancer and other genetic diseases. *Oncotarget* **7**, 52541-52552 (2016).
169. P. Liu *et al.*, Heritable/conditional genome editing in *C. elegans* using a CRISPR-Cas9 feeding system. *Cell Res* **24**, 886-889 (2014).
170. Z. Shen *et al.*, Conditional knockouts generated by engineered CRISPR-Cas9 endonuclease reveal the roles of coronin in *C. elegans* neural development. *Dev Cell* **30**, 625-636 (2014).
171. W. Li, P. Yi, G. Ou, Somatic CRISPR-Cas9-induced mutations reveal roles of embryonically essential dynein chains in *Caenorhabditis elegans* cilia. *J Cell Biol* **208**, 683-692 (2015).
172. A. Fire *et al.*, Potent and specific genetic interference by double-stranded RNA in *Caenorhabditis elegans*. *Nature* **391**, 806-811 (1998).